Summer 2018

Epithelial Sheet Response to External Stimuli

Yashar Bashirzadeh
Old Dominion University

EPITHELIAL SHEET RESPONSE TO EXTERNAL STIMULI

by

Yashar Bashirzadeh
B.S. January 2009, University of Zanjan, Zanjan, Iran
M.S. December 2012, Islamic Azad University, Science and Research Branch, Tehran, Iran

A Dissertation Submitted to the Faculty of
Old Dominion University in Partial Fulfillment of the
Requirements for the Degree of

DOCTOR OF PHILOSOPHY

MECHANICAL ENGINEERING

OLD DOMINION UNIVERSITY
August 2018

Approved by:

Shizhi Qian (Director)

Venkat Maruthamuthu (Co-Director)

Xiaoyu Zhang (Member)

Yan Peng (Member)

ABSTRACT

EPITHELIAL SHEET RESPONSE TO EXTERNAL STIMULI

Yashar Bashirzadeh
Old Dominion University, 2018
Directors: Dr. Shizhi Qian and Dr. Venkat Maruthamuthu

Mechanical communication of adherent cells with their micro-environment is mediated by cytoskeletal and adhesion proteins. These mechanical links aid tissues in maintaining their coherence in the context of the surrounding extra cellular matrix (ECM). Epithelial tissues exert force on the ECM through integrin-based junctions and maintain their coherency through E-cadherin-based cell-cell junctions while dynamically undergoing collective migration. Such a complex network of communication involving the cell cytoskeleton and adhesion proteins modulates the tissue's response to external cues. Two distinct forms of such external stimuli are those of electrical and mechanical origin.

Epithelial tissues quickly respond to physiologically relevant electric fields by moving toward one pole of the electric field. By pharmacological modulation of the actin cytoskeleton, we showed that the basic mechanism by which epithelial monolayers migrate is not altered by the application of external direct current (DC) electric field despite their directionality being biased toward the cathode. It was shown that the DC electric field controls monolayer migration by affecting cell polarity rather than the speed of cell migration.

Epithelial islands respond to external mechanical signals by altering the traction force exerted on the substrate. Here, fourier transform traction cytometry (FTTC) showed that the traction force, strain energy, and sheet tension of micropatterned eipthelial islands increase upon the application of 10% uniaxial substrate stretch and continues to temporally increase. Interestingly, the sheet tension at the island mid-line parallel to the stretch direction reached levels similar to the sheet

tension of the mid-line perpendicular to the stretch direction over time, indicating the island's tendency to homogenize its internal stress. Here, a modified protocol was used to measure the elastic properties of the soft silicon substrate required for FTTC. The validity of FTTC in quantification of the wall shear stress of small-scale flow-channels over a wide range of steady flow rates was also demonstrated.

This dissertation is dedicated to my wife, Irianna.

Editing formats of this dissertation are based on the Wiley online library (chapter 2), the Elsevier publishing company (chapter 4); and Springer (chapter 5).

ACKNOWLEDGEMENTS

TABLE OF CONTENTS

LIST OF FIGURES

Chapter 1

Chapter 2

Chapter 3

Chapter 4

Chapter 5

Figure   Page

LIST OF TABLES

CHAPTER 1

INTRODUCTION

1.1 Bioelectric manipulation of epithelial cell migration

To survive, living cells need to constantly interact with their immediate environment. Cells can respond to their surroundings via transmembrane receptors, intermediate proteins between cell, and extra cellular environment. Signals are then transmitted to the intracellular environment through the plasma membrane where they are transducted to biochemical reactions within the cell. For example, cell migration on a substrate is a result of cytoskeletal rearrangements (Figure 1b) in response to external signals of different origins: chemical, electrical, mechanical etc. These rearrangements moving the cells forward involve elongation of actin filaments (through polymerization) in the leading edge (where the cell protrudes), formation of adhesive contacts with the extra cellular matrix, contraction of the cytoplasm and finally detachment of the rear of the cell. Cells in monolayers undergo similar processes and rearrangements to migrate. Interaction of cells with neighboring cells through cell-cell junctions in monolayers makes for more complex signaling pathways and cytoskeletal rearrangements.

Cell/monolayer migration is generally random unless controlled external signals such as electric field (electrotaxis) (Figure 1a) bias the direction of motion. For example application of uniform direct current electric field (DCEF) is known to bias migration of many types of cells including cells in monolayers toward either the cathode or anode of the applied field. Studying the electrotactic behavior of cells has provided better insight into cell migration and physiological processes (eg. Wound healing) in vivo in which electric fields are directly involved.
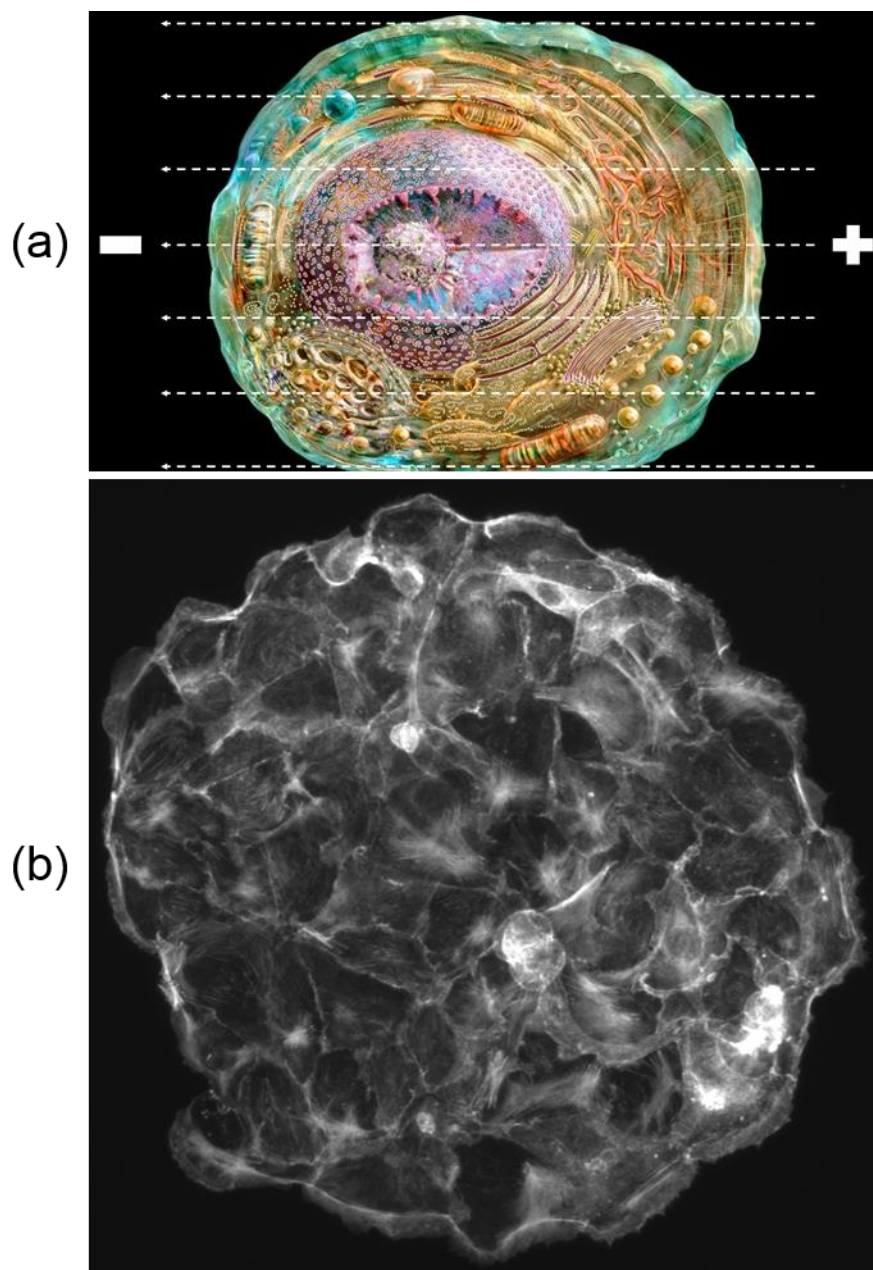
Figure 1. (a) Hundreds of extra/intra cellular molecules are involved in the receipt, transduction, and cell response to electric field. The credit for the background cutaway cell image: Russell Kightley/Science Photo Library. (b) Mechanical response of epithelial islands is a result of cytoskeletal rearrangements mainly actin filaments (white fibers in the figure) of each cell linked to ECM and neighboring cells via several adhesion proteins.

Chapter 2, first introduces *in vitro* studies of the migration of epithelial monolayers under DCEF. In chapter 2, a detailed introduction to electrotaxis and factors which regulate the response of cells to electrotaxis (using pharmacological inhibitors of key components controlling cell/monolayer migration) is provided. Here, we wanted to specifically test the extent to which both actin organization and the level of cell contractility influenced collective cell electrotaxis in response to an EF of physiologically relevant magnitude [1]. In particular, we wanted to determine how these modulations affected the speed and directionality of the collective electrotactic response compared to a case with no directional cue. In a set of *in vitro* studies (Figure 2) we applied a DC electric field (DCEF) on MDCK II monolayers (Figures 3 and 4) without (Figure 5) or with pharmacological inhibitors that tune actin organization or contractility either higher or lower. We found that only the state of higher contractility showed a loss of directionality in response to DCEF. Importantly, while all treatments altered cell speed to varying levels, we found that, for every treatment, this effect was very similar to their effect on random cell migration speeds within monolayers even in the absence of DCEF. The latter result suggests little effect of the electric field on the migration machinery itself.
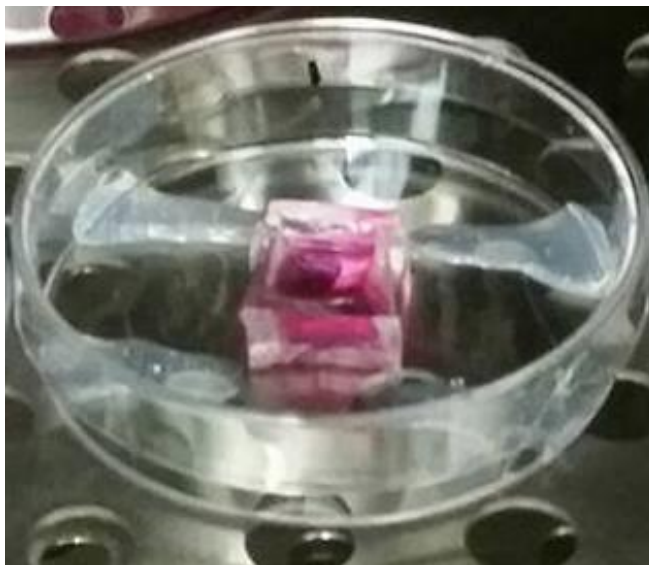
Figure 2. Cells are plated and confined within a Polydimethylsiloxane (PDMS) well placed in the middle of an electrotaxis chamber.
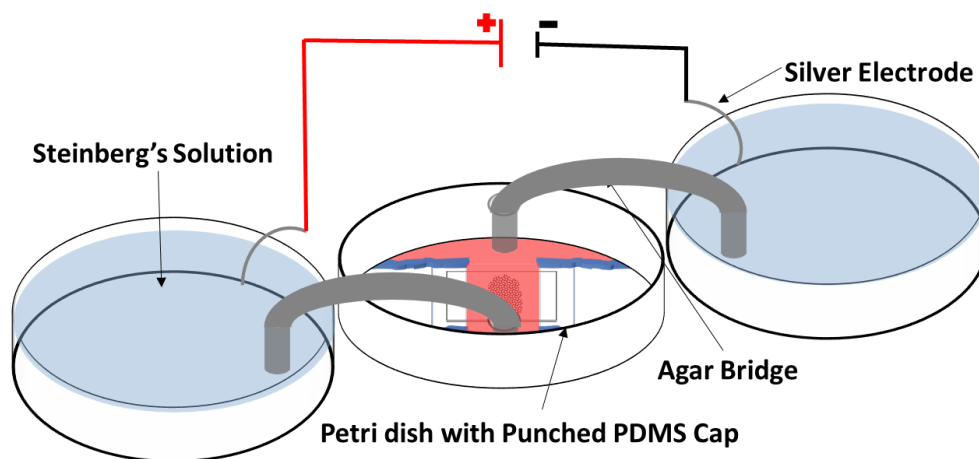
Figure 3. Schematic of monolayer in electrotaxis chamber under DCEF.

Figure 4. Experimental setup for imaging monolayers during electrotaxis
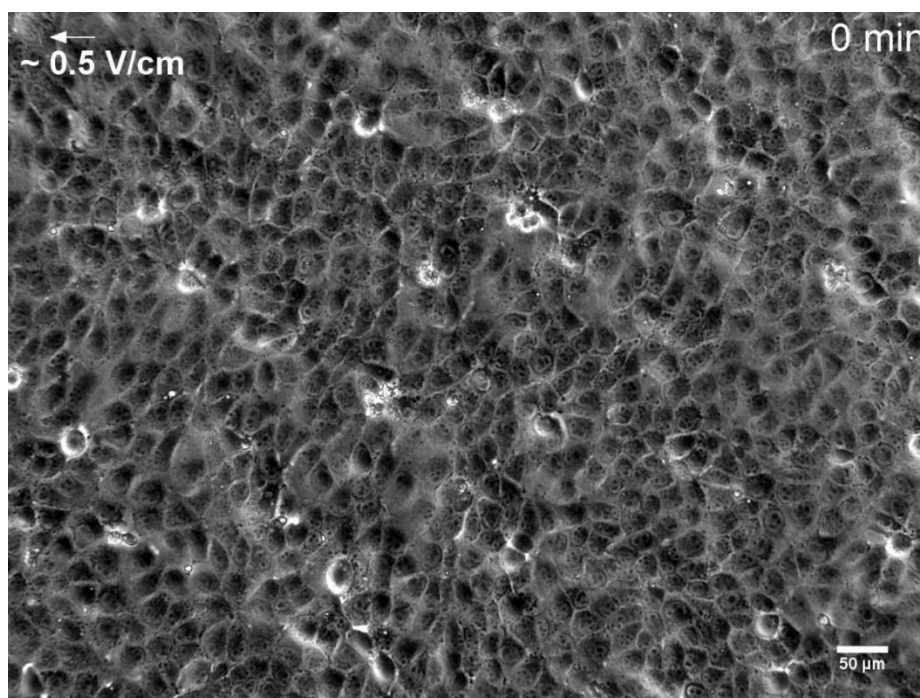
Figure 5. Phase image of 0.5 mm^2 part of control MDCK monolayer under DCEF.

1.2 Traction force microscopy

As previously mentioned, actin polymerization and actomyosin contraction are the key cytoskeletal functions controlling cell migration. Actin filaments interact with the extra cellular matrix (ECM) through integrins, the key proteins of focal adhesions (FA) involved in cell adhesion to ECM. Therefore, actin polymerization and actomyosin interaction causes cells/monolayers to apply force on their substrate enabling cells to migrate. There are several methods to quantify the traction force, the majority of which use elasticity theories to extract shear force (traction force) from displacement of elastic substrates. Fourier transform traction cytometry (FTTC) is an efficient approach which quantifies the traction stress field from the displacement field of a substrate with known elastic properties, particularly Young's modulus (E) and Poisson's ratio (ν). FTTC enables us to quantify the exchange of mechanical forces between cells and their micro environment (mechanotransduction). For example, the application of mechanical force by stretch which regulates cell traction forces can be investigated. *In vivo*, stretching is a vital process in cardiac and respiratory cycles. In monolayers, stretch-induced changes in cell force on ECM through focal adhesions, cell force on neighboring cells through cell-cell adhesion proteins, and cell sheet tension could be measured. Yet a proper characterization of monolayer response to stretch and its interaction with ECM requires micropatterning, a topographical control over monolayer geometry.

1.2.1 Micropatterning

Cell's physical aspects of behavior such as adhesion, traction exertion, and migration depend on changes in its morphology and topographical features. These changes depend on intracellular processes and cell interaction with the micro-environment. In cell sheets these interactions are

transmitted through cell-cell adhesions to create intercellular stress gradients [2]. As a result, cells in monolayers protrude toward the maximum principle stress [3]. Therefore, a more accurate characterization of the role of factors involved in cell's major exchange of force with its surroundings (i.e. ECM and neighboring cells) in cell islands requires precise control on colony shape and dimension. This topographical control by Micropatterning has provided better insight into mechano-transduction of ECM signals through focal adhesions and cell/cell island's mechanical response by cytoskeletal reinforcement. Two different approaches to micropattern cells in a controlled geometry include physical and biochemical confinements reviewed in the literature [4, 5]. PDMS-made thin masks have been used as temporary physical barriers on polyacrylamide gel substrates allowing monolayers to expand after mask removal [6]. However, cells settled on soft PDMS (e.g. A/B) substrates are disrupted and therefore cannot be patterned in PDMS masks.

To micropattern epithelial cells, we use custom designed 316 stainless steel sheets with laser-drilled holes (California Lasers, Simi Valley, CA) (Figure 6) as biocompatible molds to micropattern the monolayers on soft silicone substrates for measuring their traction force. In a simple and straight forward process, cells were plated on the sheet and adhered to the silicone substrate (Figure 7). After being in the incubator at 37 ℃, 5% CO_2 overnight, micropatterned monolayers with the same diameter as that of sheet holes were formed (Figure 8).
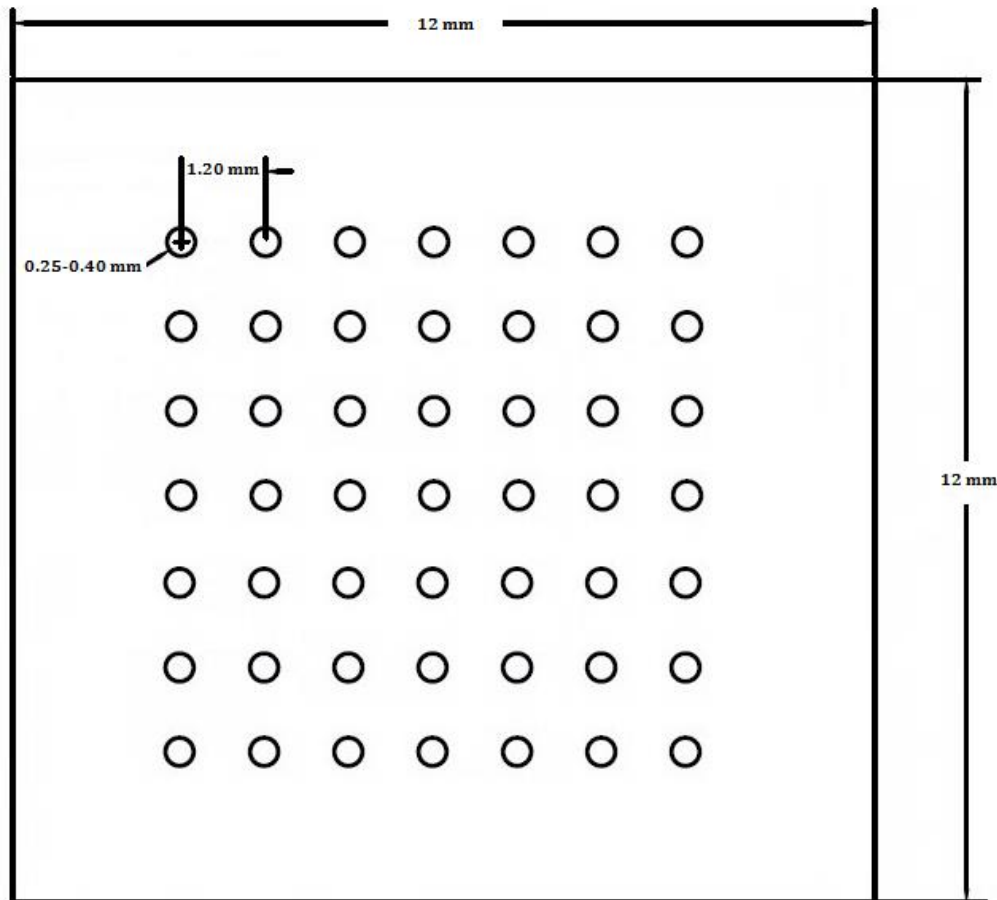
Figure 6. Thin 316 stainless steel sheets with holes of different sizes can be used for micropatterning. Cells are micropatterned in circular islands on the substrate by being plated into the sheet holes.
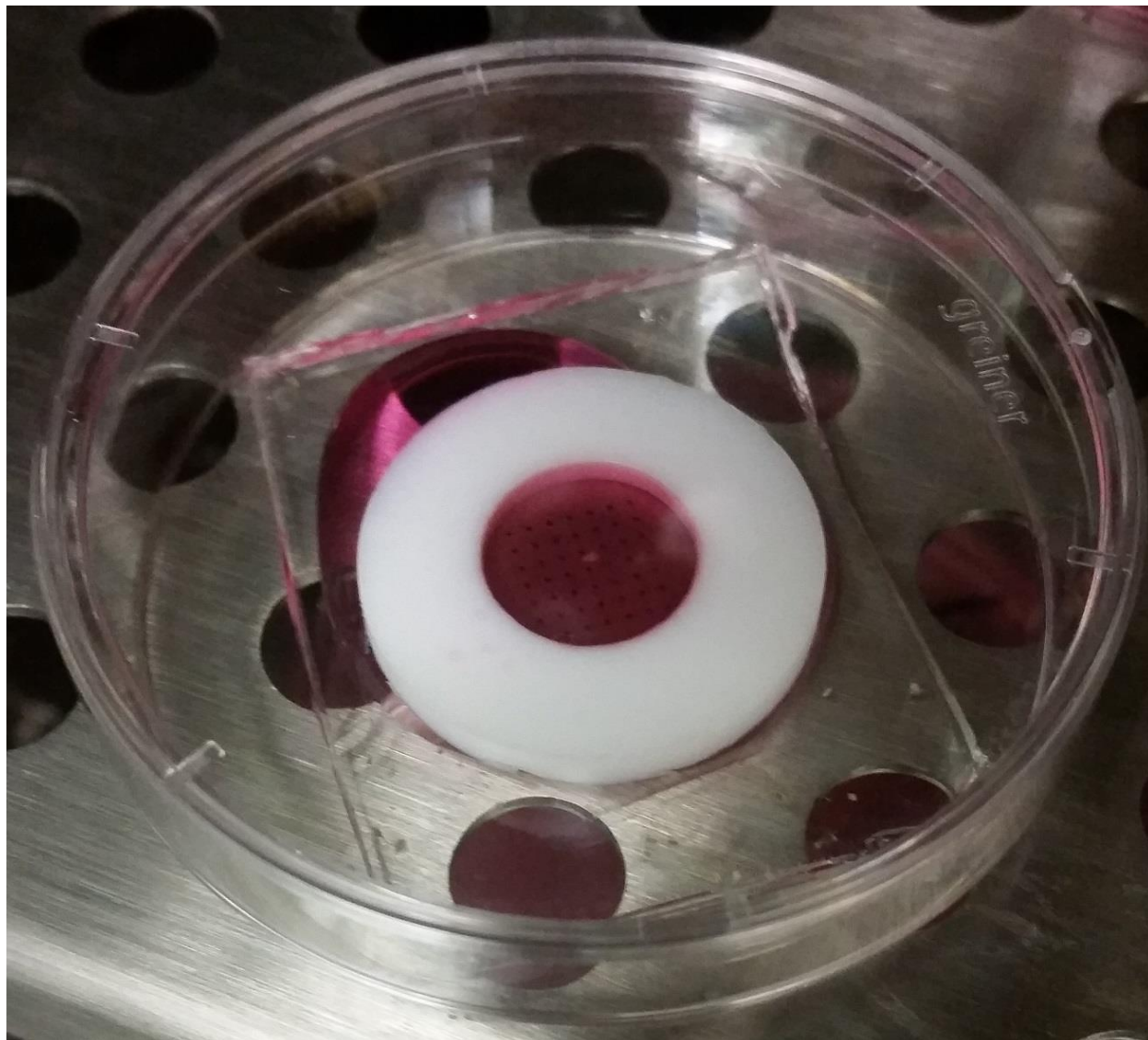
Figure 7. Cells are plated on a soft PDMS substrate masked with a perforated sheet. The sample stays in standard condition at 37 ℃, 5% CO_2 overnight to form micropatterned monolayers.
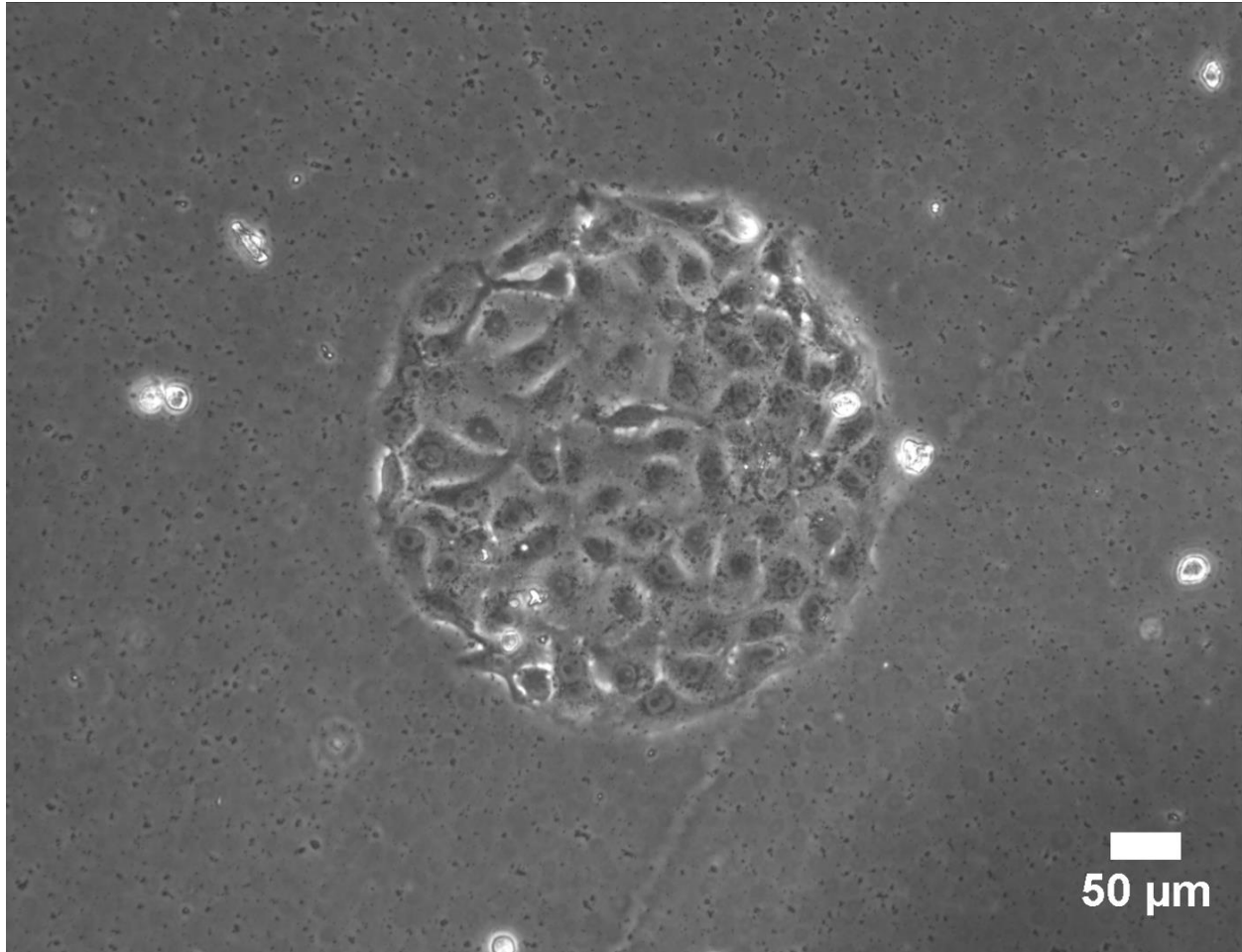
Figure 8. A micropatterned MDCK island on soft silicone substrate.

1.2.2 Fourier transform traction cytometry (FTTC)

Considering the substrate as an incompressible elastic isotropic half space [7], traction forces can be extracted by solving $X = GF$ where the knowns G and X are, the Green function and displacement vector of the substrate respectively, and F is the exerted force vector. Butler et al. [8] introduced FTTC as an efficient exact solution to this problem wherein the forces are solved for in Fourier space and inverted back to real space. Regularization has also been demonstrated to be necessary to find valid solutions for the stresses [7] and is therefore employed in the FTTC implementation in our studies. In general, soft linear elastic isotropic substrates such as

polyacrylamide (PAA) gels and PDMS (Polydimethylsiloxane) elastomers of low stiffness (Young's modulus of 0.2-20 kPa) such as CY52-276 A/B [9, 10] are proper substrates for this purpose.

Obtaining the Green function requires the elastic properties of substrate. In chapter 3 we introduce a straight forward protocol that uses sphere indentation to measure Young's modulus of substrates with low stiffness used for FTTC. We introduce a simple protocol for preparing a soft silicone sample, embedding fluorescent beads (and ECM protein such as collagen I) on the top surface of the sample, capturing phase images of indenting sphere and fluorescence imaging of the top surface of the sample and lastly processing the captured images to measure the Young's modulus of the silicone sample. The prepared soft silicone sample can be readily used for TFM experiments.

In chapter 4, FTTC was used to quantify wall shear stress field of fluid flow in a rectangular flow channel. The introduced method in chapter 4, uses a soft silicone substrate and therefore it is especially practical when it is desirable that the flow channel be entirely made of silicone (for example, to meet chemical compatibility requirements), as is common in many microfluidics applications. The protocol described in chapter 3 was employed to measure the Young's modulus of the substrate. We used particle image velocimetry (PIV) to measure flow-induced displacement in the soft substrate (wall) and deployed regularized FTTC to determine the wall shear stresses from displacement field of the wall. The theoretical measurement of wall shear stress validated FTTC for being used in microfluidics applications.

In chapter 5, FTTC was used to quantify traction forces of micropatterned epithelial cell islands under uniaxial substrate stretch. The method introduced in chapter 1 was deployed to micropattern the cells into circular islands. A custom designed stretcher (Figures. 9 and 10) capable of stretching the substrate into different strain levels (Figure 11) was used. To avoid possible hydraulic

fractures, a soft silicone was used instead of the commonly used permeable gels. The protocol described in chapter 3 was used to measure the Young's modulus of the substrate. Mechanical response of the islands to stretch was assessed by measuring traction force, strain energy, and sheet tension of control (non-stretched) and stretched islands. Immunofluorescence staining of the islands was used to assess the localization of actin cytoskeleton and E-cadherin.
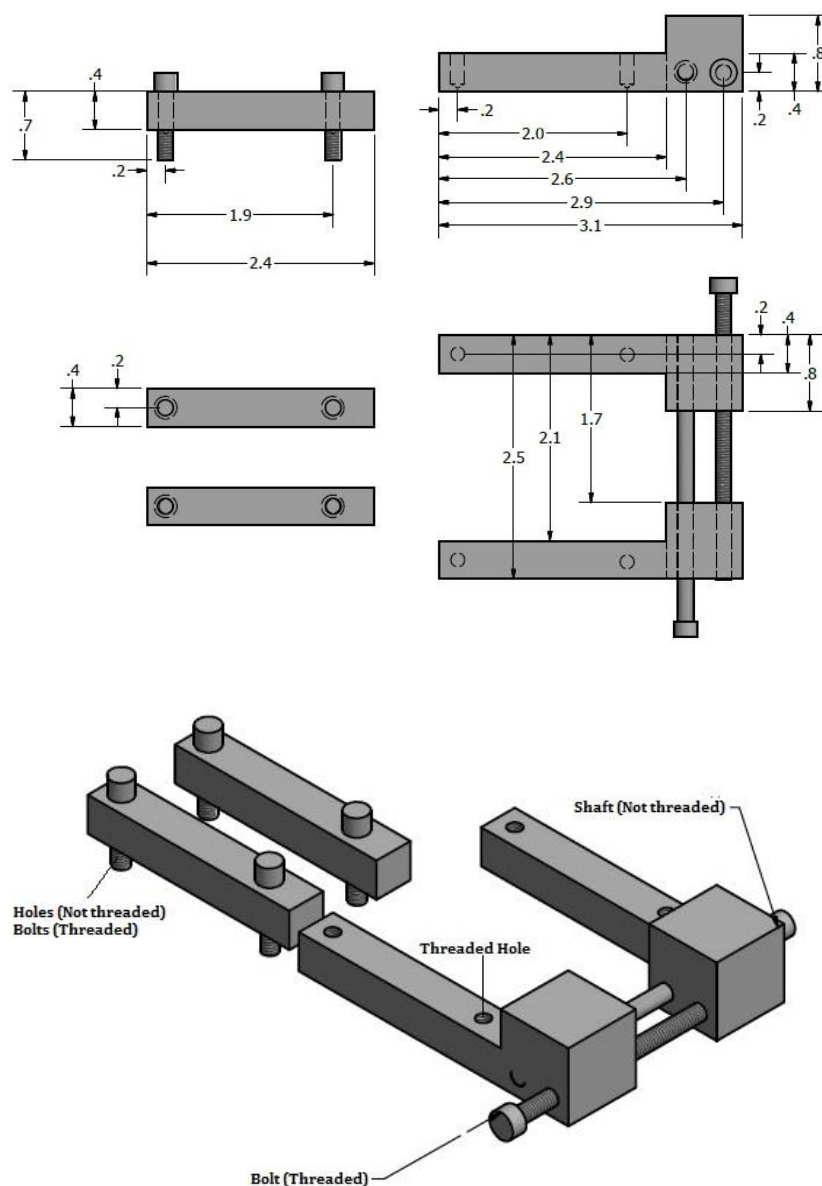
Figure 9. Custom designed substrate stretcher with detailed dimensions in inches.
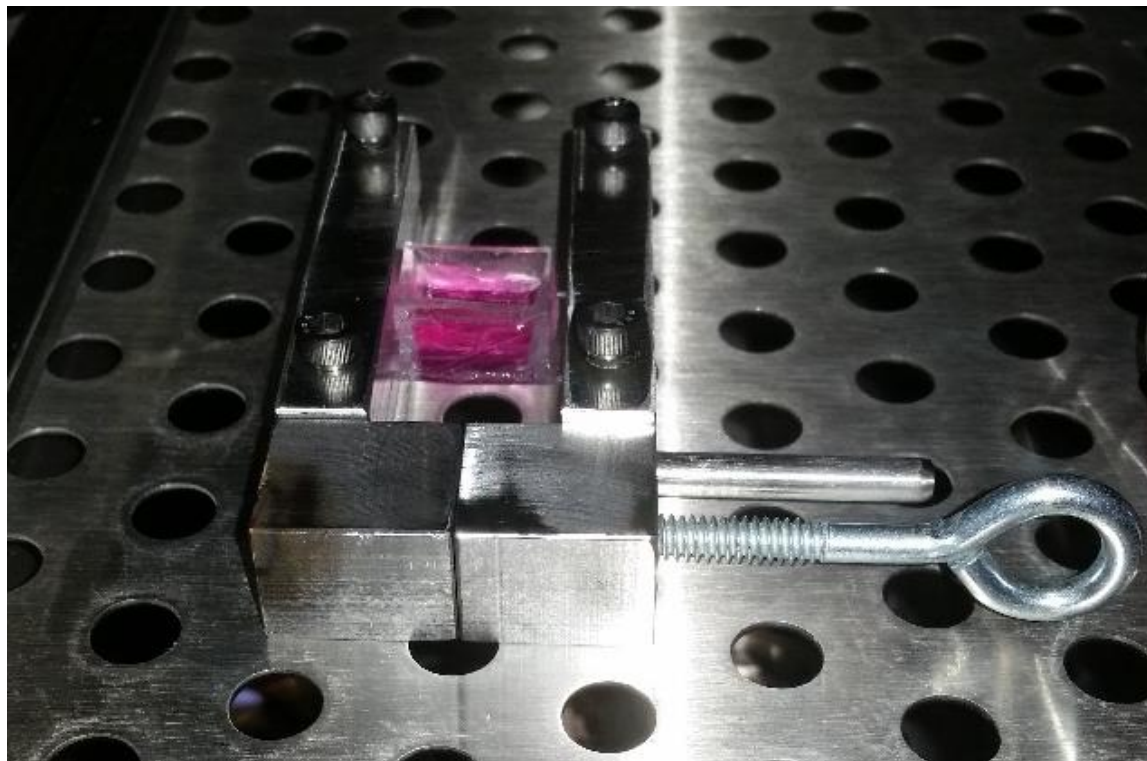
Figure 10. Sample including micropatterned monolayers in the middle is sandwiched on the stretcher. A PDMS well is used to supply cells with fresh media.
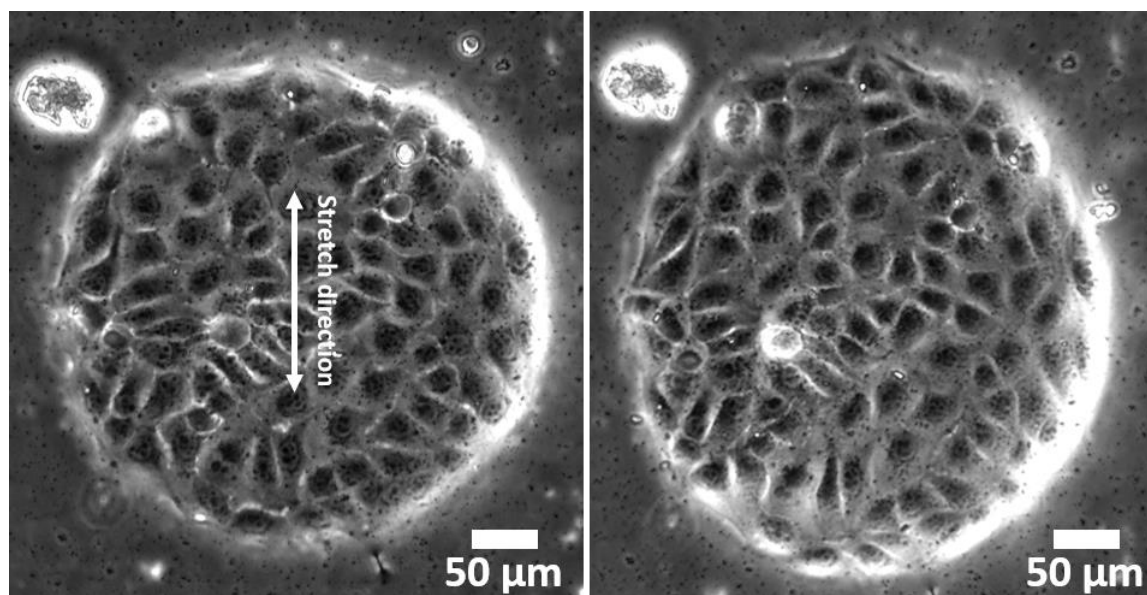
Figure 11. A micropatterned monolayer (left) stretched uniaxially (right).

CHAPTER 2

EFFECT OF PHARMACOLOGICAL MODULATION OF ACTIN AND MYOSIN ON COLLECTIVE CELL ELECTROTAXIS

Electrotaxis—the directional migration of cells in response to an electric field—is most evident in multicellular collectives and plays an important role in physiological contexts. While most cell types respond to applied electric fields of the order of a Volt per centimeter, our knowledge of the factors influencing this response is limited. This is especially true for collective cell electrotaxis, in which the subcellular migration response within a cell has to be coordinated with coupled neighboring cells. Here, we investigated the effect of the level of actin cytoskeleton polymerization and myosin activity on collective cell electrotaxis of Madin-Darby Canine Kidney (MDCK) cells in response to a weak electric field of physiologically relevant magnitude. We modulated the polymerization state of the actin cytoskeleton using the depolymerizing agent cytochalasin D or the polymerizing agent jasplakinolide. We also modulated the contractility of the cell using the myosin motor inhibitor blebbistatin or the phosphatase inhibitor calyculin A. While all the above pharmacological treatments altered cell speed to various extents, we found that only increasing the contractility and a high level of increase/stabilization of polymerized actin had a strong inhibitory effect specifically on the directedness of collective cell electrotaxis. On the other hand, even as the

effect of the actin modulators on collective cell migration was varied, most conditions of actin and myosin pharmacological modulation—except for high level of actin polymerization/stabilization—resulted in cell speeds that were similar in the absence or presence of the electric field. Our results led us to speculate that the applied electric field may largely impact the cellular apparatus specifying the polarity of collective cell migration, rather than the functioning of the migratory apparatus. Bioelectromagnetics. 39:289–298, 2018. © 2018 Wiley Periodicals, Inc.

Keywords: galvanotaxis; collective cell migration; actin polymerization; contractility; myosin inhibition

2.1. Introduction

Electrotaxis is the directional migration of cells along (or opposite to) the direction of an electric field (EF). Many types of cells have been reported to respond to EF including corneal epithelial cells and monolayers [11-13], human keratinocytes, either isolated, in pairs, or in groups [14], and tracheal epithelial cells in isolation and in monolayers [12]. The majority of the aforementioned epithelial cells migrate toward the cathode. Notably, Madin-Darby Canine Kidney (MDCK) cell sheets [12] have been reported to migrate toward the cathode [15] or anode depending on the applied electric field and MDCK sub-clone [12]. Electric fields of about 1 V/cm are known to endogenously arise in vivo when, for example, epithelial sheets are wounded [16]. Monolayers of epithelial cells also respond collectively to externally imposed electric fields of similar magnitude in vitro. Epithelial sheets show greater sensitivity in their response to EF but align more slowly than cells in isolation [17]. This collective response exhibits greater directionality [12], but the

migration rate typically slows down as cell density rises [18]. Cell-cell interactions thus play an important role in the collective response to electrotaxis.

Selective inhibition of signaling molecules has enabled the identification of key players involved in the directional electrotactic migration response of single cells and cohesive monolayers [19-26]. For example, it has been shown that the polarized formation of lamellipodia along the cathodal edge of some epithelial cells under DC (direct current) EF induces an electrotactic response toward the cathode [27]. Accordingly, the asymmetric activation of the MAP kinase ERK1/2 was shown to regulate the cathodal redistribution of the F-actin cytoskeleton, and its inhibition impaired the speed and directedness of single corneal epithelial cell migration toward the cathode [19]. Similarly, the inhibition of PI3K significantly decreased both speed and directionality of brain tumor-initiating cells in isolation under EF as well as that of MDCK epithelial monolayers [12, 26]. In addition, inhibition of PI3K switched the directional migration of single keratocytes toward the anode of an applied EF. Many of these signaling modules that influence the electrotactic response do so by acting on the actin cytoskeleton.

Previous studies modulating specific aspects of the contractile actin cytoskeleton have yielded diverse results with respect to their effect on electrotaxis. Inhibiting actin polymerization in brain tumor-initiating single cells with latrunculin B significantly weakened cell motility but their directionality toward the anode remained biased. Jasplakinolide, a promoter of actin polymerization and stabilization of F-actin, inhibited EF-induced cathodal cluster formation of muscle cells [28]. Inhibition of myosin with blebbistatin, and Rho-associated kinase with Y27632, showed little effect on single keratocyte migration toward the cathode [24]. Although myosin-II regulates cell motility [29] and its inhibition with blebbistatin could affect cell migration, neither cell motility nor the directionality of brain tumor-initiating cells in isolation was affected by it

under EF [26]. Cathode-directed migration of single keratocytes during electrotaxis was also not affected by blebbistatin [23]. On the other hand, blebbistatin inhibited cathode-directed migration of mouse epithelial fibroblasts in isolation [25]. It also abolished the anode-directed response of keratocyte fragments [24], although it had no effect on electrotaxis of keratocyte fragments when they were treated with cAMP or cGMP which are second messengers to extracellular factors [30]. In this work, we wanted to specifically test the extent to which both actin organization and the level of cell contractility influenced collective cell electro-taxis in response to an EF of physiologically relevant magnitude [31]. In particular, we wanted to determine how these modulations affected the speed and directionality of the collective electro-tactic response compared to a case with no directional cue. We applied a DC electric field (DCEF) on MDCK II monolayers in vitro without or with pharmacological inhibitors that tune actin organization or contractility either higher or lower. We found that only the state of higher contractility or the state of high degree of actin polymerization showed a large loss of directionality in response to DCEF. Importantly, we found that the effect of various pharmacological inhibitions on cell speed in the presence of EF was similar to their effect on random cell migration speeds within monolayers in the absence of EF for most treatments. The latter result suggests only a minor effect of the electric field on the migration machinery itself, compared to its effect on the cell polarization apparatus.

2.2 Materials and methods

2.2.1 Cell culture

MDCK (MDCK II, generously provided by Daniel Conway, Virginia Commonwealth University, Richmond, VA) cells were cultured with DMEM (Dulbecco's modified Eagle's medium, Corning, Corning, NY) supplemented with L-Glutamine, sodium pyruvate, 1% Penicillin/Streptomycin, and

10% Fetal Bovine Serum (FBS) (Corning) at 37 8C and under 5% CO2. For electrotaxis experiments, the chamber in which cells were plated was prepared as follows [32]: first, a Polydimethylsiloxane (PDMS) well of $10 \times 8mm^2$ inner area was placed in a 60-mm polystyrene petri dish (to confine the cells to the PDMS well region). Then, a 30×22 mm^2 glass coverslip was cut in two and the two halves were glued to the petri dish parallel to each other surrounding the two sides of the PDMS well (supplementary Figure S1). Then four 3140 silicon rubber barriers were made on opposite sides of the cover slips as shown in supplementary figure S1a. The region of the chamber confined by the PDMS well was coated with a 0.2 mg/ml solution of Col1 in 0.1 M acetic acid at 37 8C for 15 min. After washing with PBS, the cells were plated in the PDMS well and maintained in the incubator (at 37 8C and 5% CO2) overnight to form an approximately $10 \times 8mm^2$ rectangular monolayer (with minor imperfections in the vicinity of the well) adherent to the chamber substrate. Then, the PDMS well was removed, a coverslip was glued onto the sidewall coverslips, and freshly prepared media supplemented with 10 mM HEPES was added to the chamber as in supplementary figure S1b. For experiments involving cell treatment with pharmacological inhibitors, fresh media containing 10 mM HEPES and inhibitor at the appropriate concentration as mentioned was added to the chamber 1 h prior to the experiment.

2.2.2 Electrotaxis chamber

An electrotaxis chamber similar to that introduced by Song et al. [32] was used to apply DCEF to cells in vitro. Steinberg's solution (60 mM NaCl, 0.7 mM KCl, 0.8 mM MgSO4.7H2O, 0.3 mM Ca(NO3)2.4H2O, 1.4 mM Tris base, pH 7.4) in two petri dishes was used as the electrolyte solution. Agar salt bridges were prepared as follows: 2% wt/vol agar powder was dissolved in Steinberg's solution, heated until boiling, then cooled to approximately 60 8C and then injected

into Π-shaped glass tubes prepared by heating and bending 10 cm long glass tubes with a laboratory burner. The agar subsequently gelled as it cooled. The gelled agar bridges were then inserted into the chamber in contact with the cell media at the two ends of the chamber. EF of the desired direction was achieved by microscopic alignment of the two bridges. Two silver wire electrodes were inserted into the electrolytes (as in Figure 12a), and two connectors from the poles of a DC supply (Circuit Specialists, CSI20002S, Tempe, AZ) were connected to the electrodes to close the loop. The uncertainties associated with all of the following voltage and current values are due to limited increment values of the digital read-outs (from two independent measurements). The voltage applied by the power supply was 20 ± 1 V leading to a voltage of 2.40 ± 0.12 V and a current of 0.17 ± 0.01 mA measured via a multimeter (M-1750 Elenco, Wheeling, IL) between the ends of the agar bridges in the cell chamber, with a distance of 4.5 ± 0.1 cm between them. The magnitude of the EF across the chamber was thus calculated to be 0.53 ± 0.03 V/cm.
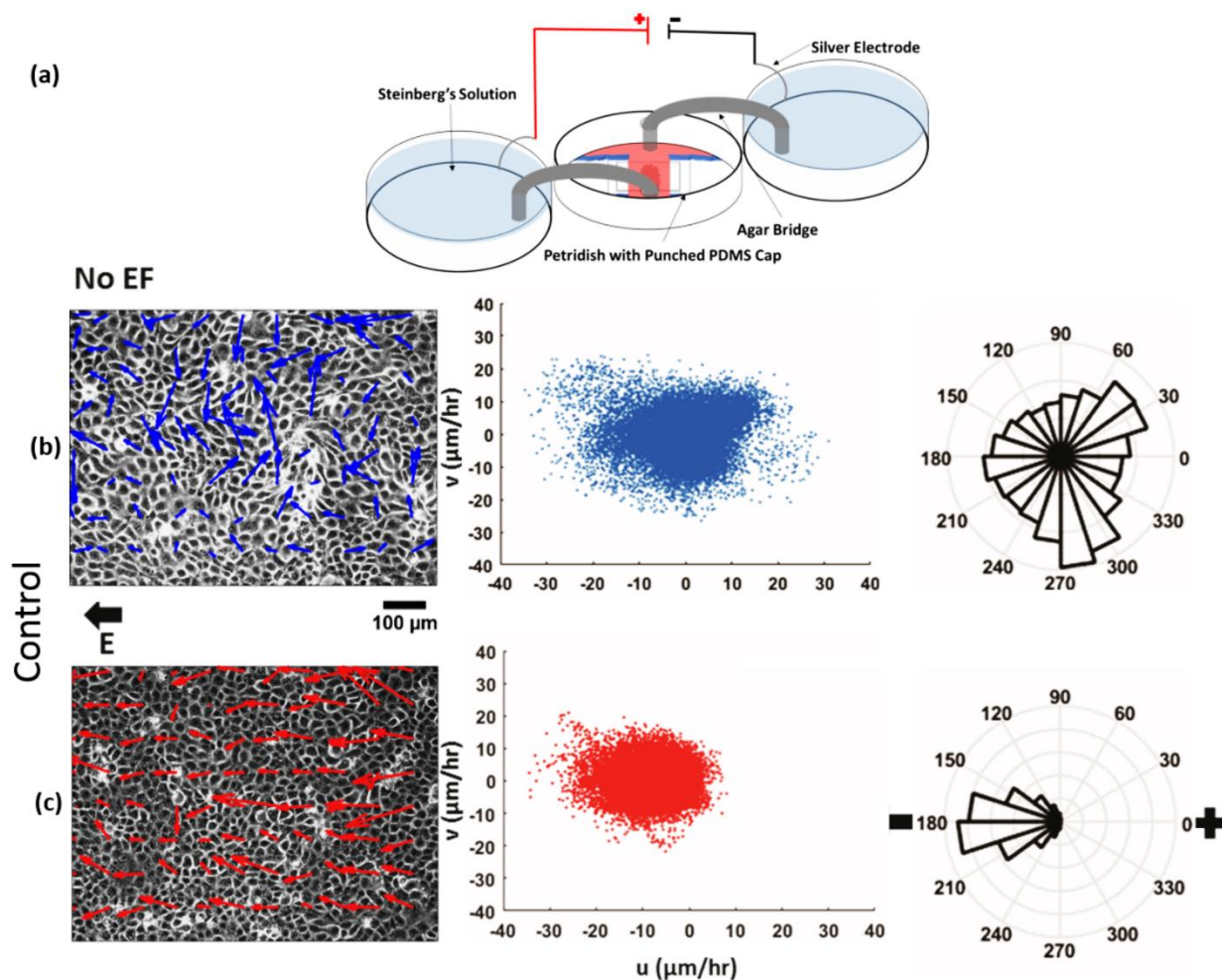
Figure 12. Collective electrotaxis of MDCK cells in the absence of any pharmacological modulation. (a) Schematic illustration of sample configuration used for application of DC EF to monolayer (based on set-up in [32]; please see Materials and Methods section). (b) Phase image of a 860×640 μm^2 region of monolayer superimposed with average local velocity vectors (averaged over 1h) at different locations within region as determined using PIV. A scatter plot of all of the average local cell velocity components for local cell velocities and a rose plot of their angular distribution are shown on the right (based on a total of ~4 $\times 10^4$ velocity vectors). (c) Phase image of a 860×640 μm^2 region of the monolayer subject to an electric field of 0.53 ± 0.03 V/cm superimposed with average local velocity vectors (averaged over 1h) at different locations within region as determined using PIV. Electric field direction is indicated above (labelled "E" with direction). A scatter plot of all of the average local cell velocity components for local cell velocities and a rose plot of their angular distribution are shown on right (based on a total of ~ 4 $\times 10^4$ velocity vectors). Directedness was d = 0.81. For angular rose plots, cathode is at 18° and anode at 0°.

2.2.3 Pharmacological inhibitors

The pharmacological inhibitors jasplakinolide (Cayman Chemical, Ann Arbor, MI), cytochalasin D (MP Biomedicals, Santa Ana, CA), blebbistatin (Cay-man Chemical), and calyculin A (MP Biomedicals, Santa Ana, CA) were used in the following concentrations: Cytochalasin D was effective at 0.2 mMas assessed by immunofluorescence (supplementary Figure S2). Blebbistatin was used at 20 mM as its solubility was reported to decrease beyond this concentration [Varkuti et al., 2016]. Higher concentrations such as 50 mM also resulted in MDCK cell–cell contact breakage (supplementary Figure S3). Calyculin A was used at 5 mM, the concentration at which contractility-dependent traction forces have been specifically shown to increase [Stricker et al., 2011]. Jasplakinolide is typically used in a relatively wider range (1–500 nM) of concentrations [Wan et al., 2011]. We thus used jasplakinolde at 1 nM (low), 50 nM (high), and 500 nM (highest)—use at 500 nM resulted in MDCK cell-cell contact breakage and disruption of monolayer integrity and hence was excluded from further consideration. It is important to note that pharmacological inhibitions as assessed above do not imply complete inhibition of intended biochemical targets.

2.2.4 Time-lapse imaging of electrotaxis

The electrotaxis experiments were imaged using an inverted microscope (DMI8, Leica Microsystems, Wetzlar, Germany) equipped with an air stream incubator (Nevtek, Williamsville, VA). The petri dishes' caps were replaced with a PDMS cap with punched holes to install the agar bridges into the chamber as in figure 12a. Electrolyte solutions were then connected with DC power supply via silver electrodes. Figure 12a shows the electrotaxis chamber equipped with electrochemical equipment for application of DCEF. From the MDCK II monolayer of area ~10

$\times 10$ mm^2, phase images of the cells within multiple positions in the central region (of $\sim 5 \times 4$ mm^2 area) of the monolayer were captured by time-lapse imaging-first with no EF for at least 1 h and then upon EF application for 2 h. Two independent experiments were conducted for each case, without or with EF, or without or with specified pharmacological inhibitor. The cell density was found to be (based on cell number data in two different regions of area 0.6 mm2 each, for all cases) 1472 ± 60 cells/mm2 for the control case, 1577 ± 52 cell/mm2 for the blebbistatin treated case, 1367 ± 67 cells/mm2 for the jasplakinolide (low) treated case, 1468 ± 230 cells/mm2 for the jasplakinolide (high) treated case, and 1407 ± 13 cells/mm2 for the calyculin A treated case. Thus, cell density variations between untreated and any inhibitor-treated case was 7% or less. In general, the cells responded to EF within 1 h and so the time lapse sequence of migration for at least a 1 h time period with no EF and a 1 h time period with EF (the time period from 1 h to 2 h after EF application, for all cases) was analyzed by PIV (particle image velocimetry).

2.2.5 Quantification of cell migration due to electrotaxis

PIVlab (version 1.41) [33], an open source MATLAB (R2015b, Math-Works, Natick, MA) program for cross-correlation, was used to process the sequence of cell phase images during random and electrotactic cell migration. First, image preprocessing, including defining a region of interest (ROI) and removing background noise, prepared the image sequences for velocimetry [Bashirzadeh et al., 2016]. PIVlab was then used to employ the Fast Fourier Transform (FFT) method with 50% overlapped interrogation windows of 64×64 pixels^2 and 32×32 pixels^2 in two passes to quantify the displacement of the cells between successive pairs of images resulting in a velocity vector field for each successive image. The MATLAB built-in function "rose" was used to depict the directionality of monolayers in an angle histogram plot. Mean of the cosine of the

angle (θ) between velocity vectors of monolayers ($d = \frac{\sum \cos \theta}{n}$) and the direction of the electric field was used as the measure of the directedness d of the migration where n is the total number of velocity vectors calculated in different regions of the monolayer. Directedness and the speed of cells in monolayers have been calculated for each case based on $3–4.5 \times 10^4$ data points. Two-way ANOVA was used to test the statistical significance of main effects (EF vs no EF as well as inhibitor vs no inhibitor) and interaction effects (in the presence of both EF and inhibitor) with P-values <0.01 considered significant. Tukey's honest significant difference criterion was used for multiple comparisons.

MDCK II epithelial monolayers were fixed with 4% w/v paraformaldehyde (Electron Microscopy Sciences, Hatfield, PA) and permeabilized with 0.5%v/v Triton X–100 (Thermo Fisher Scientific, Waltham, MA) following standard procedures [Maruthamuthu and Gardel, 2014]. Purified mouse anti-b-catenin (BD Transduction Laboratories, BD Biosciences, San Jose, CA) at a 1:100 dilution and phalloidin (Alexa Fluor, Thermo Fisher Scientific) at a 1:200 dilution were used to stain the cells. Rhodamine-goat anti-mouse (Thermo Fisher Scientific) secondary anti-body was used at a 1:200 dilution. A 20x objective lens was used for immunofluorescence imaging.

2.3. Results and discussion

2.3.1 Migration of MDCK monolayers toward the cathode in response to applied DCEF

We applied a physiologically relevant [31] weak DC field of 0.53 ± 0.03 V/cm to MDCK II monolayers (of area ~10×8 mm^2) in the electrotaxis chamber (Figure 12a). This EF magnitude is at the lower end in the range used to elicit a response from MDCK cells previously [12, 15] and is in the range of endogenous wound EF in humans and animal cells [34-36]. We found that the MDCK cells exhibited a clear cathode-directed response (d = 0.81, P < 0.01) (Figure 12b–d) in

response to this DCEF. Although various types of single cells and epithelial sheets respond to EF, epithelial cells in isolation have been reported to respond either slower or not at all to weak EFs [12]. This suggests that cell–cell coupling in epithelial sheets plays a critical role in the collective response. In fact, blocking E-cadherin or depletion of extracellular Ca2þ has been shown to abolish electrotaxis in MDCK monolayers [12]. We therefore wanted to test if impairment of the cadherin-actin link by a-catenin knock-down would affect MDCK mono-layer electrotaxis. However, we found that a-catenin knock-down inhibited even random cell migration within monolayers in the absence of EF. Expectedly, migration under EF was also essentially completely inhibited (Supplementary Video S6). This result reinforced the importance of the link between cell-cell contacts and actin cytoskeleton of epithelial cells in cell migration within monolayers, with or without EF.
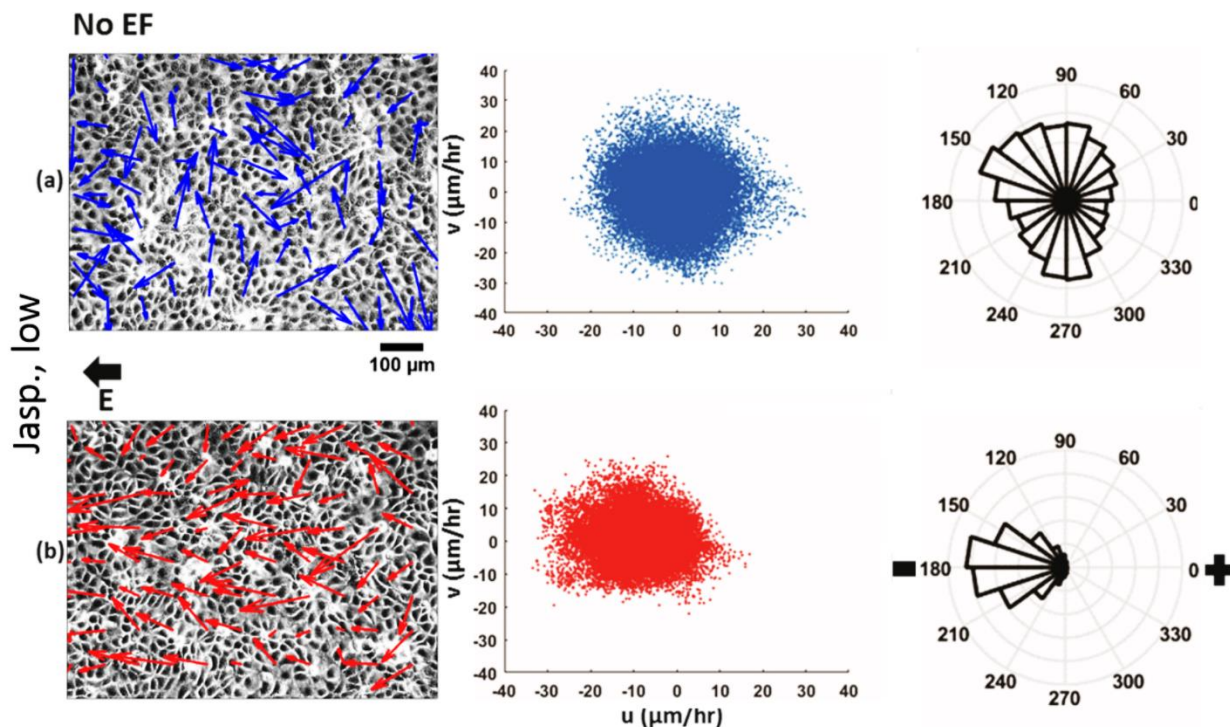
Figure 13. (a) Phase image of a 860×640 μm^2 region of monolayer pre-treated with 1nM jasplakinolide superimposed with average local velocity vectors (averaged over 1h) at different locations within region as determined using PIV. A scatter plot of all of the average local cell velocity components for local cell velocities and a rose plot of their angular distribution are shown on right (based on a total of $\sim 4.5 \times 10^4$ velocity vectors). (b) Phase image of a 860×640 μm^2 region of monolayer pre-treated with 1nM jasplakinolide subject to an electric field of 0.53 ± 0.03 V/cm superimposed with average local velocity vectors (averaged over 1h) at different locations within region as determined using PIV. Electric field direction is indicated above (labelled "E" with direction). A scatter plot of all of the average local cell velocity components for local cell velocities and a rose plot of their angular distribution are shown on right (based on a total of $\sim 4.5 \times 10^4$ velocity vectors). Directedness was d = 0.74, slightly but significantly less than that for the control case (P<0.01). For angular rose plots, cathode is at 18° and anode at 0°.

2.3.2 Promoting actin polymerization perturbs electrotaxis

Elongation of leading edge involving actin polymerization is one of the primary steps of cell migration and is therefore also essential during electrotaxis. To test the effect of F-actin stabilization on MDCK monolayer electrotaxis, we treated the cells with either a low (1 nM) or high (50 nM) concentration of jasplakinolide [37]. Jasplakinolide is a marine sponge toxin that induces actin polymerization [38] and can impact the kinetic and kinematic signatures of lamellipodia [39]. It is a potent inducer of actin polymerization in vitro by stimulation of actin filament nucleation [40] in a manner not controlled by cellular signaling [22, 38]. Typically, inhibiting polymer disassembly with jasplakinolide bound to actin filaments could disrupt normal cell motility [41]. Here, jasplakinolide at 1 nM treatment slightly enhanced cell migration speeds during both random cell migration with no EF and electrotactic collective response of MDCK monolayers to EF (compared to untreated case, main effect $P < 0.01$, 2-way ANOVA). Figure 13 shows a representative vector field (Figure 13a) along with the velocity scatter plot (Figure 13b) and directionality of the monolayer (Figure 13c) treated with jasplakinolide. Cathode-directed electrotactic migration is slightly disturbed with 1 nM jasplakinolide treatment ($d = 0.74$, interaction effect $P < 0.01$, 2-way ANOVA). However, treatment with jasplakinolide at 50 nM led to abrogation of the cathode-directed response to EF (Figure 14, interaction effect $P < 0.01$, 2-way ANOVA). Even though the cell velocities were largely preferentially oriented along the EF axis, as evident in the velocity scatter plot in figure 14b, the directedness (toward the cathode) was close to zero ($d ¼ 0.001$). On the other hand, depolymerization of actin filaments by the addition of 0.2 mM cytochalasin D [42] ceased collective cell migration both without and with EF (Supplementary Video S7), as expected, confirming the necessity of a basal level of F-actin to enable cell migration.
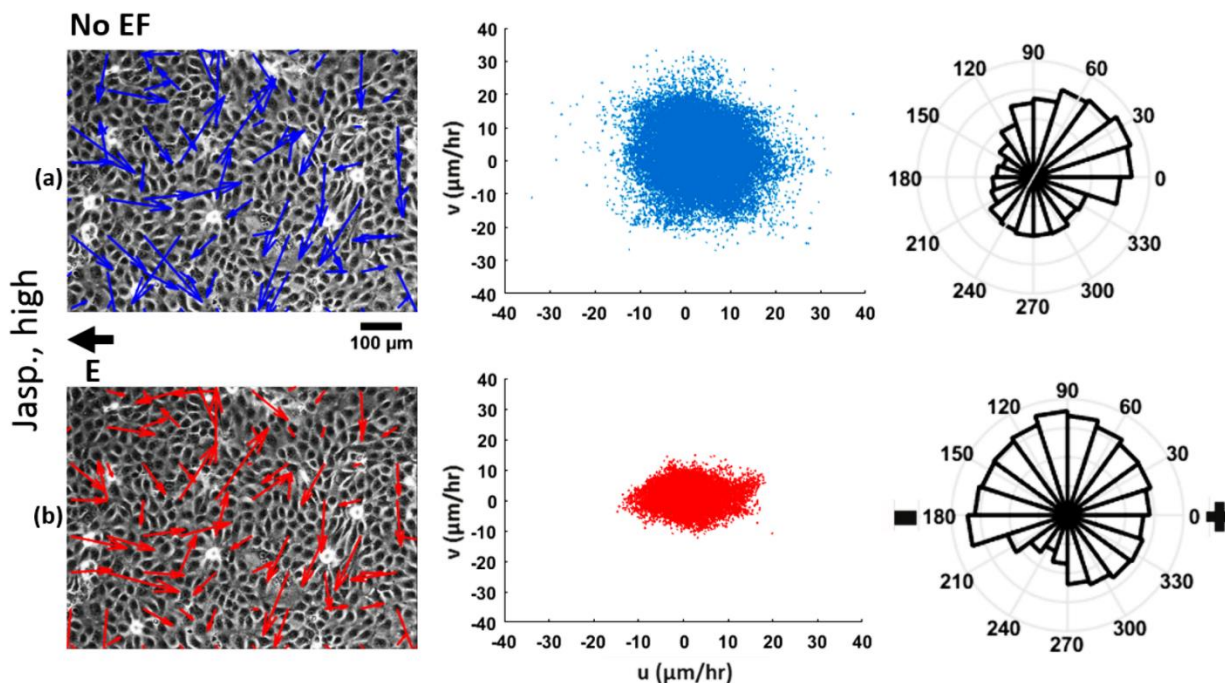
Figure 14. (a) Phase image of a 860×640 μm^2 region of the monolayer pre-treated with 50 nM jasplakinolide superimposed with the average local velocity vectors (averaged over 1 h) at different locations within the region as determined using PIV. A scatter plot of all of the average local cell velocity components for local cell velocities and a rose plot of their angular distribution are shown on the right (based on a total of ~ 3×10^4 velocity vectors). (b) Phase image of a 860×640 μm^2 region of the monolayer pre-treated with 50 nM jasplakinolide subject to an electric field of 0.53 ± 0.03 V/cm superimposed with the average local velocity vectors (averaged over 1 h) at different locations within the region as determined using PIV. Electric field direction is indicated above (labelled 'E' with direction). A scatter plot of all of the average local cell velocity components for local cell velocities and a rose plot of their angular distribution are shown on the right (based on a total of ~ 3×10^4 velocity vectors). Directedness was d = 0.001, significantly less than that for the control case (p < 0.01). For the angular rose plots, cathode is at 180^0 and anode at 0^0.

2.3.3 Increase, but not a decrease, in cell contractility inhibits electrotaxis

To test the role of myosin-based contractility in directional migration of cohesive monolayers, we treated the monolayer with 20 mM [43] of blebbistatin [44]. Blebbistatin is a rapid inhibitor of myosin II ATPases [45, 46] and thus decreases cell contractility. Here, application of blebbistatin to MDCK II monolayers slowed down both random migration of cells at no EF and their collective response to EF (compared to untreated case, main effect $P < 0.01$, 2-way ANOVA) (Figure 15a and b), even though the effect of blebbistatin on the directionality of the monolayer toward the cathode under EF was not significant ($d = 0.76$, interaction effect $P = 0.57$, 2-way ANOVA) (Figure 15c). This result suggests that reduced contractility does not impair the EF direction-sensing mechanism even though the migration speed is reduced. Slowing down of the collective cell migration of blebbistatin-treated epithelial monolayers may also reflect the disruption of the robust coupling between neighboring cells through cell-cell adhesions.

In contrast to the effect of lowering the contractility, increasing the level of contractility by treating the monolayers with 5 nM calyculin A [47] significantly attenuated cathode-directed electrotaxis of the MDCK monolayers ($d = 0.12$, interaction effect $P < 0.01$, 2-way ANOVA). Calyculin A inhibits protein phosphatases and thus promotes myosin activity by inhibiting myosin light chain phosphatase [48, 49]. Although cells treated with calyculin A showed impaired directedness toward the cathode under EF, calyculin A only had a minor (but statistically significant) effect on cell speed compared to the untreated case, either without or with the application of EF (compared to untreated case, main effect $P < 0.01$, 2-way ANOVA) (Figure 16). It should be noted that while calyculin A-induced enhanced contractility has been reported in literature [50], we cannot rule out that calyculin A-induced phosphorylation of other molecular players may have also additionally impacted the electrotactic response.
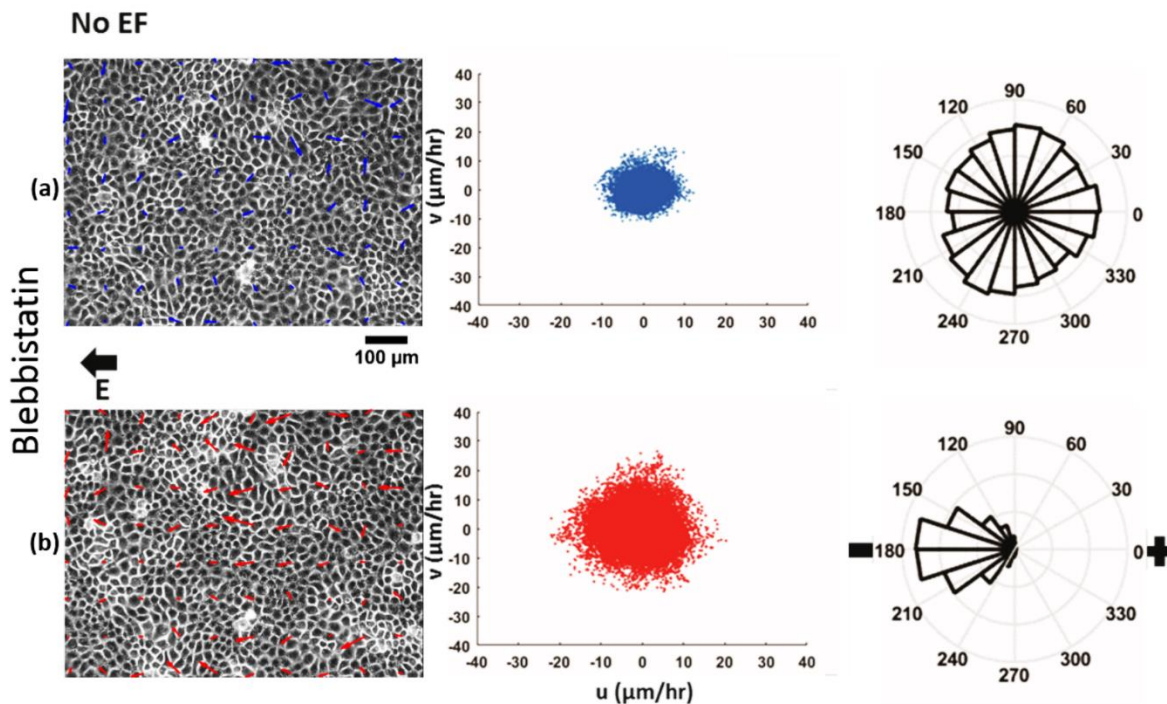
Figure 15. (a) Phase image of a $860 \times 640 \ \mu m^2$ region of the monolayer pre-treated with 20 μM blebbistatin superimposed with the average local velocity vectors (averaged over 1 h) at different locations within the region as determined using PIV. A scatter plot of all of the average local cell velocity components for local cell velocities and a rose plot of their angular distribution are shown on the right (based on a total of $\sim 3 \times 10^4$ velocity vectors). (b) Phase image of a $860 \times 640 \ \mu m^2$ region of the monolayer pre-treated with 20 μM blebbistatin subject to an electric field of 0.53±0.03 V/cm superimposed with the average local velocity vectors (averaged over 1 h) at different locations within the region as determined using PIV. Electric field direction is indicated above (labelled 'E' with direction). A scatter plot of all of the average local cell velocity components for local cell velocities and a rose plot of their angular distribution are shown on the right (based on a total of $\sim 3 \times 10^4$ velocity vectors). Directedness was d = 0.76, slightly but significantly less than that for the control case (p < 0.01). For the angular rose plots, cathode is at 180^0 and anode at 0^0.

Recent experiments with keratocytes and a corresponding 'compass' model [24] suggest that two competing intracellular pathways bias a cell along the direction of the applied EF. Actin polymerization influences the strength of the "frontness" cue [24] in this model, directing the cells toward the cathode whereas contractility promotes migration toward the anode by inducing the rear of the cell to point toward the cathode. The effect of calyculin A on collective cell electrotaxis as reported here is consistent with the proposed compass model [24] of electrotaxis: higher contractility as a result of treatment with calyculin A may promote the "backness" cue to point toward the cathode (and the cell to point toward the anode) in opposition to the cells' normal electrotactic response toward the cathode. These opposing factors could well have resulted in the low level of directedness as reported above upon calyculin A treatment. In contrast, decrease of contractility using blebbistatin is expected to suppress the backness cue, leaving the frontness cue to dominate and point toward the cathode as in the untreated case. Promoting actin polymerization with a low concentration of jasplakinolide is expected to similarly maintain cathode directedness by promoting the frontness cue, but higher jasplakinolide concentrations may impair the dynamic rearrangements of the actin cytoskeleton that are still necessary for persistent migration.
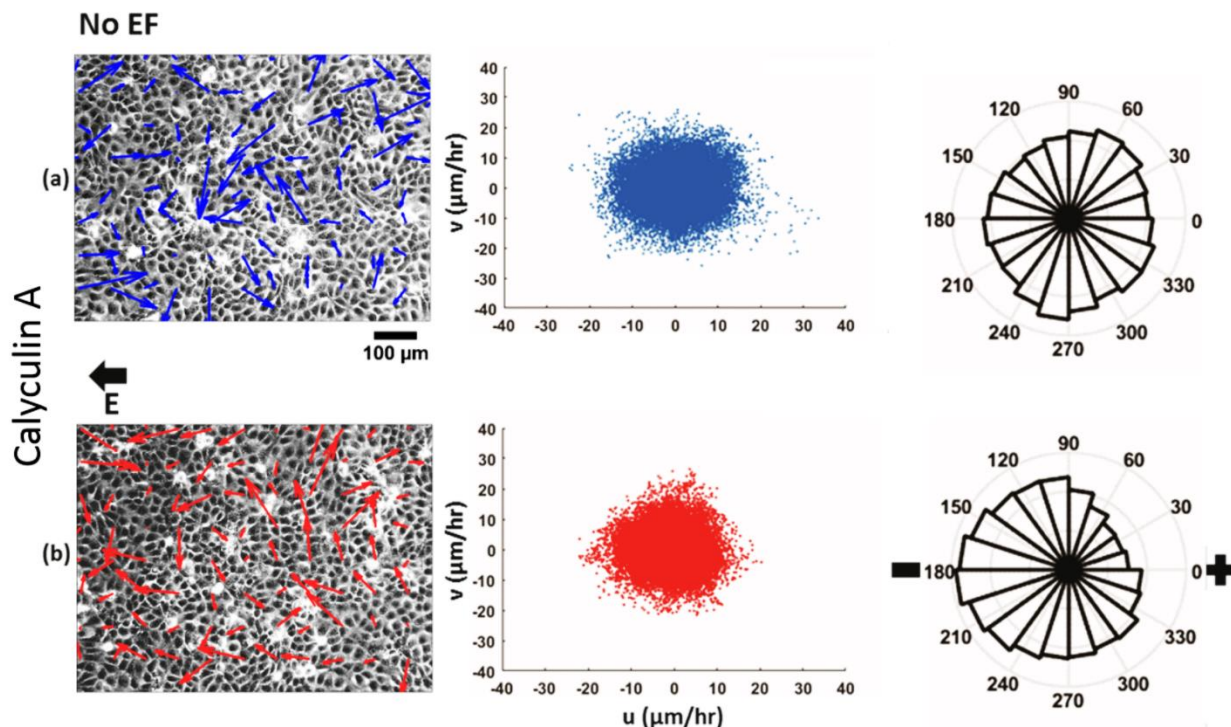
Figure 16. (a) Phase image of a 860×640 µm^2 region of the monolayer pre-treated with 5 nM calyculin A superimposed with the average local velocity vectors (averaged over 1 h) at different locations within the region as determined using PIV. A scatter plot of all of the average local cell velocity components for local cell velocities and a rose plot of their angular distribution are shown on the right (based on a total of ~ 4.5×10^4 velocity vectors). (b) Phase image of a 860×640 µm^2 region of the monolayer pre-treated with 5 nM calyculin A subject to an electric field of 0.53 ± 0.03 V/cm superimposed with the average local velocity vectors (averaged over 1 h) at different locations within the region as determined using PIV. Electric field direction is indicated above (labelled 'E' with direction). A scatter plot of all of the average local cell velocity components for local cell velocities and a rose plot of their angular distribution are shown on the right (based on a total of ~ 4.5×10^4 velocity vectors). Directedness was $d = 0.12$, significantly less than that for the control case ($p < 0.01$). For the angular rose plots, cathode is at 180^0 and anode at 0^0.

2.3.4 Electric field appears to largely affect cell polarity rather than cell migration speeds

Electrotactic cell motility was affected to various extents by the specific pharmacological agents used in this study. The differential effect of these treatments on cell speed in the presence of EF was statistically significant in all cases. However, we wanted to assess the magnitude of change affected by these different inhibitor treatments in the absence or presence of EF. Figure 17 compares the average random speeds in the absence of EF and electrotactic migration speeds in the presence of EF of inhibitor-treated monolayers. Except for jasplakinolide treatment at the higher concentration, which may have affected the cell's ability to undergo persistent directional migration, the magnitude of cell speeds without EF and with EF were similar in magnitude (although the differences among them were statistically significant, Figure 17). These results may suggest that the EF primarily affects the components of the cell polarization pathway rather than that of the cell migration machinery.
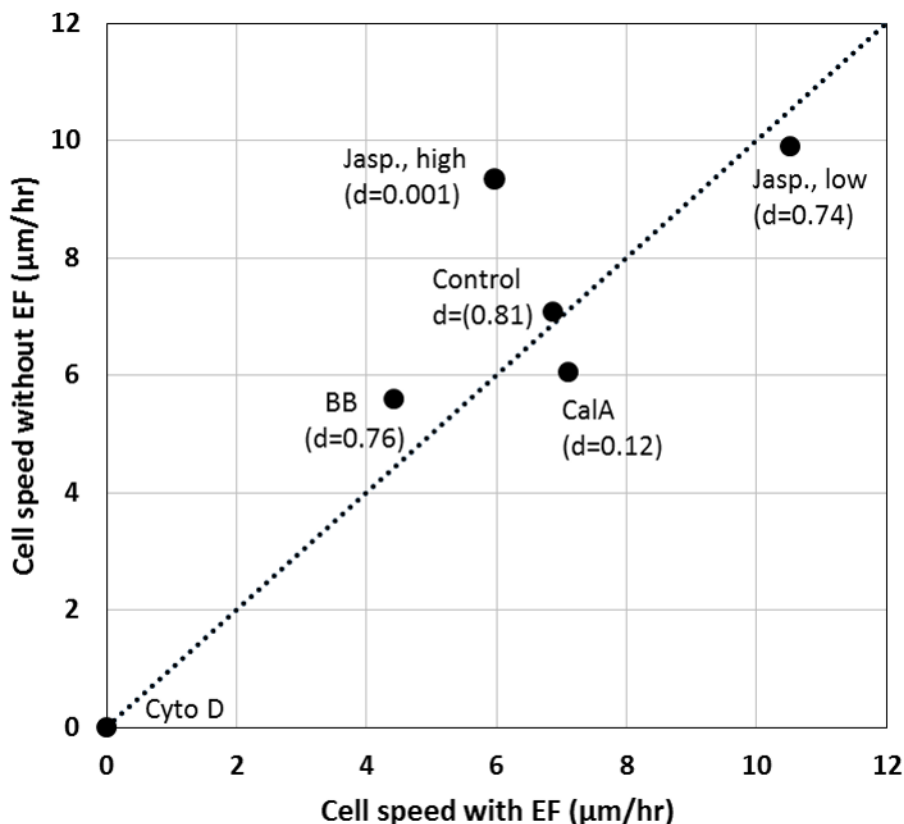
Figure 17. Average local cell speed (filled circles) within MDCK monolayers without EF is plotted against that with EF, with control as well as different pharmacological treatments as indicated. Dotted line indicates a line of slope 1 through the origin. The standard error of the mean in all cases was less than the size of the filled circles and therefore not depicted. Directedness (as defined in *Materials and Methods*) of collective cell migration in each case is shown in brackets, with a directedness of 1 corresponding to uniformly directed collective migration towards the cathode and a directedness of 0 corresponding to no preferential migration towards the cathode.

2.4 Conclusion

Cathode-directed collective migration response of MDCK monolayers to EF was tested under a range of pharmacological perturbations to the actomyosin machinery. We found that both

treatment with calyculin A and the higher concentration of jasplakinolide nearly eliminated the directedness of cells in response to EF. In contrast to directedness, cell speed in the presence of EF was affected by the pharmacological agents perturbing both actin polymerization state and myosin activity to various extents. However, the motility of the cells in the monolayer in most cases was largely conserved in magnitude between the cases without and with EF, except for actin stabilization using higher jasplakinolide concentration. Based on our results, we speculate that EF has a stronger effect on cell migration directionality rather than on cell migration capacity per se during collective cell response to EF.

AUTHORS' CONTRIBUTIONS

Yashar Bashirzadeh conducted the experiments, analyzed the data, and wrote the manuscript. Jonathan Poole also conducted experiments. Shizhi Qian contributed to the design of the experiments. Venkat Maruthamuthu conceived and designed the experiments, and revised the manuscript.

2.5 Supporting information
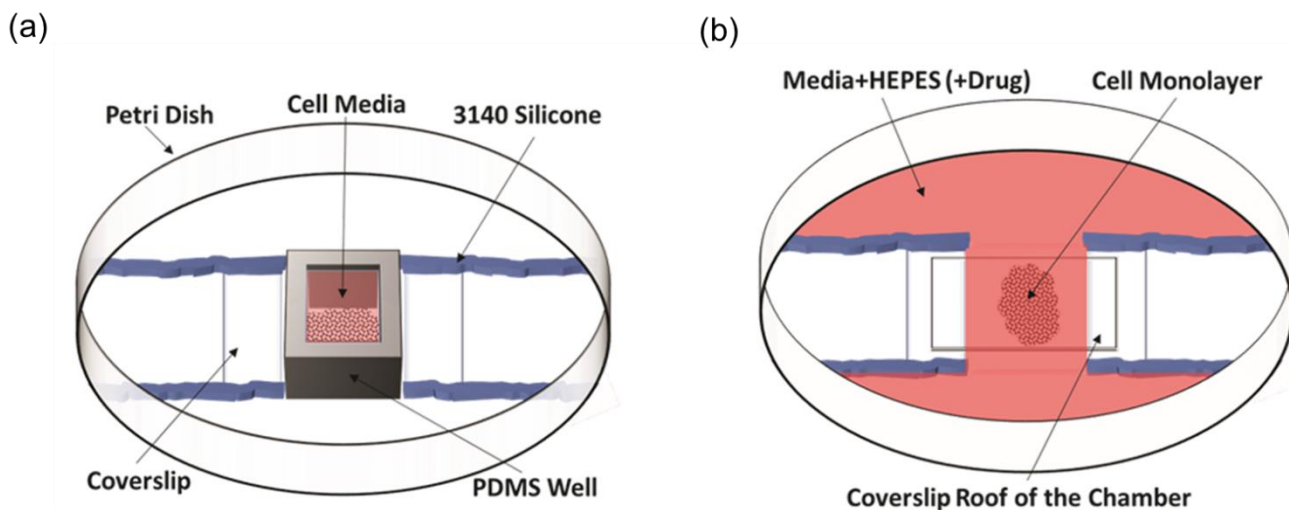
Figure S1. Schematic depiction of the preparation of the sample chamber used for the application of EF, as adapted from [32]. (a) Configuration of the petri dish with a PDMS well within which cells were plated. (b) The PDMS well was replaced with a coverslip as a roof over the cells and the media was supplemented with 10 mM HEPES as well as any pharmacological inhibitors as necessary. 3140 silicone used as a barrier to confine media as indicated.
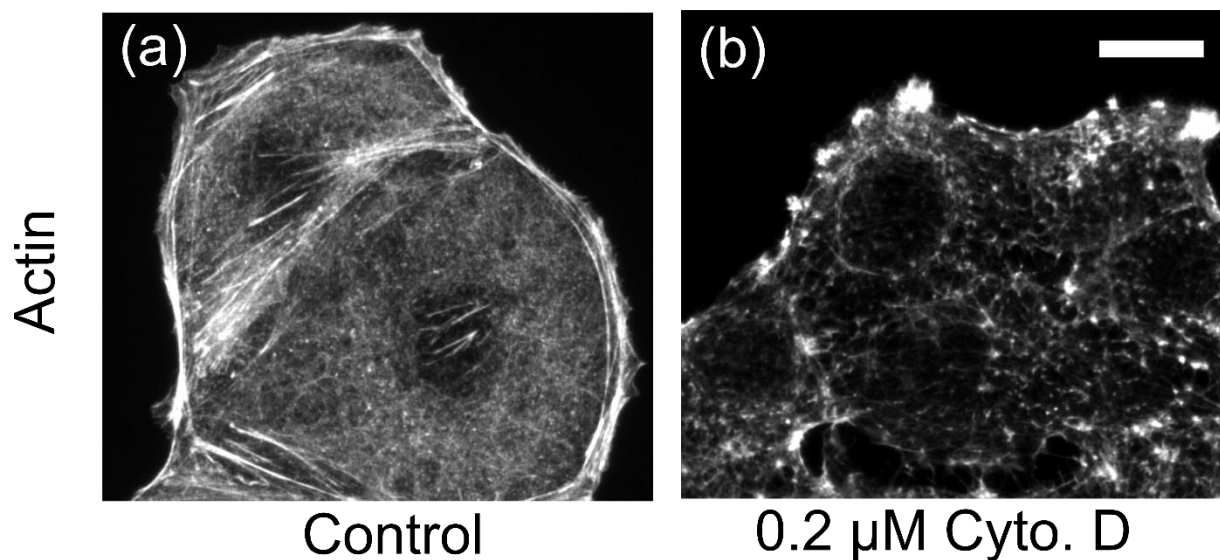
Figure S2. Immunofluorescence images of MDCK stained for actin (with phalloidin), either (a) untreated (control) or (b) treated with 0.2 µM cytochalasin D for 1 h. Notice the well-defined actin cytoskeleton in the control case and the disassembled actin cytoskeleton in the treated case. Scale bar is 20 µm.
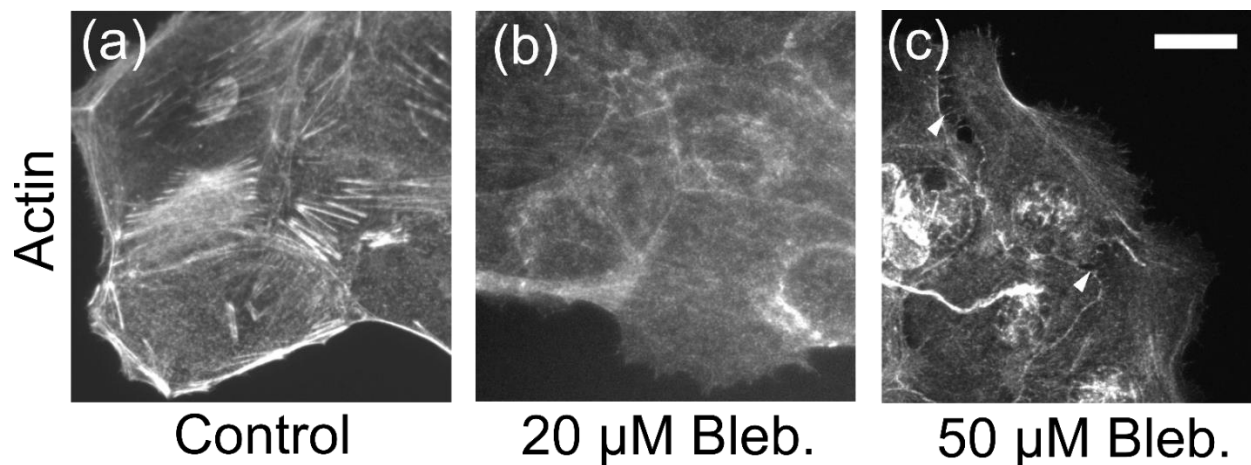
Figure S3. Immunofluorescence images of MDCK stained for actin (with phalloidin), either (a) untreated (control), (b) treated with 20 µM blebbistatin or (c) treated with 50 µM blebbistatin for 1 h. Notice the well-defined actin cytoskeleton in the control case, the decreased filamentous actin in the 20 µM blebbistatin treated case, and the ruptured cell-cell contacts in the 50 µM blebbistatin treated case (white arrow heads in (c)). Scale bar is 20 µm.

<center>CHAPTER 3</center>

STIFFNESS MEASUREMENT OF SOFT SILICONE SUBSTRATES FOR MECHANOBIOLOGY STUDIES USING A WIDEFIELD FLUORESCENCE MICROSCOPE

3.1 Introduction

Most type of cells in vivo inhabit in an extra cellular domain whose stiffness is in the range of kilopascal [51]. This is in contrast to cells grown in tissue culture dishes whose stiffness are several orders of magnitude higher. Experiments with cells on protein-conjugated ECM-soft substrates have shown that substrate stiffness influences cell migration as well as adhesion to the ECM beneath [52, 53]. In fact, substrate elastic properties is one factor controlling cell function [54] in a manner similar to pervasive biochemical signals. Protein-conjugated polyacrylamide gels are water-pervading hydrogels that have been widely used as cell culture substrates for mechanobiology studies [55]. Polydimethylsiloxane (PDMS) (Sylgard 184, Dow Corning) has been widely used as a biocompatible silicone gel with varied stiffness (in the range kPa to MPa) for micro engineering purposes [56]. Recently, soft silicone (eg. CY 52-276, Dow Corning)

substrates with more physiologically relevant stiffness in the range of a few kilopascals have been utilized as a biocompatible substrate for mechanobiology studies [57, 58].

A variety of approaches have been introduced for measuring substrate elastic properties including atomic force microscopy (AFM), macroscopic stretch-induced deformation of samples, micro rheology, sphere indentation, and micro-indentation with spherical tips [59]. Each of these methods has its own capabilities and weaknesses yet spherical indentation method (Figure 18) is a straightforward and fairly precise technique which only requires having access to a fluorescence microscope capable of wide-field imaging. Metallic spheres have been used to measure hydrogel stiffness in prior work [53, 60, 61]. Works which demonstrated the importance of substrate elasticity to cell migration used this technique to measure elastic properties of hydrogels [53]. Confocal microscopy techniques have also been recently employed to properly characterize substrate stiffness [60].

Here, we introduce a simple protocol for fabricating a soft silicone sample, embedding fluorescent beads (and ECM protein such as collagen I) on the top surface of the sample, capturing phase images of indenting sphere and fluorescence imaging of the top surface of the sample, and lastly, processing the captured images to measure the Young's modulus of the silicone sample. The prepared substrate can be directly used for TFM experiments. Use of stiff silicone such as PDMS as the base for soft silicone can also be used for mechanobiology studies involving substrate stretch which is discussed in chapter 5. Also, useful considerations imperative for preventing possible complications are pointed out where warranted.

3.2 Protocol for measuring stiffness

3.2.1 Preparation of the bead-coupled substrate

1. Pour 5 gr uncured PDMS (10:1 Base to Agent ratio) into a plastic dish and mix it for 2-3 minutes.

2. Cast the uncured PDMS mixture into a 60 mm petri dish.

3. Leave the Petri dish in vacuum chamber for 30 min in order to eliminate air bubbles.

4. Place the petri dish on a flat hot plate at $80 \,^{\circ}C$ for 4 hours.

5. Pour 2.77 gr (to be 1 mm thick) uncured soft silicone (CY52-276A/B) with A:B ratio of 1:1 into a plastic dish and mix it for 2-3 minutes.

6. Cast the uncured soft silicone mixture on the cured PDMS in the petridish.

7. Leave the petri dish in vacuum chamber for 10 minutes in order to eliminate air bubbles.

8. Place the petri dish on the flat hot plate at $70 \,^{\circ}C$ for 30 minutes.

9. Incubate the cured soft silicone with 70% ethanol for 5 min

10. UV expose the soft silicone for 5 min (10 cm from UV source) (Figure 18a).

11. Cut and remove the cured PDMS/soft silicone sample from the petri dish.

12. Incubate the soft PDMS with 1 mL of the mixture of EDC/NHS + beads + Col1 in DI water for 30 min by inverting the sample on the mixture as shown in figure 18b. Cover the sample with aluminum foil during incubation to avoid fluorescent beads being exposed to room light.

Note: The EDC/NHS + beads + Col1 mixture can be prepared while the soft silicone/PDMS sample is being exposed to UV. 1 mL of the mixture contains: 19mg of 1-ethyl-3-(3-dimethylaminopropyl) carbodiimide (EDC), 11mg *N*-hydroxysulfosuccinimide (sulfo-NHS), 30 µl of 0.44 µm carboxylate modified fluorescent (fluorescence color based on the filter cubes

available in the fluorescence microscope) microbeads, and 0.02 mg collagen I (from a rat tail, stock concentration of 4 mg/mL in 0.02 M acetic acid) to obtain a collagen concentration of about 0.02 mg/mL. The EDC/NHS/bead/collagen I mixture is briefly vortexed before coupling to the soft silicone sample.

13. Remove the sample and set it upright in a new petri dish so that the soft silicone is face up.

14. Wash the sample with proper amount of phosphate-buffered saline (PBS). After aspirating PBS, pour 5 mL of PBS on the sample.

15. Place and leave the sample in incubator overnight so that the soft silicone is further cured for about a day.

3.2.2 Measuring Young's modulus of the prepared substrate

1. Aspirate PBD, and add 4 mL DI water on the soft silicone sample.

2. Immerse and drop five 1 mm spherical indenters of proper density (look at table 1) on the soft silicone using pointed tweezers. There should be a gap of at least 5mm between the indenters.

3. Setup the sample petri dish on the stage of the wide-filed microscope.

4. Use a 10 X objective lens to focus on one of the indenters.

5 Take a phase image of the indenter. Use a tile scan if necessary.

6. Pan the live preview frame to the left so that indenter center is located at the right side of the frame and a region 1.5 R (indenter radius) away from the center is located at the left side of the frame. Switch from live phase imaging to the illumination for red fluorescence channel (if red fluorescence beads are coupled to the substrate).

7. Take a z-stack image sequence with a step size of 0.5 μm in a manner that plane z1 (Figure 18c) under the indenter center (on the right hand side of the frame) and the top plane z2 (on the left

hand side of the frame at least 1.5 R away from the indenter center) come into focus and go out of focus. Then save the z-stack image sequence.

8. Repeat step 4-7 for the other 4 indenters.

9. Open the phase of each indenter in ImageJ and measure their diameter by the line tool of the ImageJ (Figure 18e).

10. Open the z-stack fluorescent bead images in imageJ and by eye try to find, respectively, the frame numbers F1 and F2, where the beads under the indenter center (near the right edge of the frame) and beads near the left edge of the frame (top plane) are in the best focus. Figure 19a shows a frame where the fluorescent beads under the indenter center are in the best focus (near the edge of the frame).

11. At frame F1 draw a line across a micro-bead under the indenter center (Figure 19b).

12. Obtain the line scan intensity across the bead by ImageJ. Select different frames (in the neighborhood of the frame F1) to update the line scan intensity profile. The frame number F3, which gives the greatest maximum intensity is the frame best in focus under the indenter center (plane z1 in figure 18c).

13. Repeat steps 11-12 to obtain the frame F4 at which the beads are in focus 1.5 R away from the center (near the left edge of the frame).

14. The indentation depth ($\delta = z2-z1$) can be calculated as 0.5 (F4-F3).

15. Next, calculate the exerted force on the substrate by the indenter. To do this, subtract the buoyant force acting on the sphere from the liquid media (DI water) from the indenter weight to obtain the exerted force acting on the substrate (figure 1d). The exerted force on the substrate is therefore calculated as $F = (4/3) \, g \, \pi \, R^3 \, (\rho_{indentor} - \rho_{medium})$ where g is the acceleration due to gravity (9.807 m/s^2), $\rho_{indentor}$ is the indenter density, and ρ_{medium} is the density of the DI water.

16. The Young's modulus of the substrate can then be calculated as [62, 63]

$$E = c\frac{[3(1 - v^2)F]}{4R^{0.5}\delta^{1.5}}$$ (1)

where, here, v is the Poisson's ratio of the sof silicone substrate ($v \approx 0.5$ for incompressible materials [57]); and $c = \left[1 - \frac{2a}{\pi}\chi + \frac{4a^2}{\pi^2}\chi^2 - \frac{8}{\pi^3}\left(a^3 + \frac{4\pi^2}{15}b\right)\chi^3 + \frac{16a}{\pi^4}\left(a^3 + \frac{3\pi^2}{5}b\right)\chi^4\right]^{-1}$ is the correction factor considered for the Hertz model [62]. Here, $\chi = \frac{(R\delta)^{\frac{1}{2}}}{h}$; $a = -\frac{1.2876 - 1.4678v + 1.3442v^2}{1-v}$; and $b = \frac{0.6387 - 1.0277 + 1.5164v^2}{1-v}$. h is the thickness of the soft silicone substrate (figure 18c) that can be calculated by the amount of soft silicone which was cast into the petri dish before being cured (in this protocol the thickness of the sample was 1mm as mentioned). For large substrate thickness ($h > \sqrt{R\delta}$), c is close to 1. Parameters on the right-hand side of equation 1 should be expressed in SI units to obtain E in Pa.

Table 1 shows the elastic modulus of different soft substrates calculated using this protocol.
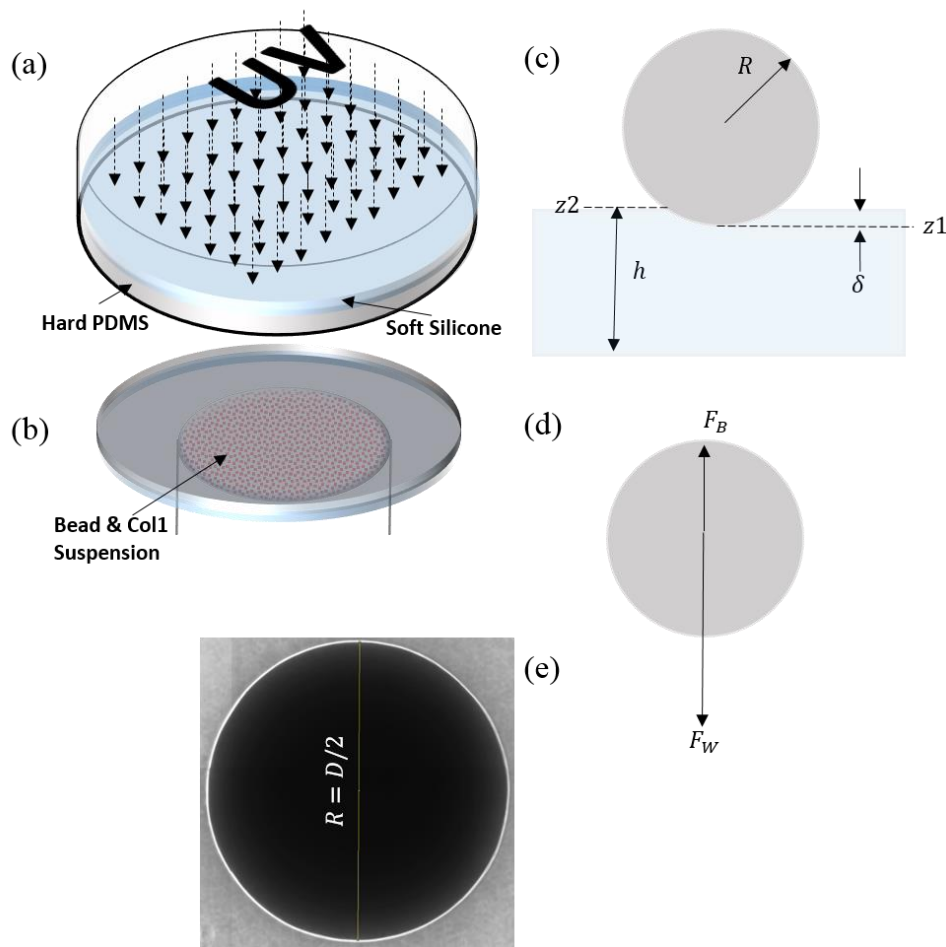
Figure 18. Substrate stiffness measurement by sphere indentation. (a) The prepared soft silicone substrate on hard PDMS base is exposed to deep UV light of wave lengths of 254 nm. (b) The sample is then inverted on EDC/NHS/fluorescent bead/collagen I mixture and incubated for 30 min. This allows the fluorescent beads to conjugate to the substrate top surface. The sample is further cured at 37°C overnight while kept incubated in PBS. The sample is placed in liquid media of known density (e.g. DI water) when ready for stiffness measurement. (c) Metallic spheres of radius R (0.5 mm here) are immersed into the liquid media and settled on the soft silicone surface. The deflection of the substrate (δ) is measured using a wide field fluorescent microscope. (d) The force acting on the substrate from the sphere is obtained by subtracting the buoyant force acting on the sphere from its weight (F_w-F_B). (e) The phase image of a sphere indenter. The radius of the sphere can be measured by drawing a line in ImageJ. The Young's modulus of the substrate can then be measured by using the modified Hertz model (equation 1).
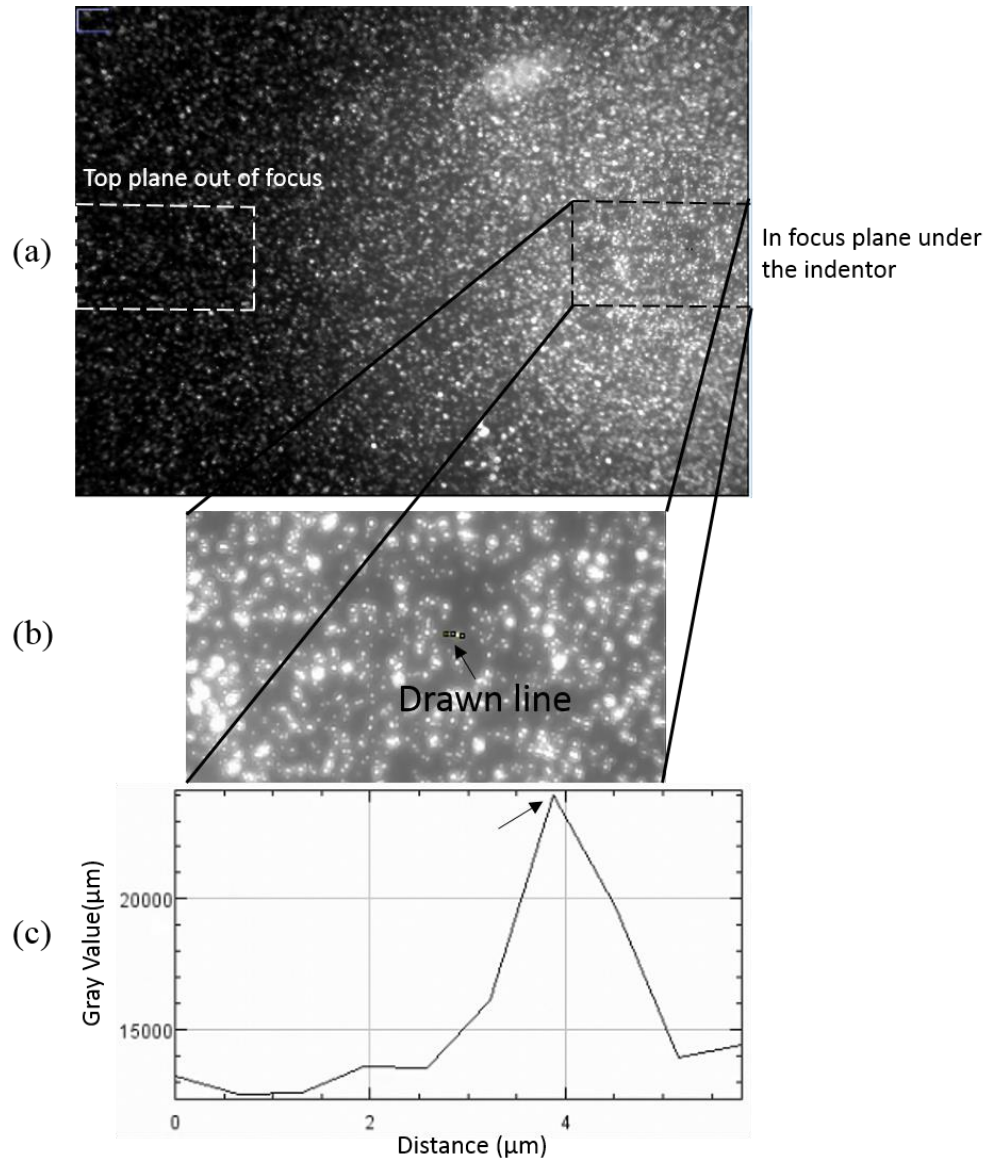
Figure 19. (a) The fluorescent bead image of the z-plane under the indenter center. The beads are in the best focus under the indenter center located near the right edge of the frame (black box). (b) A line is drawn across a fluorescent bead under the indenter center. (c) Line scan profile across the bead can be obtained by ImageJ at different planes. The shown profile gave the greatest value of maximum intensity (black arrow). The corresponding frame is chosen as the frame in which the beads under the indenter center are best in focus. By repeating this step for a region 1.5 R away from the indenter center (near the left edge of the frame), the best-in-focus top plane of the substrate is found. Substrate deflection can then be obtained by subtraction of the z values of the two planes.

Table 1. The Young's modulus of silicone substrates with different A:B ratios measured using the introduced protocol.

Material	Ratio	Indenter density (g/cc)	Young's Modulus in kPa (Avg±Std)
PAA Gel, E nominal = 20.7 kPa		4.66	22.1±4.2
CY 52-276 A/B	A:B 5:4	4.66	2.7 ± 2.1
CY 52-276 A/B	A:B 1:1	4.66	7.3 ± 1.9
CY 52-276 A/B	A:B 4:7	14.95	37.6 ± 3.9
CY 52-276 A/B	A:B 1:2	14.95	64.1 ± 6.9

CHAPTER 4

NON-INTRUSIVE MEASUREMENT OF WALL SHEAR STRESS IN FLOW CHANNELS

Highlights

- Fourier transform traction cytometry (FTTC) was used to extract wall coated with soft silicone.

- This approach introduces a non-intrusive direct method of shear stress measurement for flow channels.

- The method showed its applicability for a range of flow rates under Poiseuille flow regime in rectangular channels.

Abstract

Flow shear stress measurement plays an important role in the characterization of macro and micro fluidic systems. Many currently used wall shear sensors quantify local shear stress with the use of fluid-disruptive probes, unless installed accurately flush to the channel surface. Non-intrusive shear stress measurement systems capable of quantifying the shear stress vector field in larger areas are highly desirable. The present study reports on non-intrusive direct measurement of wall shear stress under pressure-driven fluid flows with the use of particle imaging velocimetry and

Fourier transform traction cytometry. This method uses the known mechanical properties of a soft substrate strained under the flow to quantify the shear stress field. Under fully developed pressure-driven laminar flows of different flow rates in a rectangular channel, the average magnitude of wall shear stress thus obtained matched with the theoretical results obtained for Poiseuille flow. The major advantage of this method is the direct experimental characterization of wall shear stress vector field without disruption of the flow itself. The method shows promise in the characterization of shear flow in diverse areas such as aerospace and bioengineering.

Keywords: Wall friction, PIV, Fourier transform, Traction force microscopy

4.1 Introduction

Characterization of frictional forces exerted by fluid flow on solid surfaces is of practical importance in macro and micro fluidics. Several techniques involving mechanical, thermal, optical, and chemical methods [64] have been used to quantify the wall shear stress field exerted by fluid flow. Methods such as hot film and hot wire anemometry [65], oil-film interferometry [66], use of liquid crystals [67, 68], electrochemical sensing [69], micro-electro-mechanical systems, (MEMS) [70, 71] and their new generation versions [72] such as densely arrayed direct sensing MEMS micro-sensors [73] with high spatial resolution measure local shear stress via flush-mounted floating sensors [74]. Therefore, accurate measurements require thickness of the floating element be small enough [74] and its gap under the element be less than a few viscous length scales [75] to reduce pressure-gradient induced errors [74]. These probes also need to measure intermediate parameters (eg. current and voltage) calibrated against shear stress [65]. As a non-intrusive approach, the present work demonstrates the measurement of wall shear stress (shear

stress field) with high spatial resolution in all-PDMS flow channels using the micron-scale displacement of a wall with specific mechanical properties.

In general, the high stiffness of solid surfaces that comprise the channel walls results in extremely low surface strain that is difficult to be observed under fluid shear stress. An analogous problem exists in the domain of bioengineering, wherein cell-generated stresses on solid surfaces are to be determined. For physiologically relevant cell substrate stiffness in the range of kPa, measurement of surface strain has enabled the determination of cell-generated traction stress. Several methods have been used to realize traction force microscopy (TFM) [76] which involves determination of traction stresses from the measured displacement of soft substrates. For example, the displacement of micropost force sensor arrays has been used to measure the traction force exerted by cells [77]. A similar method has been used to quantify the wall shear stress of driven fluids [78, 79]. While image processing is conventionally used for this purpose, MEMS technology can be used for quantification of the beam deformation [80]. An alternate approach is to use continuous substrates which are uniform and flat. For example, Gijsen et al. [81] used speckle pattern interferometry to measure deformation of a gel substrate to calculate the exerted flow shear stress by using Hooke's law.

Here, we use micro-particle imaging velocimetry (PIV) to obtain the displacement field in a soft substrate/wall and use regularized Fourier transform traction cytometry (FTTC) to determine the shear stresses from the flow-induced displacement. Considering the substrate as an incompressible elastic isotropic half space [7], traction forces can be obtained by solving $X = GF$ where the knowns X and G are, respectively, the displacement vector and the Green function of the substrate, and F is the exerted force vector. Butler et al. [8] introduced an efficient solution to this problem called Fourier transform traction cytometry (FTTC) wherein the forces are solved for in Fourier

space and then inverted back to real space. Regularization has also been shown to be necessary to obtain valid solutions for the stresses [7] and is therefore used in the FTTC implementation here. Soft linear isotropic elastic substrates such as polyacrylamide (PAA) gels and PDMS (Polydimethylsiloxane) elastomers of low stiffness (Young's modulus of 0.2-20 kPa) such as CY52-276 A/B [9, 10] are, in general, suitable substrates for this purpose. PDMS is a low cost and optically transparent silicone elastomer which can be easily bonded to other surfaces [82]. The method demonstrated here uses a soft silicone substrate (CY52-276 A/B, Dow Corning, Midland, MI, USA) and is thus especially useful when it is desirable that the flow channel be entirely made of silicone (for example, to meet chemical compatibility requirements), as is common in many applications in microfluidics.

The present paper uses micro-PIV techniques followed by FTTC to measure wall shear stress vectors exerted by fluid flowing through PDMS channels of rectangular cross section. While Mueller [83] introduced the approach and measured displacement of fluorescent beads embedded on much stiffer PDMS substrate (E = 500 kPa) under different flow rates, no shear stresses were reported. Here, a silicone elastomer of low Young's modulus in the range of 0.6 to 0.8 kPa is used to constitute the wall (substrate) such that shear stress of the order of 1 Pa in the fully developed region of a pressure- driven laminar flow through a PDMS channel of rectangular cross section can be determined. The results obtained in the mid width of the channel at several flow rates are validated by comparison to the theoretical wall shear stress expected for Poiseuille flow in a rectangular channel of the same geometry.

4.2. Materials and methods

Briefly, to make the flow channel, cured PDMS replica from a mold (constituting the top and side channel walls) is bonded to a soft silicone (e.g. CY52-276 A/B, Dow Corning, Midland, MI, USA) film as substrate (bottom wall). Marker fluorescent micro-beads embedded in the soft silicone top layer are used for measurement of the substrate displacement field. Microscopic image sequences of fluorescent beads embedded in the substrate are used for quantifying substrate displacement with the help of micro-PIV. Then, the Boussinesq Green function of the substrate is used to solve for the shear stress via FTTC [7, 8].

4.2.1 Channel fabrication

The elastic substrate of the channel was made of soft silicone CY52-276 A/B (Dow Corning, Midland, MI, USA). Briefly, a ~0.9 mm thick slab of CY52-276 A/B with a ratio of 1:1 was prepared on a clean glass slide. After 15 min of bubble removal in a vacuum chamber, the compound was cured at 50 °C on a hot plate for 10 min. The cured compound on the glass slide was then exposed to deep UV light (with the lamp 10 cm away) for 5 min (Figure 20a). Immediately after UV exposure, the top surface of the compound was seeded with carboxylate fluorescent beads (Invitrogen, Carlsbad, CA, USA) of 0.44 μm diameter. For this purpose, two glass supports were placed in a petri dish with a separation distance less than the length of the glass slide. Suspension containing 19 mg EDC (1-Ethyl-3-(3-dimethylaminopropyl)-carbodiimide) (Thermo fisher scientific, Waltham, MA, USA), 11 mg sulfo-NHS (N-Hydroxysulfosuccinimide) (Thermo fisher scientific, Waltham, MA, USA), 30 μL of 1% w/v fluorescent beads, and 1 mL DI water was injected in the gap. Then the glass slide with the soft silicone was inverted on the

suspension and incubated for 30 min in dark (Figure 20b). This method has the advantage that the fluorescent beads are only seeded on the top surface of the substrate. This avoids out of plane bead noise during micro-PIV cross-correlation. It should also be mentioned that the incubation of inverted soft silicone significantly prevents cluster formation of beads on the surface due to gravity.

To complete the fabrication process, a stiff PDMS (Sylgard 184, Dow Corning, Midland, MI, USA) replica of the rectangular channel (containing reservoirs) was bonded to the soft PDMS substrate. Briefly, uncured PDMS (Sylgard 184, Dow Corning, Midland, MI, USA) with base to curing agent ratio of 10:1 was poured on a master mold resembling the channel. After 30 min of bubble removal in a vacuum chamber, the PDMS covering the master was cured at 80 °C for 4 hours. After preparation of the open outlet reservoir by cutting a part of the PDMS replica resembling the outlet, the replica was bonded to the prepared soft PDMS (CY52-276 A/B) substrate (Figure 20c). Strong adhesion between stiff PDMS and CY52-276 A/B compound provided us with a water tight sealed channel at high flow rates with no need for plasma treatment often used in microfluidic channel fabrication. Finally, flow was injected to the inlet through a blunt needle inserted into the inlet and fixed with a bonded piece of PDMS (Figure 20d). The length, width and height of the fabricated channel were 40.7, 9.9 and 0.85 mm respectively. At the end of each experiment, substrate stiffness was measured by microscopy using the sphere indentation method [61] (described in section 3.2) using zirconium spherical indenters with a diameter of 1.1 ± 0.05 mm and specific gravity of 4.66.
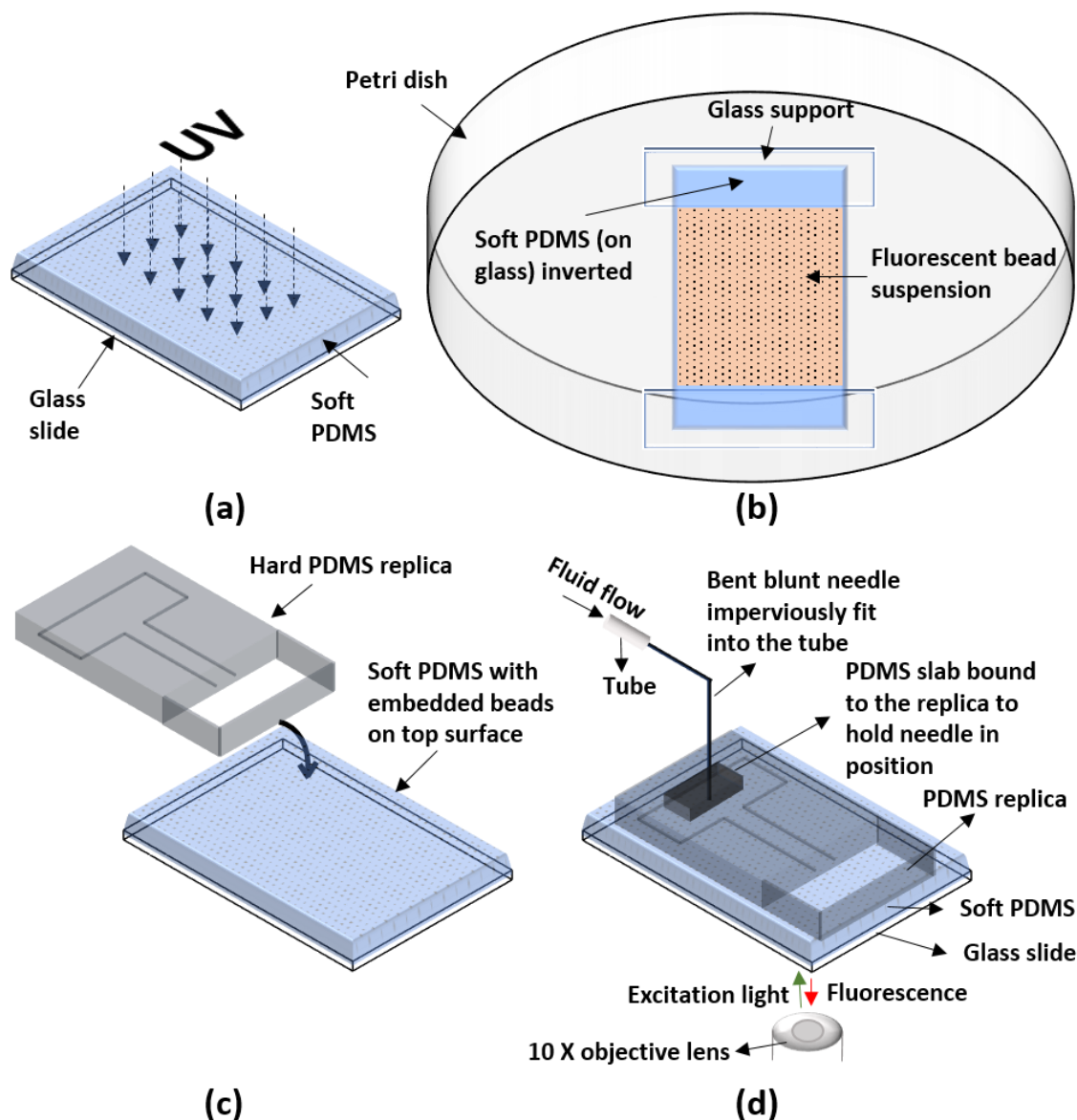
Figure 20. Fabrication of the all-PDMS flow channel. (a) Cured soft PDMS on a glass slide was first incubated with ethanol (for 5 min), air dried, and exposed to deep UV for 5 min. (b) Soft PDMS on glass slide was then inverted on fluorescent bead suspension and incubated for 30 min. (c) Hard PDMS replica cured on channel mold was placed on soft PDMS and created a water tight seal with no need for bonding treatment. (d) Inlet was supplied with pressure-driven flow through a bent blunt needle fixed to the inlet via a piece of PDMS. Prepared fluidic device was setup on the microscope stage for fluorescence microscopy.

4.2.2 Micro-PIV and FTTC

The prepared channel was first placed on the stage of a Leica DMi8 epifluorescence inverted microscope (Leica Microsystems, Buffalo Grove, IL, USA) equipped with a Clara cooled CCD camera (Andor Technology Ltd, Belfast, Ulster, UK) and a 10x objective lens. Pressure-driven DI water flows of fixed flow rates were provided by an infusion syringe pump (Harvard Apparatus, PHD 2000, Holliston, MA, USA). Fluorescent image sequences of the micro-beads seeded on the substrate were taken before and after application of the pressure-driven flow.

A MATLAB (R2017a, MathWorks, Natick, MA, USA) PIV program for cross-correlation [84] available at http://www.oceanwave.jp/softwares/mpiv/ was used to process image pairs of fluorescent beads on the substrate. The image pairs were those taken of the micro-beads while the fluid was stationary (reference image) and while the fluid flow reached steady state (target image). First, image preprocessing such as adjusting the brightness and contrast, defining the region of interest (ROI) and removing background noise by Imagej [85, 86] prepared the image sequences for velocimetry. The program then used 50% overlapped interrogation windows of 128×128 pixel^2 to quantify the displacement of beads between each pair of images resulting in a displacement vector field for each pair. The program was able to post-process the obtained vector fields, including interpolation of missing data, outlier removal, and data smoothing as necessary.

Assuming CY52-276 A/B cured compound layer to be an elastic isotropic half space with Poisson's ratio of $v \approx 0.5$ [9] and given its measured shear modulus of elasticity (as measured by the indentation of a sphere), an FTTC program using Boussinesq solution [7, 8, 87, 88] was used to solve the elasticity problem [8] as follows: For the Green function (G) and obtained displacement vectors ($\vec{X}$), shear stress vector ($\overrightarrow{\tau_w}$) field in the ROI was solved using equation (1):

$$\overrightarrow{\tau_w} = F_2^{-1}\{[F_2(G)]^{-1}F_2(\vec{X})\}, \tag{1}$$

where F_2 denotes two-dimensional Fourier transform. Figure 21 shows a side view of the geometry of the problem. The average of the quantified shear stresses at each flow rate was finally validated by comparison with theoretically obtained wall shear stresses exerted by the above pressure-driven flow.

4.3 Results and Discussion

Substrate shear stress measurements were conducted under pressure-driven laminar flows at several flow rates from 40 to 90 mL/min with corresponding Reynolds number (Re $= \frac{2\rho Q}{\mu(w+h)}$) ranging from ~140 to 310. The ROI window of 897 ×670 μm^2 (with its center set at mid width of the channel substrate, 36 and 4.7 mm away from the inlet and outlet respectively) for shear stress measurements was the position where the flow can be considered as hydrodynamically fully developed. Conventional theory predicted the entrance length ($L_e \sim 0.06 \times D_h Re$) at different flow rates to range from 13 to 29 mm. In fact, the entrance length correlation coefficient ($\frac{L_e}{D_h Re}$) in rectangular microchannels may be significantly lower than 0.06 [89].

4.3.1 Determination of displacement at the wall

First, the displacement field of the top of the substrate was obtained at several flow rates. Figure 22 shows unidirectional and nearly uniform displacement of the substrate in the flow direction. Figure 23 shows the average magnitude of the substrate displacement in the ROI at different flow rates. The error bars correspond to ± standard deviation of the experimental data. The data in all experiments showed a similar trend in average displacement. A limitation of the method is poor detection and vectorization of extremely small bead movements at flow rates lower than 40

mL/min (data not shown). One may be able to use soft substrates with lower stiffness or solve this issue by using smaller particles and image processing techniques with higher resolution.
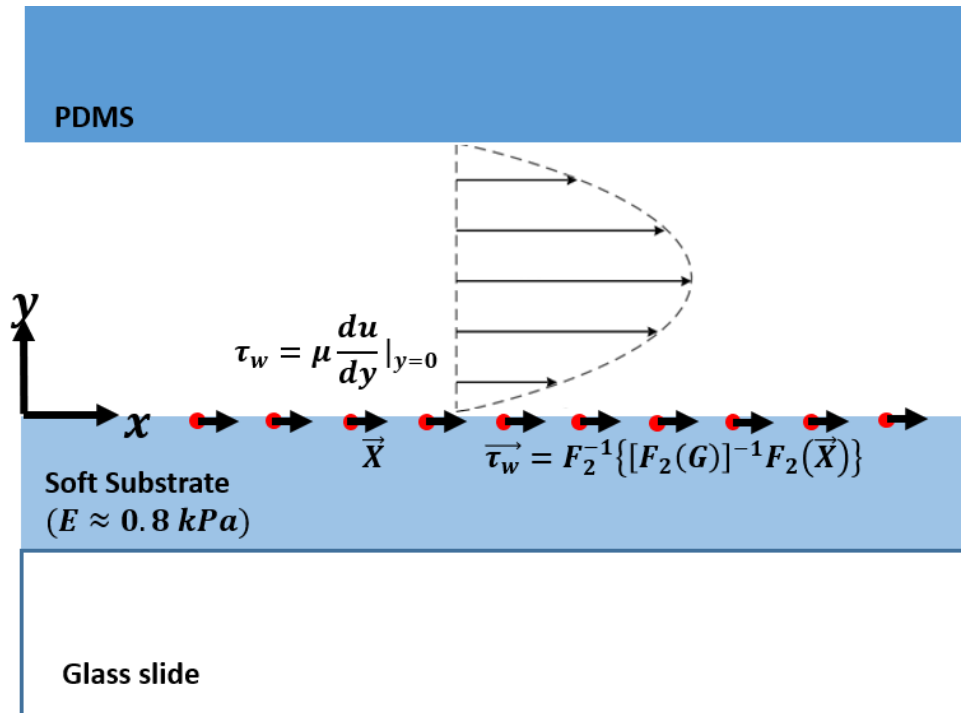
Figure 21. Schematic of side view of the PDMS rectangular channel. Displacement field of the soft substrate under frictional drag of Poiseuille flow is measured by PIV of marker fluorescent micro-beads embedded in the top layer of the soft substrate. Considering the Young's modulus (E ≈ 0.8 kPa) and Poisson's ration (v ≈ 0.5) of the displaced substrate (soft PDMS), shear stress field on the substrate can be quantified by FTTC and validated with theoretical wall shear stress expected for the viscous flow.

4.3.2 Determination of shear stress at the wall

In order to determine the shear stress from displacement, the elastic modulus of the substrate was first measured by sphere indentation [90, 91]. Briefly, a spherical zirconium indenter of known

density was placed on the elastic substrate. Using phase contrast imaging, the diameter of the indenter was found to be 1.1 ± 0.05 mm. Using widefield fluorescence imaging of the micro-beads in the substrate top layer, the deflection of the substrate under the indenter (indentation depth) was measured. Given the indentation depth and the film thickness of the substrate (~ 0.9 mm), a modified version of Hertz theory [92], Dimitriadis et al.'s model [62] was used to obtain the Young's modulus of the substrate. The Young's modulus of substrate prepared, following the indentation method, was found to be 0.8 ± 0.3 kPa (Figure 24).

Figure 25 shows the shear stress maps obtained by FTTC analysis of the substrate as an incompressible elastic isotropic half space. The shear stress vector field was unidirectional and nearly uniform, similar to that of displacement, except at low flow rates where the shear stress vectors have small components normal to the flow direction. Our results showed a nearly linear relationship between the substrate displacement and the exerted flow shear stress at all flow rates (data not shown). Figure 26 shows the average magnitude of shear stress vectors in the ROI versus the applied pressure-driven flow rates. Vertical error bars show the $\pm$ standard deviation of the experimental data. As the substrate is expected to show nearly linear elastic characteristics [9] under the applied shear force, a similar trend as that existing in the displacement fields is expected. Higher standard deviation (error bars) of the shear stress at different flow rates compared to that of the displacement field reflects two factors: the relatively high uncertainty in the measured stiffness and the higher non-uniformity in the determined shear stress vectors.
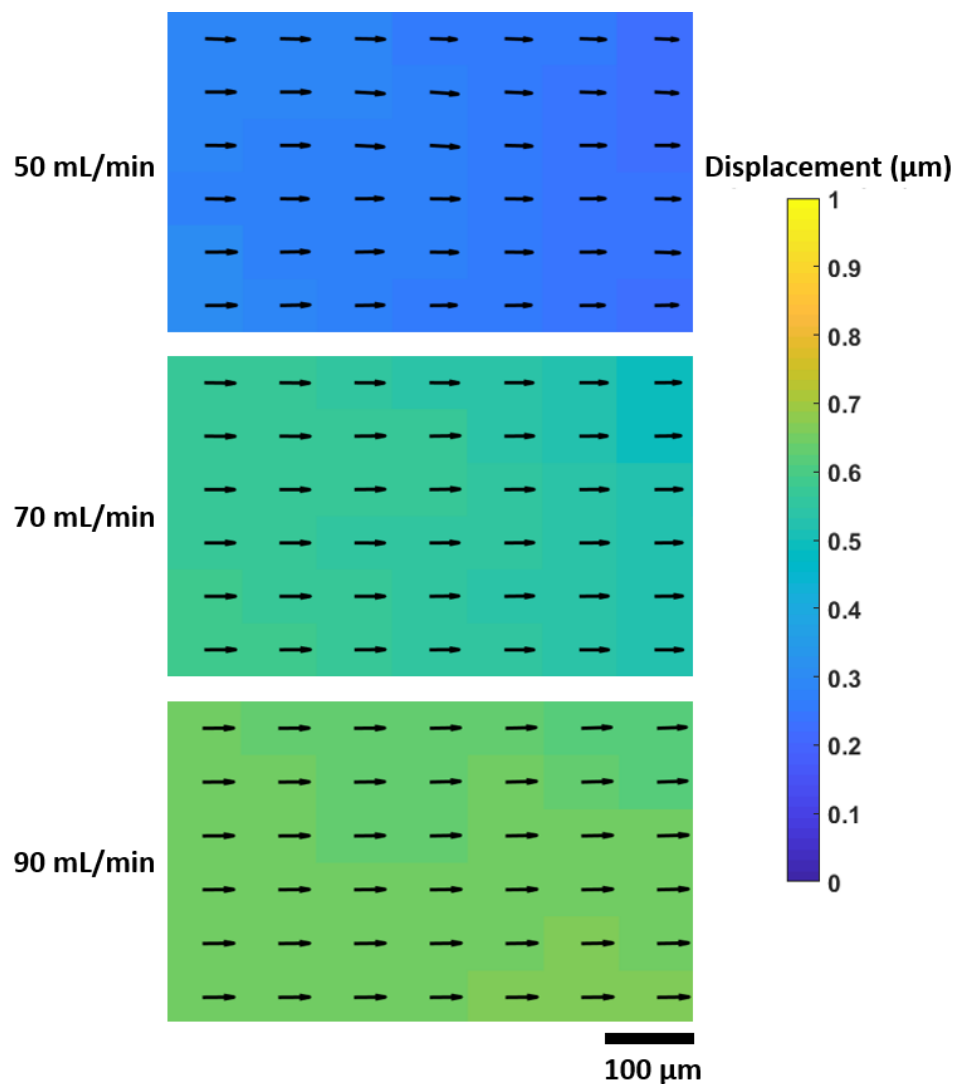
Figure 22. Substrate displacement field in the region of interest (ROI) at different flow rates. The displacement vector field of the substrate in a rectangular ROI in the mid width of the channel (under the centerline) was measured by particle imaging velocimetry of the fluorescent bead images. As expected, the uniform displacement in the fully developed region increases with flow rate.
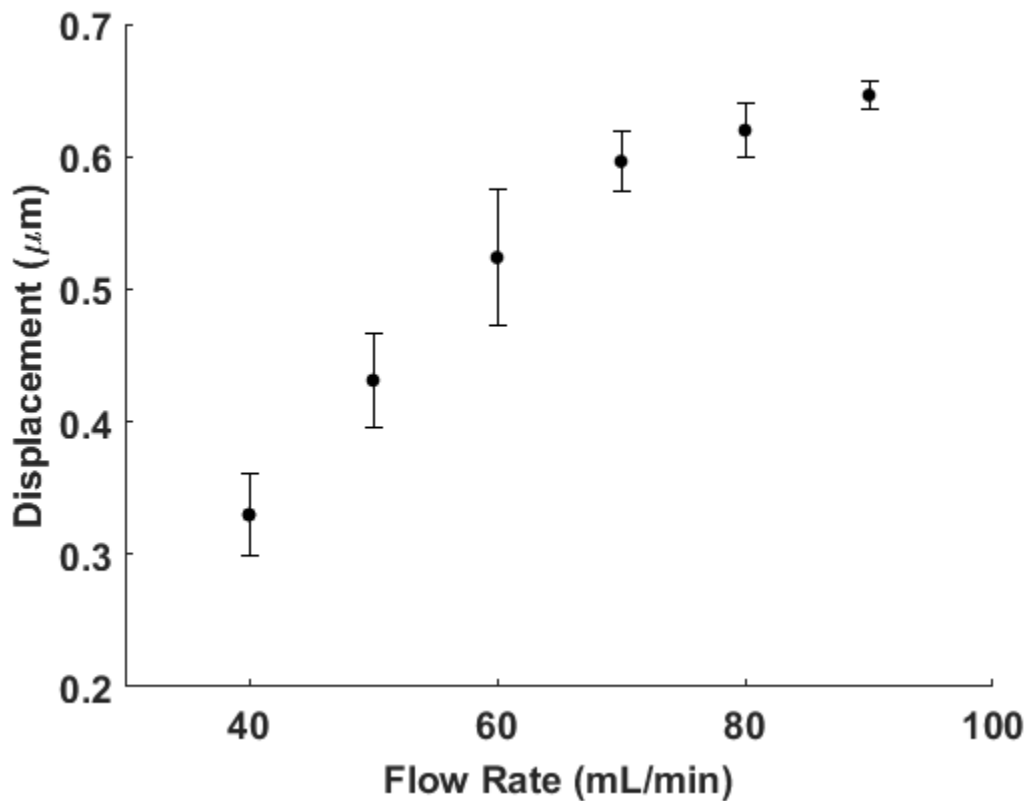
Figure 23. Average displacement at the top surface of the substrate increasing with fluid flow rate. The mean value of the average displacement in the rectangular ROI located in the mid width of the channels is expected to linearly increase with flow rate. Error bars show ± standard deviation of local displacements obtained from three experiments.

In the mid-width of the channel, the velocity profile of a fully developed laminar flow in rectangular channels was expected. Assuming no slip at the channel walls, this indicates a linear relationship between the applied flow rate (Q) and wall shear stress (τ_w). Eq. 2 shows this relation in the mid width of the channel derived from the fully developed velocity profile in rectangular micro-channels [93],

$$\tau_w = \mu \frac{du}{dy}\Big|_{y=0} = \frac{1.91\pi\mu Q}{wh^2(1-0.63\frac{h}{w})},$$ (2)

Where w and h are width and height of the channel. As shown in Figure 26, the expected theoretical line (relating the shear stress and flow rate) agrees with the measured experimental results. The average displacements and shear stresses obtained from different experiments in the same conditions showed similar trends.

It should be mentioned that in small length-scales complex molecular dynamics at the liquid and liquid-solid interface affects the quasi-static process of the channel flow [94]. Although, the channel height here is relatively high (0.85 mm) providing a surface-to-volume ratio in the order of 10^3 m^{-1}. This reduces the possibility of non-equilibrium flow conditions (considered for channels of micron length scales) which affects the validity of Navier-Stokes equations and the no-slip boundary condition at the channel walls [95]. Invalidity of these basic assumptions could also be seen in flows of liquid with non-Newtonian behavior [96] yet it is unknown the point at which stress-rate of strain relationship becomes non-linear in liquid flows [97]. With that said, the threshold of shear rate at which water shows non-Newtonian behavior is extraordinarily high [97] eliminating the possibility of non-Newtonian behavior of water in the present study.
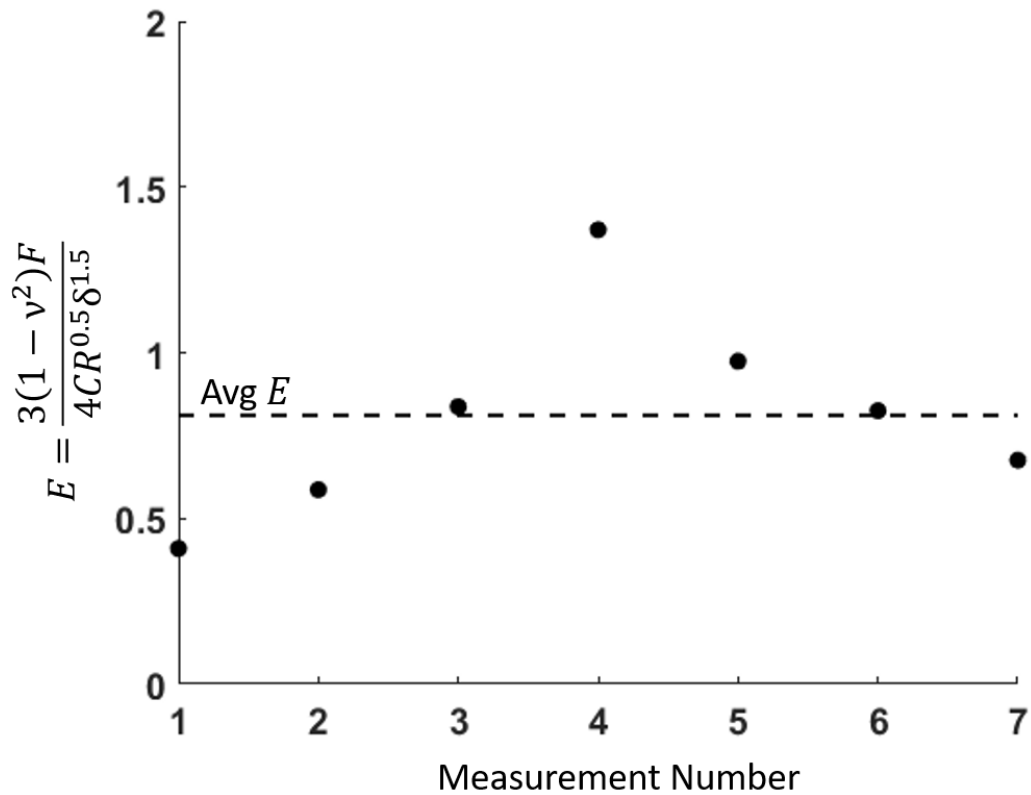
Figure 24. Stiffness measurement of the substrate with several indenters. ν and R are Poisson's ratio and radius of the indenter respectively. δ is indentation depth and F accounts for the indentation force. The average ± standard deviation of the substrate Young's modulus (E) was found to be 0.8 ± 0.3 kPa.
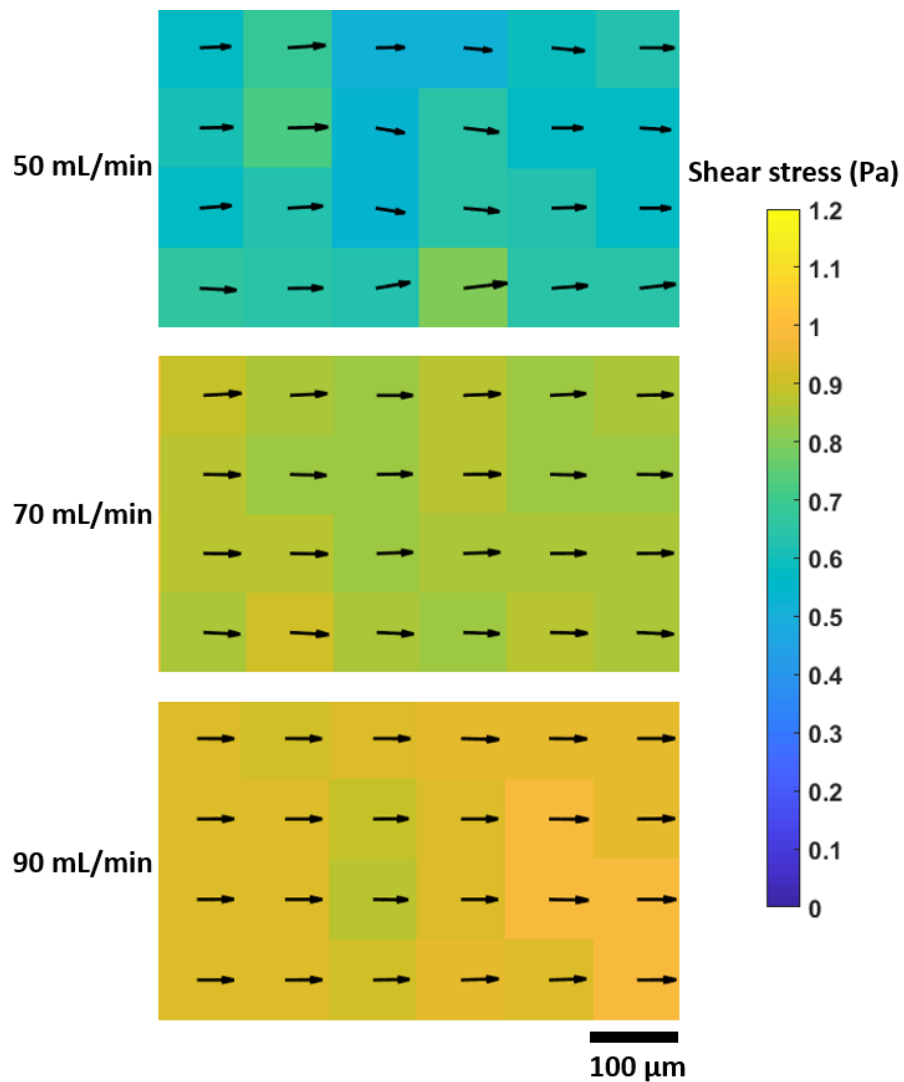
Figure 25. Shear stress vector field in the ROI shown as heat maps as a function of flow rate. The Scale bar for the heat map is shown on the right side and the scale bar for distance is shown below the heat map images.
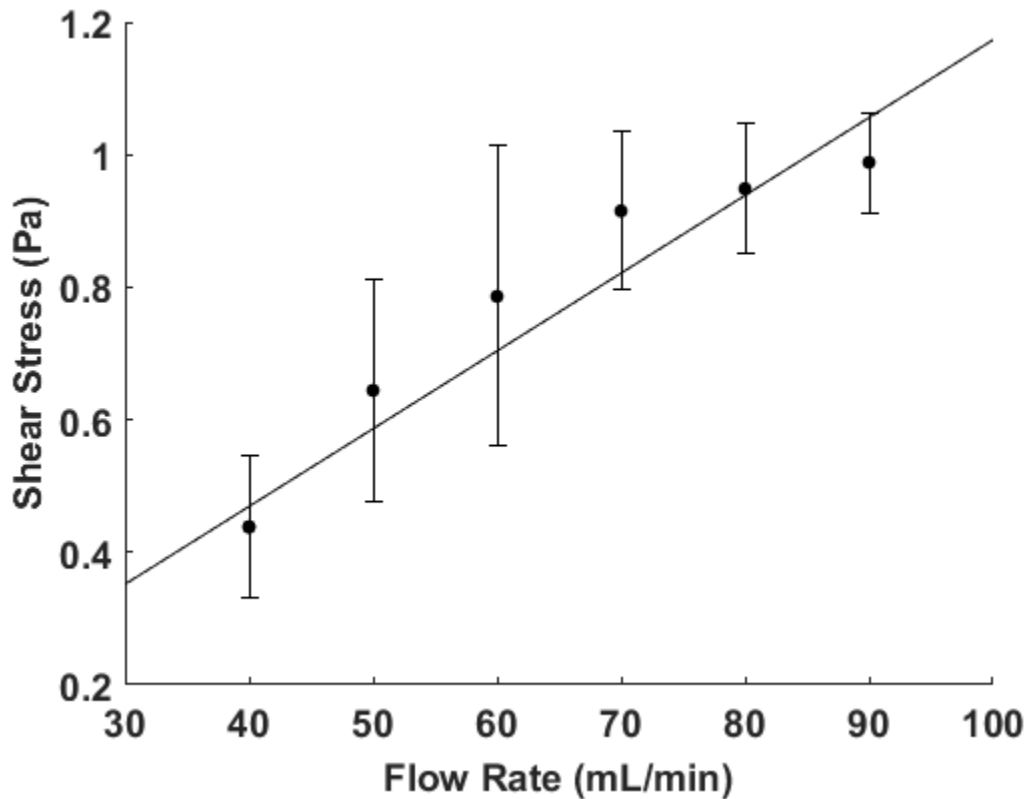
Figure 26. Determined average wall shear stress plotted as a function of flow rate. The mean value of shear stress in the rectangular ROI located in the mid width of the channels is expected to linearly increase with flow rate (line). Error bars show standard deviation of local shear stress magnitudes obtained in three experiments.

4.4 Conclusions

A non-intrusive method for determining the wall shear stress in flow channels was presented. Wall shear stress field of the order of 1 Pa exerted by Poiseuille flow through a rectangular channel of dimensions of a few mm was measured using FTTC. The only experimental modification of the flow channel required is the coating of a wall with soft silicone with doped fluorescent microbeads. In microfluidic applications where PDMS flow channels are widely used, this method can be

seamlessly integrated to yield wall shear stress values at varying flow conditions. Micro-PIV was used to quantify the wall displacement field by image processing of fluorescent beads embedded at the top surface of the wall. Sphere indentation method was used to measure the wall stiffness (<1 kPa) and the wall shear stress field was determined from the displacement field of the wall by regularized FTTC. The results obtained in the fully developed region of the channel at different flow rates ranging from 40 to 90 mL/min agree with theoretical wall shear stress of the Poiseuille flow. The minimum flow rate over which substrate displacement was measurable was limited by the resolution of micro-PIV. The method presented here is a versatile and non-disruptive means of quantifying shear stress vectors with high spatial resolution. By lowering the substrate stiffness and using high resolution image processing techniques one may characterize the shear stress over a wide range of flow rates.

Acknowledgments

CHAPTER 5

MECHANICAL RESPONSE OF AN EPITHELIAL ISLAND SUBJECT TO UNIAXIAL STRETCH ON A HYBRID SILICONE SUBSTRATE

Abstract

The mechanical response of large multi-cellular collectives to external stretch has remained largely unexplored, despite its relevance to normal function and to external challenges faced by some tissues. Here, we introduced a novel yet simple hybrid substrate made of a layer each of hard and soft silicone to enable external stretch while providing a more physiologically relevant physical micro-environment for cells. We micropatterned epithelial islands on the substrate using a stainless steel stencil to allow for a roughly circular island shape while not restraining the cells at the edges. While the strain energy stored in the substrate for unstretched cell islands expectedly stayed constant over time, we found that a uniaxial 10% stretch resulted in an abrupt increase, followed by sustained increase in the strain energy of the islands over tens of minutes, indicating slower dynamics than for single cells reported previously. At the same time, the sheet tension at the mid-line within the island, perpendicular to the stretch direction, also more than doubled compared to unstretched islands. Interestingly, the sheet tension at the island mid-line parallel to the stretch

direction also reached similar levels over tens of minutes indicating the tendency of the island to homogenize its internal stress. We suggest that the hybrid silicone substrate provides for an accessible substrate for studying the mechanobiology of large epithelial cell islands and other cell collectives.

Keywords: mechanobiology, strain, traction force, sheet tension, micropatterning

5.1 Introduction

External mechanical stimuli are known to regulate physiological processes controlling tissue development, maintenance and disease [98-100]. Mechanotransduction of signals due to substrate/ECM stretch via focal adhesions and ion channels regulates growth, migration, proliferation and differentiation in different cell types [101-105]. Particular cell responses to stretch depend on both stretch direction and frequency. For instance, adherent cells specifically reorient perpendicular to stretch direction for uniaxial cyclic strain [106]. The response of cells to stretch also depends on the extent of cell-cell interactions, with rheological properties evolving over time for stretched monolayers [107].

A primary aspect of the mechanical response of cells is the change in the traction force exerted by the cells on the substrate upon stretch. Traction force exertion in human airway smooth muscle cells was impaired right after stretch-unstretch maneuvers [108]. Traction forces exerted by uniaxially stretched human alveolar single epithelial cells was greater than the baseline but it significantly weakened to a level lower than the baseline upon release [109]. Human umbilical vein endothelial cells also displayed traction forces that increased by 5-20% upon uniaxial stretch [110]. Under equibiaxial sustained stretch, an acute cell stiffening and enhancement of traction

force was observed in smooth muscle cells before their gradual reduction [111]. The traction force and endogenous sheet tension of epithelial islands (of 80 µm diameter) increased upon application of equibiaxial stretch and returned to near baseline levels over a time scale of <10 min [112]. However, the mechanical response of larger epithelial clusters adherent to substrates have remained largely unexplored.

Prior experimental systems to apply stretch and simultaneously measure cell-exerted traction forces have involved either polydimethylsiloxane (PDMS)-based discontinuous silicone pillar/micro-structured substrates [111, 113] or continuous substrates that consist of soft substrates like PAA gel coupled to hard PDMS using chemical treatment [114]. For stretch maneuvers implemented with hydrogels such as polyacrylamide (PAA) gel or matrigel, matrix hydraulics can be a factor that needs to be considered [108, 112]. Thus, it is desirable to use a continuous substrate that is not a hydrogel, and therefore does not involve additional hydraulic effects, in cell stretch maneuvers.

Here, we show that elastic soft silicone substrates bound to hard PDMS are suitable for simultaneous stretch and traction force microscopy. We pattern large epithelial cell islands hundreds of µm in diameter, apply 10% uniaxial stretch and track temporal changes in the traction forces exerted by these islands. We find that traction forces exerted by these islands quickly increase initially, but then continue to increase slowly over tens of min, compared to that for single cells/smaller islands reported previously. We also find that the cell sheet tension in the island also increase several-fold both in the stretch direction and in a direction perpendicular to it. The results highlight the ability of epithelial cell islands to both homogenize and bear stress within the island.

5.2 Methods

5.2.1 Cell culture

MDCK II cells (generously provided by Daniel Conway, Virginia Commonwealth University) were cultured in DMEM (Dulbecco's modified Eagle's medium, Corning, Corning, NY) supplemented with L-Glutamine, sodium pyruvate, 1% Penicillin/Streptomycin, and 10% Fetal Bovine Serum (FBS) (Corning) at 37°C and under 5% CO_2.

5.2.2 Preparation of hybrid silicone substrates

In a 60 mm petri dish, 0.85 g CY52-276 A/B (Dow Corning, Midland, MI, USA) with an A:B ratio of 1:1 was cast on a cured piece of hard PDMS (Sylgard184 Silicone Elastomer kit, Dow Corning Corp., Freeland, MI, USA) with pre-polymer to curing agent weight ratio of 10:1 for the hard PDMS. After 10 min of degassing, the soft silicone was cured on a hot plate at 70 °C for 30 min. The cured soft silicone was exposed to deep UV light for 5 min and the top surface was seeded with carboxylate fluorescent beads (Invitrogen, Carlsbad, CA, USA) of 0.44 μm diameter as follows. The sample was inverted [112] on a suspension containing 19 mg EDC (1-Ethyl-3-(3-dimethylaminopropyl)-carbodiimide) (Thermo fisher scientific, Waltham, MA, USA), 11 mg sulfo-NHS (N-Hydroxysulfosuccinimide) (Thermo fisher scientific, Waltham, MA, USA), and 30 μL of 1% w/v fluorescent beads in 1 mL DI water for 30 min [115, 116]. Then, a slab of 45×35 mm^2 PDMS/soft silicone was cut and washed with PBS before it was used for micropatterning.

5.2.3 Micropatterning of large epithelial cell islands

12 mm thick 316 stainless steel sheets with laser-drilled 380 μm diameter holes (California Lasers, Simi Valley, CA, USA) were used as biocompatible stencils to topographically confine the plated epithelial cells. Briefly, a few drops of DMEM were placed on the soft silicone sample before the perforated sheet was placed on the substrate. This step is critical as it avoids air entrapment in the sheet holes. Media with cells was then plated on top of the perforated sheet so that the cells settled on the substrate beneath the holes. After overnight incubation at 37 ºC, 5% CO_2, micropatterned islands with the same size as that of the sheet holes were obtained.

5.2.4 Substrate stretch

A custom designed uniaxial stretcher was used to uniaxially stretch micropatterned epithelial monolayers. Similar to previously designed uniaxial stretchers [117, 118], media for the micropatterned cells was confined within a PDMS well placed on the substrate that was mounted on the stretcher. Here, CY52276 A/B (i.e. soft silicone) was used as a mechanically characterized silicone substrate [9, 10] which can be coated with different proteins to enhance cell attachment [119, 120].

5.2.5 Image acquisition

Phase and fluorescence images of the cell islands were acquired with a Leica DMi8 epifluorescence inverted microscope (Leica Microsystems, Buffalo Grove, IL, USA) equipped

with a Clara cooled CCD camera (Andor Technology Ltd, Belfast, Ulster, UK), a 10x 0.3 NA

objective lens, and an airstream incubator (Nevtek, Williamsville, VA, USA).

5.2.6 Substrate strain field

PIV was used to characterize the strain field of the substrate when stretched by 10% along the y

direction. Captured substrate bead images before and after stretch were first preprocessed (e.g.

adjustment of brightness/contrast) in ImageJ [86, 121]. Then a direct cross-correlation PIV

algorithm (PIVlab [33], Version 1.42) in MATLAB (R2017a, MathWorks, Natick, MA, USA)

with 256×256 pix^2 interrogation windows and 50% overlap yielded the displacement field (u, v)

of the stretched substrate. After the application of post-processing (i.e. standard deviation filtering,

local median filtering, data smoothing and removal of displacement at frame corners as outliers),

the strain field of the substrate was computed as:

$$\varepsilon_{yy} = \frac{dv}{dy}, \varepsilon_{xx} = \frac{du}{dx}, \varepsilon_{xy} = \frac{1}{2}\left(\frac{du}{dy} + \frac{dv}{dx}\right) \tag{1}$$

5.2.7 Traction force microscopy

For control (unstretched) and stretched islands, red fluorescence bead images were taken over time

as well as after the removal of the islands using 10% sodium dodecyl sulfate. PIVlab [33] (Version

1.42) was used to process image pairs (bead image of a time point and reference bead image).

PIVlab was then used with the fast Fourier transform window deformation method with 50%

overlapped interrogation windows of 64×64 and 32×32 pixel^2 to quantify the displacement of the beads resulting in a displacement vector field at each time point. The Young's modulus of the substrate (cured CY52-276 A/B) was previously measured to be 7.2 ± 2.4 kPa [116] using sphere indentation. By considering the substrate to be an elastic isotropic half space with Young's modulus of 7.2 kPa and Poisson's ratio of 0.5, Fourier transform traction cytometry [7, 8, 88, 122] was used to compute the traction stress field using MATLAB.

Two-sample 2 tale student t-test was used to test the statistical significance of the effects of substrate stretch. Paired-sample 2 tale student t-test was used to test the statistical significance of temporal changes of associated variables. Significant effects are expressed as * ($p<0.05$), ** ($p<0.01$), and *** ($p<0.001$).

5.3 Results

Compared to soft substrates such as PAA gels coupled to hard PDMS used previously [112, 114], which require chemical treatments to bond the soft and hard substrates, we found that soft silicone bonded as it cured on hard PDMS without any need for chemical treatments. This substrate also avoids issues due to hydraulics observed previously with PAA bonded to PDMS [112]. We also devised a method to couple fluorescent micro-beads just to the top surface of the soft silicone as depicted in Figure 27A,B, drawing on previously published methods [123]. Using a custom built uniaxial stretcher (Figure 28A), we assessed the strain field in the substrate, as it was stretched by 10%. As shown in Figure 28B, the strain along the stretch direction was 10%, with a strain magnitude about half that in the normal direction, as expected. The shear strain magnitude was more than an order of magnitude lesser.
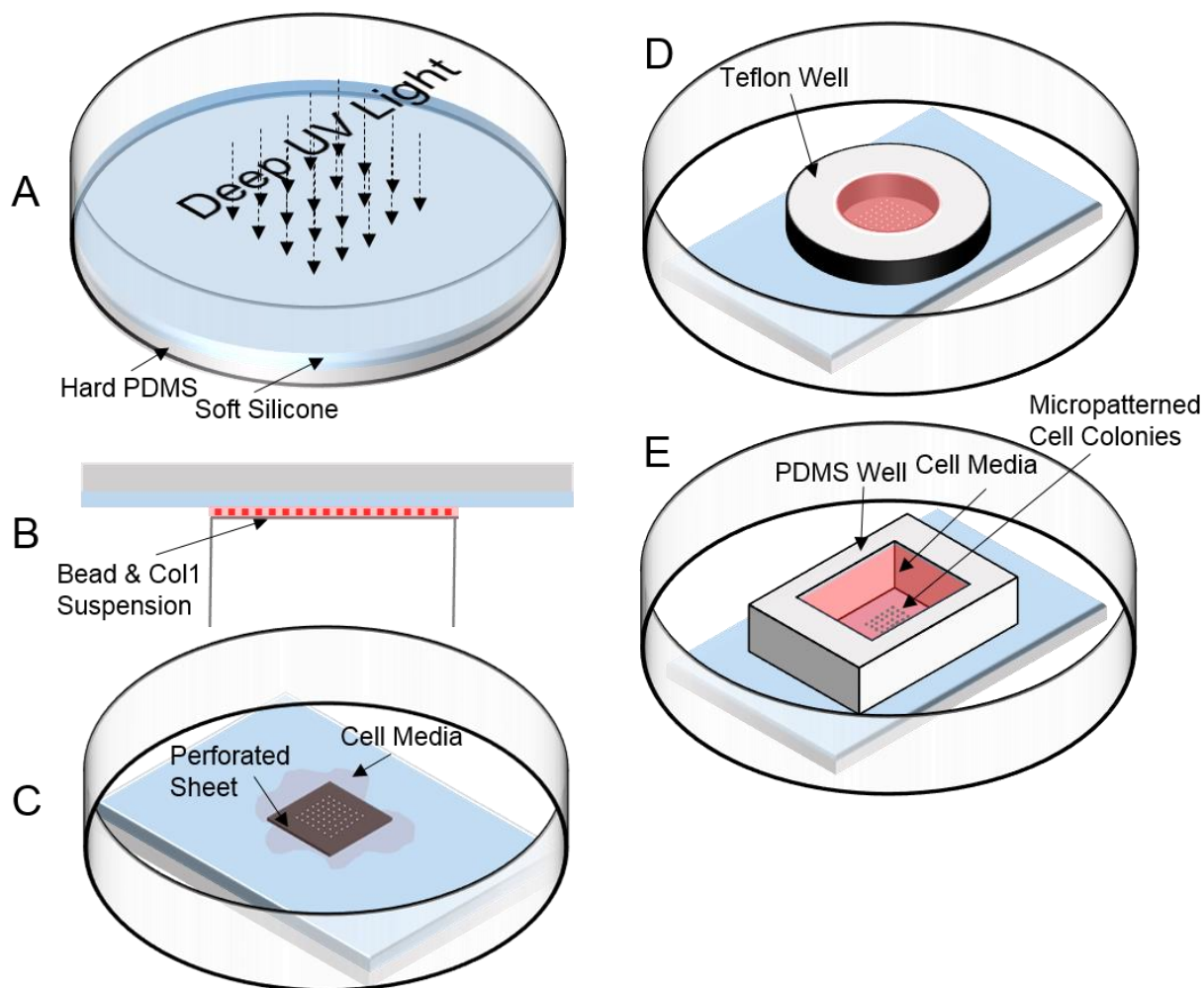
Figure 27. Preparation of hybrid silicone substrates and patterning of epithelial cell islands for stretch and traction measurements. Soft silicone was cured on a layer of pre-cured hard PDMS, and then exposed to deep UV light (of wave lengths 185 and 254 nm) (A). It was then incubated with an aqueous mixture containing EDC, sulfo-NHS, fluorescent beads, and collagen I in water (B). After washing with PBS, some cell culture media was added and a perforated stainless steel sheet was placed on the soft silicone sample (C). Cells were then plated in media constrained by a teflon well (D). After overnight incubation at 37^0 C (and 5% CO_2), the Teflon well and perforated sheet were removed and a PDMS well held replaced cell media supplemented with 10 mM HEPES (E).
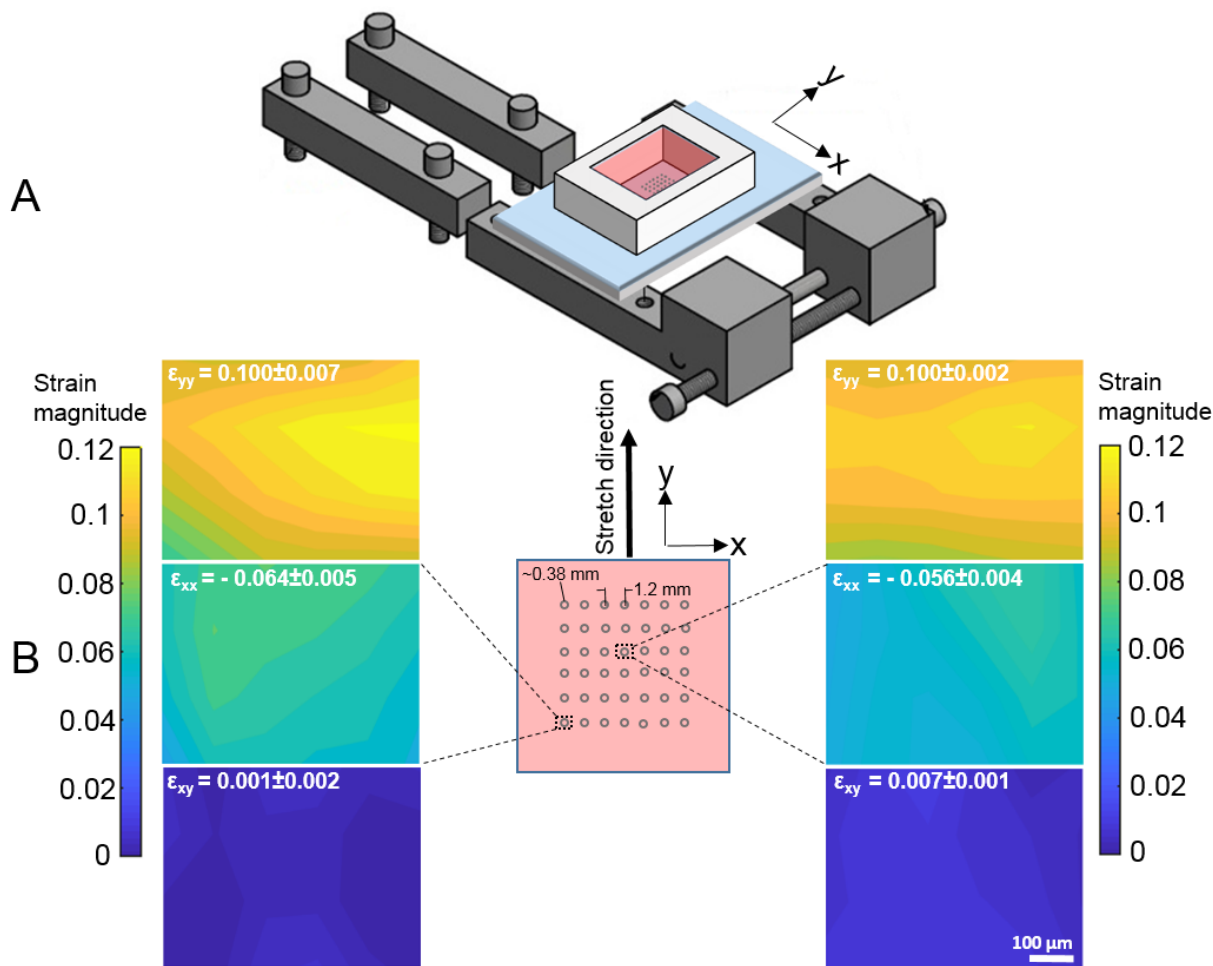
Figure 28. Application of uniaxial stretch. (A) Schematic of the custom designed uniaxial stretcher. (B) The region of the sample (where the islands are patterned, shown as circles) is schematically shown (middle), with y being the stretch direction. Strain field (ε_{yy}, ε_{xx}, ε_{xy}) of the substrate at the center (right images) and corner (left images) of the sample under 10% uniaxial stretch are shown.

We wanted to utilize this hybrid silicone substrate to assess how large epithelial cell islands mechanically responded to external stretch. We patterned large epithelial cell islands (Figure 27C-E) with a diameter of ~380 μm and with about six times as many cells as considered previously in

80 µm islands [112]. Figure 29A shows a map of traction stress exerted by an unstretched MDCK island. To characterize the mechanical output of the island, we quantified the strain energy stored in the substrate due to the work performed by the cell island [8], computed as

$$W_A = \frac{1}{2}\int \vec{T}(r).\vec{u}(r)\, dA \qquad\qquad (2)$$

where $\vec{u}(r)$ and $\vec{T}(r)$ are the displacement vector and the exerted traction stress vector applied by the cell island at a location of the substrate top surface, respectively.
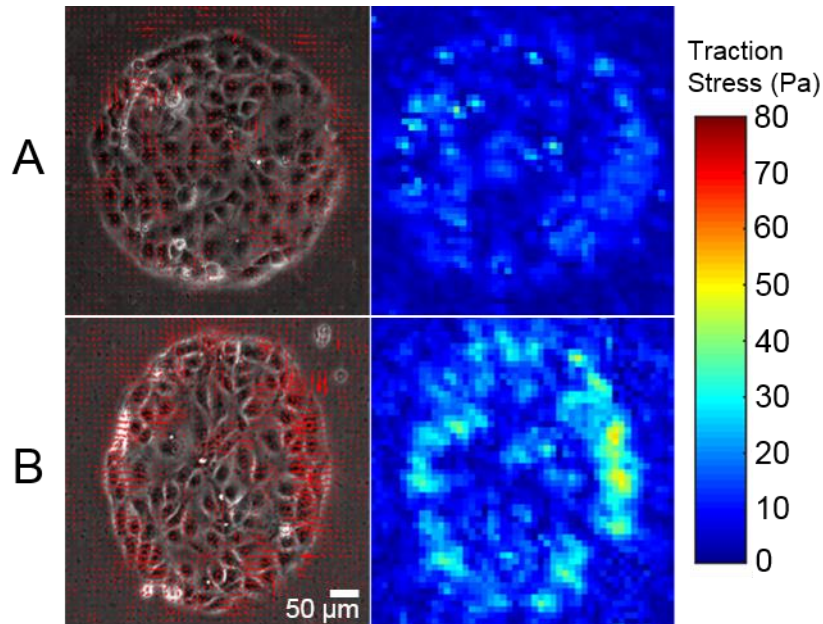
Figure 29. Traction forces exerted by control and uniaxially stretched MDCK islands. (A-B) Traction stress vector field (left) and traction stress magnitude (right) of a micropatterned MDCK cell island that hasn't been subjected to stretch (A) and that has been subjected to 10% uniaxial stretch (B) for 35-40 min.
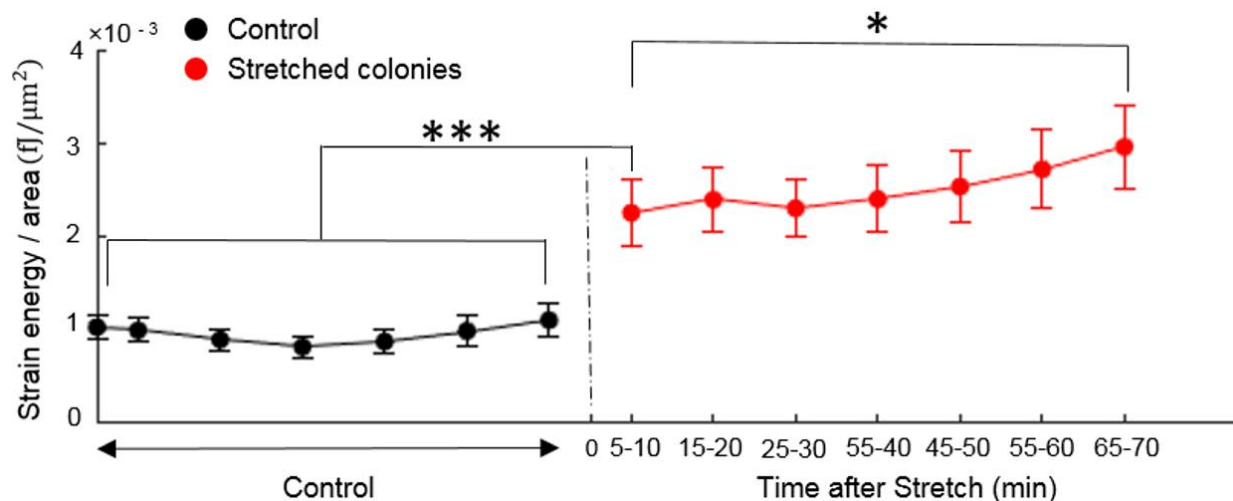
Figure 30. Temporal changes in strain energy stored in the substrate for control (black) and stretched (red) cell islands. Strain energy per unit area of the control cell islands (N = 14 islands) stays essentially constant. Stretched islands (N = 17 islands) exhibit greater strain energy which continues to slowly increase over time after the initial abrupt increase. Error bars show the corresponding values of standard error of the mean for all islands.

Figure 29B shows the traction map for an MDCK island uniaxially stretched by 10%. Notice the apparent larger aspect ratio of the stretched island. As is evident in Figure 29B, the overall levels of traction stress exerted are higher in stretched islands. Accordingly, compared to the unstretched islands, the stretched islands displayed higher strain energy (Figure 30). The strain energy density of stretched islands were significantly higher than unstretched islands even 5-10 minutes post-stretch ($p<0.001$). However, the strain energy density after over an hour post-stretch was slightly even higher ($p<0.05$) suggesting that the island mechanical response continues to evolve slowly.
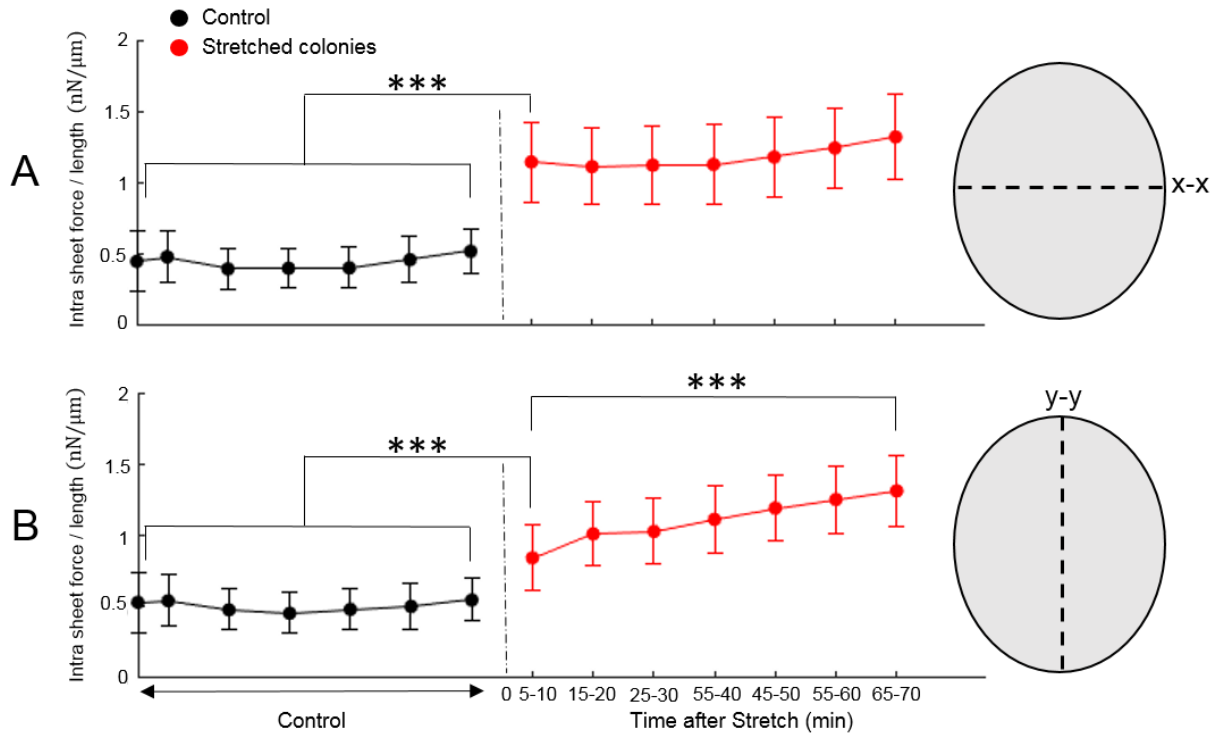
Figure 31. The sheet tension of the midline of control (black) (N = 14 islands) and stretched (red) (N = 17 islands) cell islands. Cell sheet tension at the midline of cell islands along the x-x (A) and y-y (B) midlines are shown. Error bars show the corresponding values of standard error of the mean for all islands.

In order to obtain a measure of forces transmitted through the cell island and from cell to cell, we then proceeded to quantify the sheet tension within the island at the midline within the island [124] as follows: the net force exerted by the two halves of an island at the midline is given by

$$\vec{F}_i = \sum \vec{T}_{ij} \qquad i = 1, 2 \tag{3}$$

where $\sum \overrightarrow{T_{ij}}$ is the vector sum of the traction forces over position *j* for each half *i* (*i*=1,2).

The average of these forces is the estimate for the net force at the island midline and the cell sheet tension per unit length is given by

$$\overrightarrow{F_L} = \frac{(\overrightarrow{F_1} - \overrightarrow{F_2})}{2L} \tag{4}$$

where *L* is the length of the island mid-line (i.e., the diameter of the island). Compared to unstretched islands, the cell sheet tension for stretched cells at the midline (x-x) perpendicular to the stretch direction (y) was significantly higher (p<0.001) even 5-10 min post-stretch. Interestingly, the cell sheet tension at the midline (y-y) parallel to the stretch direction (y) was also significantly higher (p<0.001) (Figure 31). While the cell sheet tension for stretched cells at the midline perpendicular to the stretch direction didn't change over tens of minutes, sheet tension at the midline parallel to the stretch direction was even higher over an hour post-stretch compared to just 5-10 min post-stretch (p<0.001), indicating a slow increase.

5.4 Discussion and Conclusion

We introduced a hybrid silicone substrate that can be fabricated relatively easily and avoids some of the steps (like chemical treatment for bonding) and complications (like hydraulic effects) of hydrogel-PDMS hybrid substrates [112, 114]. Using stencil-based micro-patterning, we patterned large epithelial cell islands and uncovered aspects of their mechanical response to external stretch.

We found that the strain energy stored in the substrate for stretched islands even at 5-10 min post-stretch was higher than that for unstretched islands. However, there was also a slow evolution of the strain energy over tens of minutes, in contrast to that for single cells [111] and small islands [112] that exhibited smaller time scales for alterations in exerted traction. Our data shows that this slower evolution is related to the slower increase in the cell sheet tension acting at the midline (y-y) parallel to the stretch direction (y), as it co-evolved with the strain energy over tens of minutes. In contrast, the cell sheet tension acting on the midline (x-x) perpendicular to the stretch direction (y) maintained its magnitude over tens of minutes after the initial increase.

Our data indicates that epithelial islands under uniaxial stretch tend to homogenize their cell sheet tension in orthogonal directions over time, and that the time constants for these changes depend on the direction. The data also indicates that the cell sheet can sustain much higher increases in sheet tension (compared to baseline levels) without rupturing cell-cell contacts. This may reflect the inherent strength of the cell-cell contacts or rapid changes that help adapt the contacts to external challenges. Immunostaining of the islands did not show any significant alteration in the extent of actin or E-cadherin localization when unstretched islands were compared to stretched islands. However, we cannot strictly rule out subtle changes as there was large heterogeneity in actin and cadherin levels (at the cell-cell contacts) between islands. Future studies over longer time periods can reveal further changes that may occur in response to external stretch.

In vitro methods to exert external stretch on large cell collectives are essential to understand how multi-cellular collectives dynamically adapt and modify their behavior in response to external challenges. Understanding the response to a step increase in stretch can in turn help decipher responses to more complex stretch maneuvers. We propose that the hybrid substrates used here

may enable enhanced studies of cell response to stretch as it facilitates both optical observations and force measurements.

Acknowledgments

5.5 Supporting information
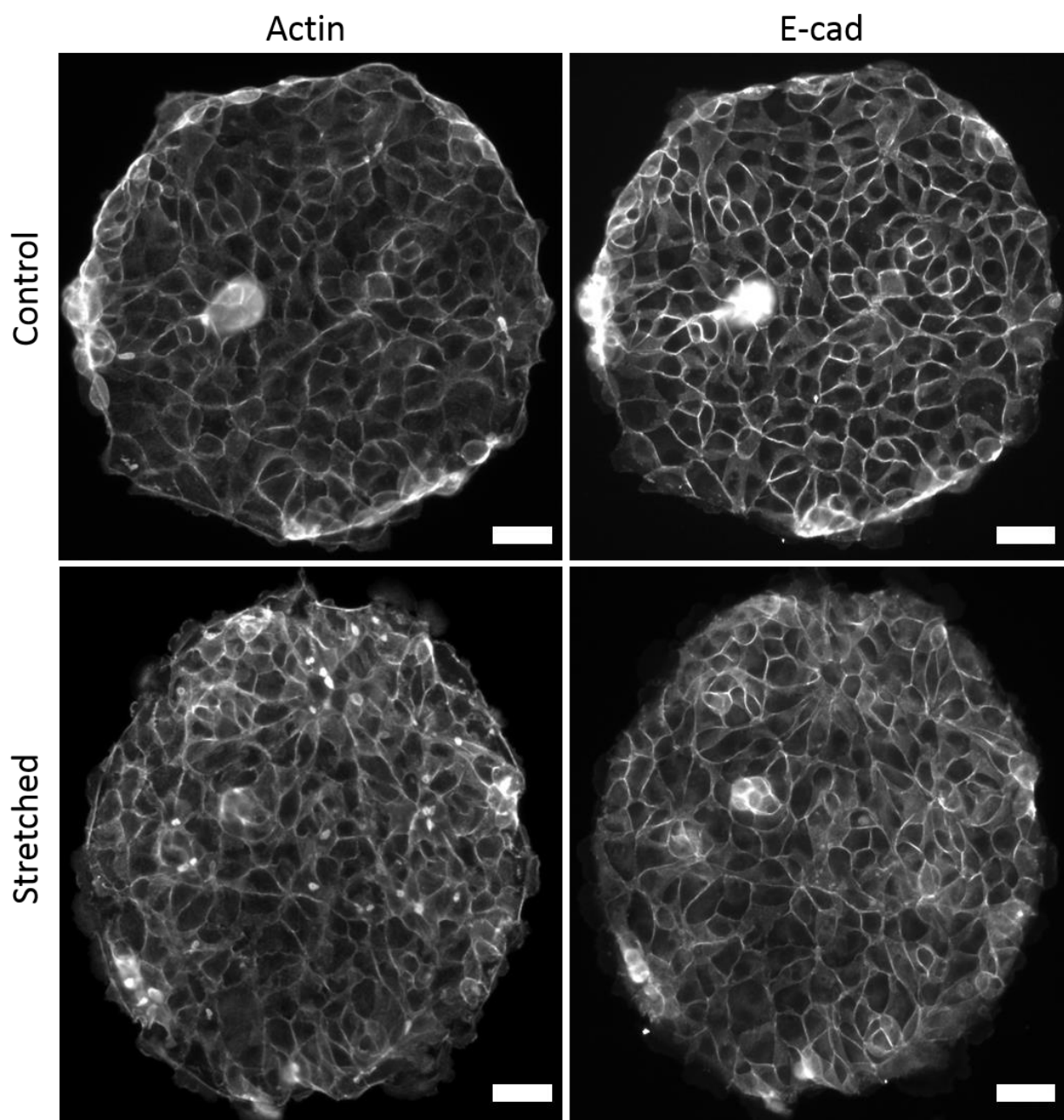
Figure S1. Immunostaining of Actin (left) and E-cadherin (right) of control (top) and stretched (bottom) MDCK islands. While the change in expression of E-cadherin is not significant (p>0.05) the expression of actin filaments in cell-cell contacts are greater in stretched cell islands (p~0.02). Scale bar is 50 μm.

CHAPTER 6

SUMMARY AND FUTURE RESEARCH

6.1 Electrotaxis of epithelial monolayers

Electrotaxis, the biased motion of cells along the field lines of an externally applied electric field is a factor involved in physiological processes such as wound healing and metastatic disease. This study focused on the collective migration of epithelial monolayers under a direct current electric field (DC EF) in vitro and in particular, the effect of pharmacological modulation of actin and myosin in their electrotaxis response. For this purpose, monolayers were treated with several pharmacological inhibitors (e.g. Jasplakinolide, Blebbistatin, Calyculin A, and Cytochalasin D) that tune actin organization or contractility either higher or lower. Monolayer speed and directionality was quantified by micro-PIV. A summary of our findings are listed here:

- PIV data of the epithelial cell populations showed that the speed of cell migration is not altered by application of DC electric field.

- Promotion of actin polymerization with Jasplakinolide of low concentration (1 nM) slightly disturbed the electrotaxis response while 50 nM Jasplakinolide attenuated the cathodal migration of the monolayer. Depolymerization of actin filaments with 0.2 mM cytochalasin D halted the cell migration without and with electric field confirming that a basal level of F-actin is required for cell migration.

- Decreasing cell contractility with 20 mM blebbistatin did not affect cathodal migration of the monolayer but slowed down the monolayer speed without and with presence of electric field. On the other hand, increasing cell contractility with 5 nM calyculin A significantly impaired the cathode-directed collective migration of the monolayers with minor effect on monolayer speed.

- These results suggest that DC electric field does not alter the mechanism by which epithelial sheets migrate and it largely affects cell polarity rather than cell migration speeds.

6.2 The effect of substrate stretch on traction force of epithelial islands

Adherent cells in soft tissues exert traction forces on their underlying micro-environment. Quantification of cell traction forces has aided in better understanding of mechanotransduction in cells and therefore of many fundamental biological processes such as morphogenesis, wound healing of tissues and organs, and metastasis. Application of external mechanical signals such as substrate stretch alters traction forces and regulates growth, migration, proliferation, and differentiation in different cell types. Our focus here was in vitro measurement of epithelial traction stresses under uniaxial substrate stretch using biocompatible substrates with similar mechanical properties as those in vivo (e.g. PDMS-based elastomers). Here, Fourier transform traction cytometry (FTTC) was employed to extract the traction vector field of cell colonies from the displacement field (measured using PIV) of the underlying incompressible substrate and its elastic properties.

- We introduced a straightforward protocol which uses sphere indentation to measure the elastic modulus of soft silicone substrates for FTTC. The protocol used a wide-field fluorescent microscope to measure indenter size and substrate deflection under the indenter, and therefore enabled us to calculate the Young's modulus of the substrate using the modified Hertz model.

- Prior to cell traction force microscopy using FTTC, we used the principles of FTTC to develop a non-intrusive direct method of wall shear stress measurement in rectangular PDMS channels. FTTC extracted the shear stress field from the displacement field of the channel wall made of an elastomer with low stiffness. The wall stiffness was measured using the stiffness

measurement method detailed in this dissertation. FTTC results were validated by the Newton's law of viscosity.

- FTTC was then deployed to measure traction stress field of miropatterned MDCK II islands. A custom designed stainless steel with laser-drilled holes was used to micropattern the cells on silicone elastomers. FTTC results showed that the traction force is directed toward the island center and enhanced radially from the island center to periphery. In this study, stretch-induced spaciotemporal changes in strain energy and intra-sheet forces, cytoskeletal rearrangements, and expression of actin and key cell-cell adhesion proteins such as E-cadherin was the main focus. A significant and quick escalation of traction force upon stretch was noticed. Such quick elastic response of the epithelial islands to stretch slowly evolved with time. The cell sheet tension for stretched cells at a midline perpendicular to the stretch direction was significantly increased upon stretch. The cell sheet tension at a midline parallel to the stretch direction was also increased and evolved with time indicating the respond of the island to homogenize its internal stress. The expression of actin within cells and in cell-cell contact was not significantly altered upon stretch.

6.3 Direction for future research

6.3.1 Bioelectric control of epithelial tissues

Coherent population of cells respond to their immediate micro-environment by cytoskeletal rearrangements induced by complex cellular signaling networks. These colonies of cells show collective behavior in response to electrical signals during processes such as metastatic cancer and wound healing. Such collective migration of cells can be spatiotemporally manipulated and controlled [15]. The collective migration of epithelial monolayers studied here can be further

studied in vitro via simple yet versatile electrotaxis chambers designed with different geometries. These frameworks can control migration by allowing tissues to respond locally to applied stimuli while producing predictable global outcomes [15]. Such designs can enable us to spatiotemporally control the directional migration of epithelium which may be useful for manipulating critical endogenous events involving collective cell migration such as wound healing.

6.3.2 The role of key stress bearing proteins to maintain the coherency of epithelial islands upon stretch

In epithelial tissues, E-cadherin bears excessive tension applied upon cells by stretch [125] to prevent cell-cell ruptures [126] and maintain the coherency of the epithelium. α-catenin is also reported to be a key mechanosensing cytosolic protein that unfolds under tension as a strain gauge in series with actin and E-cadherin [127, 128]. This in turn results in myosin II-independent accumulation of vinculin and therefore release of F-actin binding sites and actomyosin recruitment in cell-cell contacts [129, 130]. The role of these proteins upon stretch can be further studied by traction force microscopy. Complementary to our studies, substrate stretch of different strain levels and directions can be applied to normal and protein-knock down epithelial islands and the influence of tens of such proteins in their mechanical response can be studied by FTTC.

REFERENCES

[1]   R. Nuccitelli, P. Nuccitelli, S. Ramlatchan, R. Sanger, and P. J. Smith, "Imaging the electric field associated with mouse and human skin wounds," *Wound repair and regeneration,* vol. 16, pp. 432-441, 2008.

[2]   X. Trepat, M. R. Wasserman, T. E. Angelini, E. Millet, D. A. Weitz, J. P. Butler*, et al.*, "Physical forces during collective cell migration," *Nature physics,* vol. 5, pp. 426-430, 2009.

[3]   D. T. Tambe, C. C. Hardin, T. E. Angelini, K. Rajendran, C. Y. Park, X. Serra-Picamal*, et al.*, "Collective cell guidance by cooperative intercellular forces," *Nature materials,* vol. 10, pp. 469-475, 2011.

[4]   D. Falconnet, G. Csucs, H. M. Grandin, and M. Textor, "Surface engineering approaches to micropattern surfaces for cell-based assays," *Biomaterials,* vol. 27, pp. 3044-3063, 2006.

[5]   L. Wen-Wen, C. Zhen-Ling, and X.-Y. JIANG, "Methods for cell micropatterning on two-dimensional surfaces and their applications in biology," *Chinese Journal of Analytical Chemistry,* vol. 37, pp. 943-949, 2009.

[6]   H. Jang, J. Notbohm, B. Gweon, Y. Cho, C. Y. Park, S.-H. Kee*, et al.*, "Homogenizing cellular tension by hepatocyte growth factor in expanding epithelial monolayer," *Scientific Reports,* vol. 8, 2017.

[7]   U. S. Schwarz, N. Q. Balaban, D. Riveline, A. Bershadsky, B. Geiger, and S. Safran, "Calculation of forces at focal adhesions from elastic substrate data: the effect of localized force and the need for regularization," *Biophysical journal,* vol. 83, pp. 1380-1394, 2002.

[8]   J. P. Butler, I. M. Tolic-Nørrelykke, B. Fabry, and J. J. Fredberg, "Traction fields, moments, and strain energy that cells exert on their surroundings," *American Journal of Physiology-Cell Physiology,* vol. 282, pp. C595-C605, 2002.

[9]   R. W. Style, R. Boltyanskiy, G. K. German, C. Hyland, C. W. MacMinn, A. F. Mertz*, et al.*, "Traction force microscopy in physics and biology," *Soft matter,* vol. 10, pp. 4047-4055, 2014.

[10]   E. Lee, M. L. Ewald, M. Sedarous, T. Kim, B. W. Weyers, R. H. Truong*, et al.*, "Deletion of the cytoplasmic domain of N-cadherin reduces, but does not eliminate, traction force-transmission," *Biochemical and biophysical research communications,* vol. 478, pp. 1640-1646, 2016.

[11]   M. Zhao, C. D. McCaig, A. Agius-Fernandez, J. V. Forrester, and K. Araki-Sasaki, "Human corneal epithelial cells reorient and migrate cathodally in a small applied electric field," *Current eye research,* vol. 16, pp. 973-984, 1997.

[12]   L. Li, R. Hartley, B. Reiss, Y. Sun, J. Pu, D. Wu*, et al.*, "E-cadherin plays an essential role in collective directional migration of large epithelial sheets," *Cellular and Molecular Life Sciences,* vol. 69, pp. 2779-2789, 2012.

[13]   J. Gao, V. K. Raghunathan, B. Reid, D. Wei, R. C. Diaz, P. Russell*, et al.*, "Biomimetic stochastic topography and electric fields synergistically enhance directional migration of corneal epithelial cells in a MMP-3-dependent manner," *Acta biomaterialia,* vol. 12, pp. 102-112, 2015.

[14]   K. Y. Nishimura, R. R. Isseroff, and R. Nuccitelli, "Human keratinocytes migrate to the negative pole in direct current electric fields comparable to those measured in mammalian wounds," *Journal of Cell Science,* vol. 109, pp. 199-207, 1996.

[15]   D. J. Cohen, W. J. Nelson, and M. M. Maharbiz, "Galvanotactic control of collective cell migration in epithelial monolayers," *Nature materials,* vol. 13, pp. 409-417, 2014.

[16]   M. Zhao, A. Agius-Fernandez, J. V. Forrester, and C. D. McCaig, "Directed migration of corneal epithelial sheets in physiological electric fields," *Investigative ophthalmology & visual science,* vol. 37, pp. 2548-2558, 1996.

[17]   M. L. Lalli and A. R. Asthagiri, "Collective Migration Exhibits Greater Sensitivity But Slower Dynamics of Alignment to Applied Electric Fields," *Cellular and molecular bioengineering,* vol. 8, pp. 247-257, 2015.

[18]   T. E. Angelini, E. Hannezo, X. Trepat, M. Marquez, J. J. Fredberg, and D. A. Weitz, "Glass-like dynamics of collective cell migration," *Proceedings of the National Academy of Sciences,* vol. 108, pp. 4714-4719, 2011.

[19]   M. Zhao, J. Pu, J. V. Forrester, and C. D. McCaig, "Membrane lipids, EGF receptors, and intracellular signals colocalize and are polarized in epithelial cells moving directionally in a physiological electric field," *The FASEB Journal,* vol. 16, pp. 857-859, 2002.

[20]   J. Pu, C. D. McCaig, L. Cao, Z. Zhao, J. E. Segall, and M. Zhao, "EGF receptor signalling is essential for electric-field-directed migration of breast cancer cells," *Journal of cell science,* vol. 120, pp. 3395-3403, 2007.

[21]   X. Meng, M. Arocena, J. Penninger, F. H. Gage, M. Zhao, and B. Song, "PI3K mediated electrotaxis of embryonic and adult neural progenitor cells in the presence of growth factors," *Experimental neurology,* vol. 227, pp. 210-217, 2011.

[22]   J. Zhang, M. Calafiore, Q. Zeng, X. Zhang, Y. Huang, R. A. Li*, et al.*, "Electrically guiding migration of human induced pluripotent stem cells," *Stem Cell Reviews and Reports,* vol. 7, pp. 987-996, 2011.

[23]   G. M. Allen, A. Mogilner, and J. A. Theriot, "Electrophoresis of cellular membrane components creates the directional cue guiding keratocyte galvanotaxis," *Current Biology,* vol. 23, pp. 560-568, 2013.

[24]   Y. Sun, H. Do, J. Gao, R. Zhao, M. Zhao, and A. Mogilner, "Keratocyte fragments and cells utilize competing pathways to move in opposite directions in an electric field," *Current Biology,* vol. 23, pp. 569-574, 2013.

[25]   L. Guo, C. Xu, D. Li, X. Zheng, J. Tang, J. Bu*, et al.*, "Calcium Ion Flow Permeates Cells through SOCs to Promote Cathode-Directed Galvanotaxis," *PloS one,* vol. 10, p. e0139865, 2015.

[26]   Y. J. Huang, G. Hoffmann, B. Wheeler, P. Schiapparelli, A. Quinones-Hinojosa, and P. Searson, "Cellular microenvironment modulates the galvanotaxis of brain tumor initiating cells," *Sci Rep,* vol. 6, p. 21583, Feb 22 2016.

[27]   P. W. Luther, H. B. Peng, and J. J. Lin, "Changes in cell shape and actin distribution induced by constant electric fields," *Nature,* vol. 303, pp. 61-4, May 5-11 1983.

[28]   H. L. Zhang and H. B. Peng, "Mechanism of acetylcholine receptor cluster formation induced by DC electric field," *PloS one,* vol. 6, p. e26805, 2011.

[29]   S. Even-Ram, A. D. Doyle, M. A. Conti, K. Matsumoto, R. S. Adelstein, and K. M. Yamada, "Myosin IIA regulates cell motility and actomyosin–microtubule crosstalk," *Nature cell biology,* vol. 9, pp. 299-309, 2007.

[30]   K. Zhu, Y. Sun, A. Miu, M. Yen, B. Liu, Q. Zeng*, et al.*, "cAMP and cGMP Play an Essential Role in Galvanotaxis of Cell Fragments," *J Cell Physiol,* vol. 231, pp. 1291-300, Jun 2016.

[31]   C. D. McCaig, B. Song, and A. M. Rajnicek, "Electrical dimensions in cell science," *Journal of cell science,* vol. 122, pp. 4267-4276, 2009.

[32]   B. Song, Y. Gu, J. Pu, B. Reid, Z. Zhao, and M. Zhao, "Application of direct current electric fields to cells and tissues in vitro and modulation of wound electric field in vivo," *Nature protocols,* vol. 2, pp. 1479-1489, 2007.

[33]   W. Thielicke and E. Stamhuis, "PIVlab–towards user-friendly, affordable and accurate digital particle image velocimetry in MATLAB," *Journal of Open Research Software,* vol. 2, 2014.

[34]   A. Barker, L. Jaffe, and J. Vanable, "The glabrous epidermis of cavies contains a powerful battery," *American Journal of Physiology-Regulatory, Integrative and Comparative Physiology,* vol. 242, pp. R358-R366, 1982.

[35]   M. Chiang, K. R. Robinson, and J. W. Vanable, "Electrical fields in the vicinity of epithelial wounds in the isolated bovine eye," *Experimental eye research,* vol. 54, pp. 999-1003, 1992.

[36]   M. Zhao, B. Song, J. Pu, T. Wada, B. Reid, G. Tai*, et al.*, "Electrical signals control wound healing through phosphatidylinositol-3-OH kinase-γ and PTEN," *Nature,* vol. 442, pp. 457-460, 2006.

[37]   L. Q. Wan, K. Ronaldson, M. Park, G. Taylor, Y. Zhang, J. M. Gimble*, et al.*, "Micropatterned mammalian cells exhibit phenotype-specific left-right asymmetry," *Proceedings of the National Academy of Sciences,* vol. 108, pp. 12295-12300, 2011.

[38]   M. R. Bubb, A. Senderowicz, E. A. Sausville, K. Duncan, and E. D. Korn, "Jasplakinolide, a cytotoxic natural product, induces actin polymerization and competitively inhibits the binding of phalloidin to F-actin," *Journal of Biological Chemistry,* vol. 269, pp. 14869-14871, 1994.

[39]   A. Ponti, M. Machacek, S. L. Gupton, C. Waterman-Storer, and G. Danuser, "Two distinct actin networks drive the protrusion of migrating cells," *Science,* vol. 305, pp. 1782-1786, 2004.

[40]   M. R. Bubb, I. Spector, B. B. Beyer, and K. M. Fosen, "Effects of Jasplakinolide on the Kinetics of Actin Polymerization AN EXPLANATION FOR CERTAIN IN VIVO OBSERVATIONS," *Journal of Biological Chemistry,* vol. 275, pp. 5163-5170, 2000.

[41]   G. E. Peng, S. R. Wilson, and O. D. Weiner, "A pharmacological cocktail for arresting actin dynamics in living cells," *Molecular biology of the cell,* vol. 22, pp. 3986-3994, 2011.

[42]   I. Tardieux, P. Webster, J. Ravesloot, W. Boron, J. A. Lunn, J. E. Heuser*, et al.*, "Lysosome recruitment and fusion are early events required for trypanosome invasion of mammalian cells," *Cell,* vol. 71, pp. 1117-1130, 1992.

[43]   J. P. Hoj, J. A. Davis, K. E. Fullmer, D. J. Morrell, N. E. Saguibo, J. T. Schuler*, et al.*, "Cellular contractility changes are sufficient to drive epithelial scattering," *Experimental cell research,* vol. 326, pp. 187-200, 2014.

[44]   A. F. Straight, A. Cheung, J. Limouze, I. Chen, N. J. Westwood, J. R. Sellers*, et al.*, "Dissecting temporal and spatial control of cytokinesis with a myosin II Inhibitor," *Science,* vol. 299, pp. 1743-1747, 2003.

[45] M. Kovács, J. Tóth, C. Hetényi, A. Málnási-Csizmadia, and J. R. Sellers, "Mechanism of blebbistatin inhibition of myosin II," *Journal of Biological Chemistry,* vol. 279, pp. 35557-35563, 2004.

[46] J. S. Allingham, R. Smith, and I. Rayment, "The structural basis of blebbistatin inhibition and specificity for myosin II," *Nature structural & molecular biology,* vol. 12, pp. 378-379, 2005.

[47] N. Kawabata and M. Matsuda, "Cell Density-Dependent Increase in Tyrosine-Monophosphorylated ERK2 in MDCK Cells Expressing Active Ras or Raf," *PloS one,* vol. 11, p. e0167940, 2016.

[48] Z. M. Goeckeler and R. B. Wysolmerski, "Myosin light chain kinase-regulated endothelial cell contraction: the relationship between isometric tension, actin polymerization, and myosin phosphorylation," *The Journal of Cell Biology,* vol. 130, pp. 613-627, 1995.

[49] J. Stull, P. Lin, J. Krueger, J. Trewhella, and G. Zhi, "Myosin light chain kinase: functional domains and structural motifs," *Acta physiologica scandinavica,* vol. 164, pp. 471-482, 1998.

[50] J. Stricker, Y. Aratyn-Schaus, P. W. Oakes, and M. L. Gardel, "Spatiotemporal constraints on the force-dependent growth of focal adhesions," *Biophysical journal,* vol. 100, pp. 2883-2893, 2011.

[51] A. M. Handorf, Y. Zhou, M. A. Halanski, and W. J. Li, "Tissue stiffness dictates development, homeostasis, and disease progression," *Organogenesis,* vol. 11, pp. 1-15, 2015.

[52] R. J. Pelham and Y.-l. Wang, "Cell locomotion and focal adhesions are regulated by substrate flexibility," *Proceedings of the National Academy of Sciences,* vol. 94, pp. 13661-13665, December 9, 1997 1997.

[53] C. M. Lo, Wang, H. B., Dembo, M., and Wang, Y. L., "Cell movement is guided by the rigidity of the substrate," *Biophysical Journal,* vol. 79, pp. 144-152, 2000.

[54] P. J. Dennis E. Discher, Yu-li Wang, "Tissue Cells Feel and Respond to the Stiffness of Their Substrate," *Science,* vol. 310, pp. 1139-1143, 2005.

[55] C. E. Kandow, P. C. Georges, P. A. Janmey, and K. A. Beningo, "Polyacrylamide Hydrogels for Cell Mechanics: Steps Toward Optimization and Alternative Uses," vol. 83, pp. 29-46, 2007.

[56] I. D. Johnston, D. K. McCluskey, C. K. L. Tan, and M. C. Tracey, "Mechanical characterization of bulk Sylgard 184 for microfluidics and microengineering," *Journal of Micromechanics and Microengineering,* vol. 24, p. 035017, 2014.

[57] R. W. Style, R. Boltyanskiy, G. K. German, C. Hyland, C. W. MacMinn, A. F. Mertz*, et al.*, "Traction force microscopy in physics and biology," *Soft Matter,* vol. 10, pp. 4047-55, Jun 21 2014.

[58] E. Lee, M. Ewald, M. Sedarous, T. Kim, B. W. Weyers, R. H. Truong*, et al.*, "Deletion of the cytoplasmic domain of N-cadherin reduces, but does not eliminate, traction force-transmission," *Biochem Biophys Res Commun,* Sep 2 2016.

[59] M. T. Frey, A. Engler, D. E. Discher, J. Lee, and Y. L. Wang, "Microscopic methods for measuring the elasticity of gel substrates for cell culture: microspheres, microindenters, and atomic force microscopy," *Methods in cell biology,* vol. 83, pp. 47-65, 2007.

[60] D. Lee, M. M. Rahman, Y. Zhou, and S. Ryu, "Three-Dimensional Confocal Microscopy Indentation Method for Hydrogel Elasticity Measurement," *Langmuir,* vol. 31, pp. 9684-93, Sep 08 2015.

[61] M. T. Frey, A. Engler, D. E. Discher, J. Lee, and Y. L. Wang, "Microscopic Methods for Measuring the Elasticity of Gel Substrates for Cell Culture: Microspheres, Microindenters, and Atomic Force Microscopy," vol. 83, pp. 47-65, 2007.

[62] E. K. Dimitriadis, F. Horkay, J. Maresca, B. Kachar, and R. S. Chadwick, "Determination of elastic moduli of thin layers of soft material using the atomic force microscope," *Biophysical Journal,* vol. 82, pp. 2798-2810, 2002.

[63] H. R. Hertz, "Uber die Beruhrung fester elastischer Korper und Uber die Harte," *Verhandlung des Vereins zur Beforderung des GewerbefleiBes, Berlin,* p. 449, 1882.

[64]   L. Böhm, S. Jankhah, J. Tihon, P. R. Bérubé, and M. Kraume, "Application of the electrodiffusion method to measure wall shear stress: integrating theory and practice," *Chemical Engineering & Technology,* vol. 37, pp. 938-950, 2014.

[65]   P. H. Alfredsson, A. V. Johansson, J. H. Haritonidis, and H. Eckelmann, "The fluctuating wall-shear stress and the velocity field in the viscous sublayer," *The Physics of fluids,* vol. 31, pp. 1026-1033, 1988.

[66]   J. Naughton and M. Hind, "Multi-image oil-film interferometry skin friction measurements," *Measurement Science and Technology,* vol. 24, p. 124003, 2013.

[67]   R. Gottlieb, F. Shu, M. Kameneva, J. Antaki, Z. Wu, and G. Burgreen, "Liquid crystal shear stress sensor for blood and other opaque viscous fluids," *Journal of Flow Visualization and Image Processing,* vol. 16, pp. 51-71, 2009.

[68]   P. Ireland and T. Jones, "Liquid crystal measurements of heat transfer and surface shear stress," *Measurement Science and Technology,* vol. 11, p. 969, 2000.

[69]   C. Hughes, D. Dutta, Y. Bashirzadeh, K. Ahmed, and S. Qian, "Measuring shear stress with A Micro Fluidic sensor to improve aerodynamic efficiency," in *53rd AIAA Aerospace Sciences Meeting. AIAA*, 2015.

[70]   F. Jiang, Y. Tai, B. Gupta, R. Goodman, S. Tung, J. Huang*, et al.*, "A micromachined shear stress sensor array," in *Proc. IEEE MEMS-96 Workshop*, 1996, pp. 110-115.

[71]   Y. Ou, F. Qu, G. Wang, M. Nie, Z. Li, W. Ou*, et al.*, "A MEMS thermal shear stress sensor produced by a combination of substrate-free structures with anodic bonding technology," *Applied Physics Letters,* vol. 109, p. 023512, 2016.

[72]   J. Weiss, Q. Schwaab, Y. Boucetta, A. Giani, C. Guigue, P. Combette*, et al.*, "Simulation and testing of a MEMS calorimetric shear-stress sensor," *Sensors and Actuators A: Physical,* vol. 253, pp. 210-217, 2017.

[73]   F. Jiang, G.-B. Lee, Y.-C. Tai, and C.-M. Ho, "A flexible micromachine-based shear-stress sensor array and its application to separation-point detection," *Sensors and Actuators A: Physical,* vol. 79, pp. 194-203, 2000.

[74]   J. W. Naughton and M. Sheplak, "Modern developments in shear-stress measurement," *Progress in Aerospace Sciences,* vol. 38, pp. 515-570, 2002.

[75]   H. Schlichting and K. Gersten, "Boundary Layer Theory Springer-Verlag," *Berlin, Heidelberg,* 2000.

[76]   J. H. Wang and J.-S. Lin, "Cell traction force and measurement methods," *Biomechanics and modeling in mechanobiology,* vol. 6, p. 361, 2007.

[77]   B. Li, L. Xie, Z. C. Starr, Z. Yang, J. S. Lin, and J. H. C. Wang, "Development of micropost force sensor array with culture experiments for determination of cell traction forces," *Cytoskeleton,* vol. 64, pp. 509-518, 2007.

[78]   C. Brücker, J. Spatz, and W. Schröder, "Feasability study of wall shear stress imaging using microstructured surfaces with flexible micropillars," *Experiments in fluids,* vol. 39, pp. 464-474, 2005.

[79]   S. Große and W. Schröder, "Dynamic wall-shear stress measurements in turbulent pipe flow using the micro-pillar sensor MPS 3," *International Journal of Heat and Fluid Flow,* vol. 29, pp. 830-840, 2008.

[80]   T.-V. Nguyen, R. Kazama, H. Takahashi, T. Takahata, K. Matsumoto, and I. Shimoyama, "A wall shear stress sensor using a pair of sidewall doped cantilevers," *Journal of Micromechanics and Microengineering,* vol. 27, p. 075017, 2017.

[81]   F. Gijsen, A. Goijaerts, F. Van de Vosse, and J. Janssen, "A new method to determine wall shear stress distribution," *Journal of Rheology,* vol. 41, pp. 995-1006, 1997.

[82]   S. K. Sia and G. M. Whitesides, "Microfluidic devices fabricated in poly (dimethylsiloxane) for biological studies," *Electrophoresis,* vol. 24, pp. 3563-3576, 2003.

[83]   B. Mueller, "Measuring Shear Stress in Microfluidics using Traction Force Microscopy," *Experimental and Applied Mechanics, Volume 6,* pp. 135-136, 2011.

[84]   N. Mori and K.-A. Chang, "Introduction to MPIV," *User manual and program available online at http://sauron. civil. eng. osaka-cu. ac. jp/~ mori/softwares/mpiv,* 2003.

[85]   W. S. Rasband, "ImageJ, US National Institutes of Health," *http://rsb. info. nih. gov/ij/(1997-2007),* 2007.

[86]   T. Ferreira and W. Rasband, "ImageJ user guide," *ImageJ/Fiji,* vol. 1, 2012.

[87]   S. V. Plotnikov, B. Sabass, U. S. Schwarz, and C. M. Waterman, "High-resolution traction force microscopy," *Methods in cell biology,* vol. 123, p. 367, 2014.

[88]   B. Sabass, M. L. Gardel, C. M. Waterman, and U. S. Schwarz, "High resolution traction force microscopy based on experimental and computational advances," *Biophysical journal,* vol. 94, pp. 207-220, 2008.

[89]   S.-Y. Lee, S. T. Wereley, L. Gui, W. Qu, and I. Mudawar, "Microchannel flow measurement using micro particle image velocimetry," in *Proc. ASME/IMECE*, 2002.

[90]   D. Lee, M. M. Rahman, Y. Zhou, and S. Ryu, "Three-dimensional confocal microscopy indentation method for hydrogel elasticity measurement," *Langmuir,* vol. 31, pp. 9684-9693, 2015.

[91]   C.-M. Lo, H.-B. Wang, M. Dembo, and Y.-l. Wang, "Cell movement is guided by the rigidity of the substrate," *Biophysical journal,* vol. 79, pp. 144-152, 2000.

[92]   H. Hertz, "Über die Berührung fester elastischer Körper," *Journal für die reine und angewandte Mathematik,* vol. 92, pp. 156-171, 1882.

[93]   H. Bruus, *Theoretical microfluidics*: Oxford university press Oxford, 2007.

[94]   M. Gad-el-Hak, "The fluid mechanics of microdevices-the Freeman scholar lecture," *Transactions-American Society of Mechanical Engineers Journal of FLUIDS Engineering,* vol. 121, pp. 5-33, 1999.

[95]   M. Gad-el-Hak, "Flow Physics in Microdevices," *The Handbook of MEMS,* 2002.

[96]   R. H. Nadolink and W. W. Haigh, "Bibliography on skin friction reduction with polymers and other boundary-layer additives," *Appl. Mech. Rev,* vol. 48, pp. 351-460, 1995.

[97]   M. Gad-el-Hak, "Liquids: The holy grail of microfluidic modeling," *Physics of Fluids,* vol. 17, p. 100612, 2005.

[98]   P. A. Janmey and R. T. Miller, "Mechanisms of mechanical signaling in development and disease," *J Cell Sci,* vol. 124, pp. 9-18, 2011.

[99]   D. Ingber, "Mechanobiology and diseases of mechanotransduction," *Annals of medicine,* vol. 35, pp. 564-577, 2003.

[100]   M. A. Wozniak and C. S. Chen, "Mechanotransduction in development: a growing role for contractility," *Nature reviews Molecular cell biology,* vol. 10, pp. 34-43, 2009.

[101]   H. R. Wirtz and L. G. Dobbs, "Calcium mobilization and exocytosis after one mechanical stretch of lung epithelial cells," *Science,* vol. 250, pp. 1266-1270, 1990.

[102]   B. D. Hoffman, C. Grashoff, and M. A. Schwartz, "Dynamic molecular processes mediate cellular mechanotransduction," *Nature,* vol. 475, pp. 316-323, 2011.

[103]   C. M. Waters, K. M. Ridge, G. Sunio, K. Venetsanou, and J. I. Sznajder, "Mechanical stretching of alveolar epithelial cells increases Na+-K+-ATPase activity," *Journal of Applied Physiology,* vol. 87, pp. 715-721, 1999.

[104]   S. Yano, M. Komine, M. Fujimoto, H. Okochi, and K. Tamaki, "Mechanical stretching in vitro regulates signal transduction pathways and cellular proliferation in human epidermal keratinocytes," *Journal of Investigative Dermatology,* vol. 122, pp. 783-790, 2004.

[105]   V. Vogel and M. Sheetz, "Local force and geometry sensing regulate cell functions," *Nature reviews Molecular cell biology,* vol. 7, pp. 265-275, 2006.

[106]   S. Jungbauer, H. Gao, J. P. Spatz, and R. Kemkemer, "Two characteristic regimes in frequency-dependent dynamic reorientation of fibroblasts on cyclically stretched substrates," *Biophysical journal,* vol. 95, pp. 3470-3478, 2008.

[107]   A. R. Harris, L. Peter, J. Bellis, B. Baum, A. J. Kabla, and G. T. Charras, "Characterizing the mechanics of cultured cell monolayers," *Proceedings of the National Academy of Sciences,* vol. 109, pp. 16449-16454, 2012.

[108]   R. Krishnan, C. Y. Park, Y.-C. Lin, J. Mead, R. T. Jaspers, X. Trepat*, et al.*, "Reinforcement versus fluidization in cytoskeletal mechanoresponsiveness," *PloS one,* vol. 4, p. e5486, 2009.

[109]   N. Gavara, P. Roca-Cusachs, R. Sunyer, R. Farré, and D. Navajas, "Mapping cell-matrix stresses during stretch reveals inelastic reorganization of the cytoskeleton," *Biophysical journal,* vol. 95, pp. 464-471, 2008.

[110]   A. Tsukamoto, K. R. Ryan, Y. Mitsuoka, K. S. Furukawa, and T. Ushida, "Cellular traction forces increase during consecutive mechanical stretching following traction force attenuation," *Journal of Biomechanical Science and Engineering,* vol. 12, pp. 17-00118-17-00118, 2017.

[111]   J. M. Mann, R. H. Lam, S. Weng, Y. Sun, and J. Fu, "A silicone-based stretchable micropost array membrane for monitoring live-cell subcellular cytoskeletal response," *Lab on a Chip,* vol. 12, pp. 731-740, 2012.

[112]   L. Casares, R. Vincent, D. Zalvidea, N. Campillo, D. Navajas, M. Arroyo*, et al.*, "Hydraulic fracture during epithelial stretching," *Nature materials,* vol. 14, p. 343, 2015.

[113]   C. M. Cesa, N. Kirchgeßner, D. Mayer, U. S. Schwarz, B. Hoffmann, and R. Merkel, "Micropatterned silicone elastomer substrates for high resolution analysis of cellular force patterns," *Review of Scientific Instruments,* vol. 78, p. 034301, 2007.

[114] A. M. T. Quinlan, L. N. Sierad, A. K. Capulli, L. E. Firstenberg, and K. L. Billiar, "Combining dynamic stretch and tunable stiffness to probe cell mechanobiology in vitro," *PloS one,* vol. 6, p. e23272, 2011.

[115] Y. Bashirzadeh, S. Qian, and V. Maruthamuthu, "Non-intrusive Measurement of Wall Shear Stress in Flow Channels," *Sensors and Actuators A: Physical,* 2018.

[116] Y. Bashirzadeh, S. Chatterji, D. Palmer, S. Dumbali, S. Qian, and V. Maruthamuthu, "Stiffness Measurement of Soft Silicone Substrates for Mechanobiology Studies Using a Widefield Fluorescence Microscope," *JoVE,* p. e57797.

[117] N. Carpi and M. Piel, "Stretching micropatterned cells on a PDMS membrane," *Journal of visualized experiments: JoVE,* 2014.

[118] Y. Shao, X. Tan, R. Novitski, M. Muqaddam, P. List, L. Williamson*, et al.*, "Uniaxial cell stretching device for live-cell imaging of mechanosensitive cellular functions," *Review of Scientific Instruments,* vol. 84, p. 114304, 2013.

[119] D. E. Anderson and M. T. Hinds, "Endothelial cell micropatterning: methods, effects, and applications," *Annals of biomedical engineering,* vol. 39, p. 2329, 2011.

[120] A. W. Feinberg, W. R. Wilkerson, C. A. Seegert, A. L. Gibson, L. Hoipkemeier-Wilson, and A. B. Brennan, "Systematic variation of microtopography, surface chemistry and elastic modulus and the state dependent effect on endothelial cell alignment," *Journal of Biomedical Materials Research Part A,* vol. 86, pp. 522-534, 2008.

[121] W. S. Rasband, "Imagej, us national institutes of health, bethesda, maryland, usa," *http://imagej. nih. gov/ij/,* 2011.

[122] S. V. Plotnikov, B. Sabass, U. S. Schwarz, and C. M. Waterman, "High-resolution traction force microscopy," in *Methods in cell biology*. vol. 123, ed: Elsevier, 2014, pp. 367-394.

[123] A. Azioune, N. Carpi, Q. Tseng, M. Thery, and M. Piel, "Protein micropatterns: A direct printing protocol using deep UVs," in *Methods in cell biology*. vol. 97, ed: Elsevier, 2010, pp. 133-146.

[124] S. P. Dumbali, L. Mei, S. Qian, and V. Maruthamuthu, "Endogenous Sheet-Averaged Tension Within a Large Epithelial Cell Colony," *Journal of biomechanical engineering,* vol. 139, p. 101008, 2017.

[125] N. Borghi, M. Sorokina, O. G. Shcherbakova, W. I. Weis, B. L. Pruitt, W. J. Nelson*, et al.*, "E-cadherin is under constitutive actomyosin-generated tension that is increased at cell–cell contacts upon externally applied stretch," *Proceedings of the National Academy of Sciences,* vol. 109, pp. 12568-12573, 2012.

[126] J. Eyckmans, T. Boudou, X. Yu, and C. S. Chen, "A hitchhiker's guide to mechanobiology," *Developmental cell,* vol. 21, pp. 35-47, 2011.

[127] T.-J. Kim, S. Zheng, J. Sun, I. Muhamed, J. Wu, L. Lei*, et al.*, "Dynamic visualization of α-catenin reveals rapid, reversible conformation switching between tension states," *Current Biology,* vol. 25, pp. 218-224, 2015.

[128] D. E. Leckband, Q. le Duc, N. Wang, and J. de Rooij, "Mechanotransduction at cadherin-mediated adhesions," *Current opinion in cell biology,* vol. 23, pp. 523-530, 2011.

[129] S. Huveneers and J. de Rooij, "Mechanosensitive systems at the cadherin–F-actin interface," *J Cell Sci,* vol. 126, pp. 403-413, 2013.

[130] S. Yonemura, Y. Wada, T. Watanabe, A. Nagafuchi, and M. Shibata, "α-Catenin as a tension transducer that induces adherens junction development," *Nature cell biology,* vol. 12, p. 533, 2010.

APPENDIX A

FUNCTION FOR CALCULATING THE YOUNG'S MODULUS OF PREPARED SOFT

SUBSTRATES

Young_Modulus.m

```matlab
% Yashar Bashirzadeh 2017
% Hertz & Dimitriadis models for stiffness measurement of substrate in kPa
function [E_hertz,E_Dimitriadis]=Young_Modulus(D,d,minF,maxF,dz,h,v)

% D is indentor diameter in um
% d is density of the indentor in g/cm^3
% minF is minimum frame number (undeformed top surface of the substrate)
% maxF is maximum frame number (max deformed surface right under the indentor)
% dz is z step in um
% h is substrate film thickness in um
% v is substrate poissons ratio

R = D/2*1e-6;
delta = dz*(maxF-minF)*1e-6;

g = 9.807;
V = (4/3)*pi*R^3;
Bf = g*V*1*998;      % Buoyant force
Wf = g*V*d*998;       % Indentor weight
F = Wf-Bf;        % Force exeted by indentor on substrate

x = (R*delta)^0.5/(h*1e-6);
a0 = (1.3442*v^2-1.4678*v+1.2876)/(v-1);
b0 = (1.5164*v^2-1.0277*v+0.6378)/(1-v);

E_hertz = 3*(1-v^2)*F/(4*R^0.5*delta^1.5);

C = 1/(1-2*a0*x/pi+4*a0^2*x^2/pi^2-
8*(a0^3+4*pi^2*b0/15)*x^3/pi^3+16*a0*(a0^3+3*pi^2*b0/5)*x^4/pi^4);

E_Dimitriadis = C*E_hertz;

E_hertz = E_hertz/1000;
E_Dimitriadis = E_Dimitriadis/1000;
```

APPENDIX B

SINGLE RUN FTTC [7, 84] FOR AN ASSEMBLY OF EXPERIMENTS

assembly_analysis.m

```matlab
% Yashar Bashirzadeh 2017

% FTTC for an assembly of experiments/positions
% Note: This code calls PIV and FTTC funcions written or modified by:
% Nobuhito Mori et al., Benedikt Sabass, Ulrich Schwarz, and Venkat Maruthamuthu
% which are all available in a general foder 'Labcode'.
% Therefore the user should have access to the 'Labcode' to run this script.

% The results are saved in user generated folders (say cell folder) numbered as: 1, 2, 3 etc

% The folder which contains all cell folders should be in the general folder 'Labcode'.

% The folder which contains all cell folders should itself be located inside a folder
% in the general folder 'Lab code'.'Lab code' itslef can be  located anywhere in PC.

% an example for correct location of cell foders:
% Z:\Yashar\LabCode\MDCK\analysis
% Here the folder 'MDCK' must be in the general foder 'LabCode' and the
% 'MDCK' folder itself contains the folder 'analysis' which is the folder that includes
% all the cell folders (1,2,...) for a particular experiment or a set of experiments.


% All aligned (time laspe) cell images should have been saved in
% order time wise) as 001.tiff, 002.tiff etc in the associated cell foder.

% All aligned (time laspe) bead images should have been saved in
% order (time wise)as 01.tiff, 02.tiff etc in the associated cell foder.

% Last bead image is the reference bead image.

% Before running the code set the current directory to LabCode/analysis


% User inputs......................................................

C_dir = 'MDCK\analysis\';% File containing all cell folders (look at the example above).
folder = [1 14];         % First and last folders to be processed.
N_BeadImages = 8;        % Numder of bead images in each folder (2 if not a time lapse).
E = 7.2;                 % Young's modulus of the substrate in kPa.
Obj = 10;                % Objective lens magnification.

% End of user inputs......................................................
```

```matlab
%................................................................
%................................................................
%................................................................
%................................................................
addpath('../disp','../traction','../mpiv_toolbox','../dace','../forces');
%...................................... Image and analysis directories

prefix_dir =['../',C_dir];

for i = folder(1):folder(2)
%copyfile([prefix_dir,num2str(i),'/log.txt'],cd)          % remove comment if template matching
if N_BeadImages<=9
suffix_dir2 =[prefix_dir,num2str(i),'/0',num2str(N_BeadImages),'.tif'];
else
suffix_dir2 =[prefix_dir,num2str(i),'/',num2str(N_BeadImages),'.tif'];
end
for j=1:N_BeadImages-1

if j<10
suffix_dir1 =[prefix_dir,num2str(i),'/0',num2str(j),'.tif'];
cell_image = [prefix_dir,num2str(i),'/00',num2str(j),'.tif'];
copyfile(cell_image,'./cell/cell_01.tif');

%CellShift;                                            % remove comment if template matching
%copyfile('./cell_shifted/shifted_cell_01.tif',cell_image); % remove comment if template matching
else
suffix_dir1 =[prefix_dir,num2str(i),'/',num2str(j),'.tif'];
cell_image = [prefix_dir,num2str(i),'/0',num2str(j),'.tif'];
copyfile(cell_image,'./cell/cell_01.tif');
 %CellShift;                                           % remove comment if template matching
 %copyfile('./cell_shifted/shifted_cell_01.tif',cell_image);% remove comment if template matching
end


%cell_image = [')\Project_ph-stretch',num2str(i),'_ch00.tif'];
% The cropped bead and cell images will be automatically copied into analysis/bead_cropped
% and renamed as bead_cropped_01 and bead_cropped_02.

%(3)...............Copying prepared images by imagej into analysis folder:

copyfile(suffix_dir1,'./bead_cropped/bead_cropped_01.tif');
copyfile(suffix_dir2,'./bead_cropped/bead_cropped_02.tif');

% For fluid shear stress experiments:
%
copyfile([prefix_dir,num2str(i),suffix_dir1],[analysis_dir,'\cell_cropped\cell_cropped_01.tif'])

% For cell stretching experiments:
 copyfile(cell_image,'./cell_cropped\cell_cropped_01.tif');
```

```matlab
% (4)................................................................FTTC

% Displacement & Traction maps are generated and they will be saved as both .fig and .tif.
% Workspace is saved as result.mat.
% Avg displacement and stress are calculated.
DispCalc;
load('Disp.mat');
DispCalc_results.grid_mat(:,:,2)=DispCalc_results.pos_x_mat;
DispCalc_results.grid_mat(:,:,1)=DispCalc_results.pos_y_mat;
save('Disp.mat','DispCalc_results','DispCalc_settings')
% disp_map;
% saveas(gcf,'disp_map_plot.fig');
TracCalc(E/3, Obj, 5);
% load('Trac.mat');
TracMap;
%caxis([0, 1])
saveas(gcf,'trac_map.fig');
close(figure (1));
%Avg_stress=mean(TracCalc_results.trac_mag);

% For fluid shear stress experiments:
% TracMapPlot(0,1,'y',1,1,1);

% For cell stretching experiments:
%TracMapPlot;
TracMapPlot(0,1,'y',1,1,4)
caxis([0, 1])
saveas(gcf,'trac_map_plot.fig');
close(figure (1));
CellTracPlot('y', 'r', 1, 4, 2);
saveas(gcf,'cell_trac_plot.fig');
close(figure (1));
save('result');

% The 'analysis' folder in the general code directory that includes all
% saved results are cut and pasted into a folder called 'results'.
% Then a reserved folder that includes origianl empty folders of the
% 'analysis' folder are copied into a new folder 'analysis' in the general
% code directory in order to be filled with second batch of images with the
% for loop.

cd '..'
movefile('analysis',[C_dir,num2str(i),'/results',num2str(j)]);

copyfile('analysis empty folders','analysis');
cd 'analysis'
%copyfile([prefix_dir,num2str(i),'/results',num2str(j),'/log.txt'],cd)
                                                  %remove the comment above if template
matching
% disp_map;
% saveas(gcf,'disp_map_plot.fig');
```

```
    end
end

% (5)...............................................Traction parameters

% Quantification of traction scalar sum, strain energy etc
% for t = folder(1):folder(2)
% for k =1:N_BeadImages-1
% mkdir ([prefix_dir,num2str(t),'/results',num2str(k),'/binary']);
% copyfile([prefix_dir,num2str(t),'/0001.tif'],...
% [prefix_dir,num2str(t),'/results',num2str(k),'/binary/binary_01.tif']);
%
% cd ([prefix_dir,num2str(t),'/results',num2str(k)]);
% F_cell;
% cd '../../../../analysis'
% end
% end
```

APPENDIX C

SINGLE RUN FTTC [7] FOR AN ASSEMBLY OF EXPERIMENTS

USING SUBSTRATE DISPLACEMENT FIELDS QUANTIFIED BY PIV LAB 1.41 [33]

pivlab_to_labcode.m

```
% Yashar Bashirzadeh 2018

% This code quantifies the traction forces by using displacement fields
% quantified by PIV lab (Thielicke et al. 2014).

% Note: This code calls FTTC funcions written or modified by
% Benedikt Sabass, Ulrich Schwarz, and Venkat Maruthamuthu
% which are all available in a general foder 'Labcode'.
% Therefore the user should have access to the 'Labcode' to run this script.


% The results are saved in user generated folders (say cell folder) numbered as: 1, 2, 3 etc

% PIV lab results should have been saved as piv_data.mat in the folder
% which contains all cell folders.

% All aligned bead images should have been loaded as a sequence in
% PIV lab in a way that PIV lab obtains all displacement fields
% (for each image pair) in one run. The order of sequence of image pairs are:
% bead image of cell 1 at time 1- reference bead image of cell 1, bead image
% of cell 1 at time 2- reference bead image of cell 1, ..., bead image of
% last cell at last time  point- reference bead iamge of last cell.


% Therefore piv_data.mat contains time-lapse displacement fields of
% all cells/islands.

% The folder which contains all cell folders should be in the general folder 'Labcode'.

% The folder which contains all cell folders should itself be located inside a folder
% in the general folder 'Lab code'. 'Lab code' itslef can be  located anywhere in PC.

% an example for correct location of cell foders:
% Z:\Yashar\LabCode\MDCK\analysis
% Here the folder 'MDCK' must be in the general foder 'LabCode' and the
% 'MDCK' folder itself contains the folder 'analysis' which is the folder that includes
% all the cell folders (1,2,...) for a particular experiment or a set of experiments.


% All aligned (time laspe) cell images should have been saved in in the
% associated cell foder.

% All aligned (time laspe) bead images should have been saved in the
```

```matlab
% associated cell foder.
clc




%...............................................................
% User defined inputs..............................................


% Before running the code set the current directory to LabCode/analysis
% which is the current directory containing cell folders:
cd 'Z:\Yashar\epithelial stretch\PC-backup\cell stretching\TFM Code\LabCode\analysis'


C_dir = 'MDCK2\analysis\'; % File containing cell folders and piv_data.mat
load (['../',C_dir,'piv_data.mat'])


folder1=1;       % This should be 1 (folder number of first cell folder)
folder2=9;       % Number of cell folders (folder number of last cell folder)
for n=folder1:folder2
E = 7.2;         % Young's modulus of the substrate in kPa.
Obj = 10;        % Objective lens magnification.
N_BeadImages=14; % number of bead images (including reference)of each cell folder

% Here write the values of grid size, overlap, and final grid size (if 'fft' method used)
% which was set in PIV lab. Also, write the user defined max displacement.
DispCalc_settings.initial_grid_size=64;
DispCalc_settings.overlap=0.5;
DispCalc_settings.final_grid_size = 32;
DispCalc_settings.no_of_recursions=round(log2(DispCalc_settings.initial_grid_size*DispCalc_settin
gs.overlap/DispCalc_settings.final_grid_size)) + 1;
% Leave the line above as it is.
DispCalc_settings.maximum_displacement_set = 30;
% DispCalc_settings.piv_type = 'fft';
% DispCalc_settings.filter_type = 'stdev=3, local median fileter=3,0.1';
%...............................................................
%...............................................................
%...............................................................
%End of user defined inputs.......................................................


folder=n;
start=1+(N_BeadImages-1)*(n-1);
stop=start+N_BeadImages-2;
addpath('../traction','../dace','../forces');
prefix_dir =['../',C_dir];
%copyfile([prefix_dir,num2str(folder),'/log.txt'],cd)
%remove the above cooment if template matching was applied
if N_BeadImages<=9
suffix_dir2 =[prefix_dir,num2str(folder),'/0',num2str(N_BeadImages),'.tif'];
```

```matlab
else
suffix_dir2 =[prefix_dir,num2str(folder),'/',num2str(N_BeadImages),'.tif'];
end

j=1;
for i=start:stop
addpath('../disp');
    if j<10
suffix_dir1 =[prefix_dir,num2str(folder),'/0',num2str(j),'.tif'];
cell_image = [prefix_dir,num2str(folder),'/00',num2str(j),'.tif'];
copyfile(cell_image,'./cell/cell_01.tif');

%CellShift;                                              % in case template
matching is applied
%copyfile('./cell_shifted/shifted_cell_01.tif',cell_image);       % in case template
matching is applied
else
suffix_dir1 =[prefix_dir,num2str(folder),'/',num2str(j),'.tif'];
cell_image = [prefix_dir,num2str(folder),'/0',num2str(j),'.tif'];
copyfile(cell_image,'./cell/cell_01.tif');
%CellShift;                                              % in case template
matching is applied
%copyfile('./cell_shifted/shifted_cell_01.tif',cell_image);       % in case template
matching is applied
end

% The cropped bead images will be automatically copied into analysis/bead_cropped
% and renamed as bead_cropped_01 and bead_cropped_02.

%(3)...............Copying prepared images by imagej into analysis folder:

copyfile(suffix_dir1,'./bead_cropped/bead_cropped_01.tif');
copyfile(suffix_dir2,'./bead_cropped/bead_cropped_02.tif');

% For cell stretching experiments:
 copyfile(cell_image,'./cell_cropped\cell_cropped_01.tif');

X=x{i,1};
Y=y{i,1};
u_filterednew=u_filtered{i,1};
v_filterednew=flipud(v_filtered{i,1});
pos = [X(:), Y(:)];
disp = [u_filterednew(:), v_filterednew(:)];
DispCalc_results.pos=pos;
DispCalc_results.pos_x_mat=X;
DispCalc_results.pos_y_mat=Y;
DispCalc_results.disp_dx_mat=u_filterednew;
DispCalc_results.disp_dy_mat=v_filterednew;
DispCalc_results.disp=disp;
DispCalc_results.grid_mat(:,:,1)=DispCalc_results.pos_y_mat/1000;
DispCalc_results.grid_mat(:,:,2)=DispCalc_results.pos_x_mat/1000;

save('Disp.mat','DispCalc_results','DispCalc_settings')
```

```matlab
TracCalc(E/3, Obj, 5);
TracMap;
saveas(gcf,'trac_map.fig');
close(figure (1));
TracMapPlot(0,1,'y',1,1,4)
saveas(gcf,'trac_map_plot.fig');
close(figure (1));
CellTracPlot('y', 'r', 1, 2, 2);
saveas(gcf,'cell_trac_plot.fig');
close(figure (1));
save('result');

cd '..'
a=rmdir ([C_dir,num2str(folder),'/results',num2str(j)],'s');
movefile('analysis',[C_dir,num2str(folder),'/results',num2str(j)]);
copyfile('analysis empty folders','analysis');
cd 'analysis'
%copyfile([prefix_dir,num2str(folder),'/results',num2str(j),'/log.txt'],cd)    % in case template
matching is applied
j=j+1;

end
%load (['../',C_dir,'piv_data.mat'])
%cd 'C:\Users\ybash001\Desktop\PIVlab'
end
```

APPENDIX D

FUNCTION FOR CALCULATING THE VECTOR AND SCALAR SUM OF TRACTION

FORCES FOR ONE CELL OR CELL ISLAND USING ELLIPTICAL MASKS

TF_ellipse.m

```matlab
% Yashar Bashirzadeh 2018
% Code to calculate the vector and scalar sum of traction forces
% for one cell or cell island using elliptical masks.

% Edited version of TF_circle.m by  Dr. Venkat_Maruthamuthu for circular masks

% - Binary masks for elliptical cell/cell island ('binary_xy.tif')
%   should be in binary/
% - Traction results as trac.mat should be in current folder

% Outputs:
%        TFellipse.mat has:
%        TF (vector sum, x and y comp, and scalar sum (in nN)
%            as well as imb (as a percentage) for the cell/cell island)
%        TF_mask (ellipse semi-major and semi-mnor lengths,and centre)
%
function TF_ellipse
if nargin < 1
    dil_perc = 10;
end
load Trac.mat

ObjMag = TracCalc_settings.ObjMag;
TracGridSize = TracCalc_settings.GridSize;

cell_files = dir('./binary/binary*.*');
num_cell_files = numel(cell_files);

for num_cell_file = 1:1:(num_cell_files)

binary_mat = imread(fullfile('./binary/',cell_files(num_cell_file).name));
% to find the center and semi-major and semi-minor axes of the white elliptical region:
xmin = size(binary_mat,2);
ymin = size(binary_mat,1);
for di1 = 1:1:size(binary_mat,1)
    for di2 = 1:1:size(binary_mat,2)
        if binary_mat(di1,di2) == 255
            if di2 < xmin
                xmin = di2;
            end
            if di1 < ymin
                ymin = di1;
```

```matlab
            end
        end
    end
end


xmax = 1;
ymax = 1;
for di1 = size(binary_mat,1):-1:1
for di2 = size(binary_mat,2):-1:1
if binary_mat(di1,di2) == 255
if di2 > xmax
xmax = di2;
end
if di1 > ymax
ymax = di1;
end
end
end
end

a=(ymax-ymin)/2;
b=(xmax-xmin)/2;
center_x=xmin+b;
center_y=ymin+a;

t = TracCalc_results(num_cell_file).trac;
tm = TracCalc_results(num_cell_file).trac_mag;
p = TracCalc_results(num_cell_file).pos;
for i=1:1:length(p)
    if binary_mat(uint16(p(i,2)),uint16(p(i,1)))==0
    t(i,1)=0;
    t(i,2)=0;
    tm(i)=0;
    end
end
% vector sum of traction stresses:
cell_t_sum=[sum(t(:,1)) sum(t(:,2))];
%scalar sum of traction stress magnitudes:
cell_tm_sum=sum(tm(:));
% traction to force conversion factor
conv_fac = 0.001 * (6.45*TracGridSize/ObjMag)^2; % pN->nN; grid area in um2
cell_f_sum=conv_fac.*cell_t_sum;
cell_fm_sum=conv_fac.*cell_tm_sum;
fprintf('For cell %d:\n', num_cell_file)
tfvs = (((cell_f_sum(1,1))^2)+((cell_f_sum(1,2))^2))^0.5;
fprintf('TF vector sum is %.2f nN\n', tfvs)
fprintf('with x component: %.2f nN\n', cell_f_sum(1,1))
fprintf('with y component: %.2f nN\n', cell_f_sum(1,2))
fprintf('TF scalar sum is %.2f nN\n',cell_fm_sum)
imb = 100*tfvs/cell_fm_sum;
fprintf('Percent imbalance is %.1f\n', imb)
```

```matlab
        fprintf('\n')
        TF(num_cell_file).tf_vec_sum = tfvs;
        TF(num_cell_file).tf_x_vec_sum = cell_f_sum(1,1);
        TF(num_cell_file).tf_y_vec_sum = cell_f_sum(1,2);
        TF(num_cell_file).tf_sca_sum = cell_fm_sum;
        TF(num_cell_file).perc_imbalance = imb;
end
TF_mask.a = a;
TF_mask.b = b;
TF_mask.center_x = center_x;
TF_mask.center_y = center_y;
save('TFellipse.mat', 'TF','TF_mask');
clear Fcell.mat Fcell ObjMag TracGridSize binary_mat t tm p i
clear cell_files cell_fm_sum cell_f_sum cell_t_sum cell_tm_sum imb
%clear a b center_x center_y
```

APPENDIX E

FUNCTION FOR CALCULATING INTER-CELLULAR TENSION OR CELL

SHEET TENSION USING ELLIPTICAL MASKS

Fcc_ellipse.m

```matlab
%Yashar Bashirzadeh 2018
% Code to calculate the inter-cellular tension or cell sheet tension
% using elliptical masks

% Edited version of Fcc_circle.m by Dr. Venkat Maruthamuthu for circular
% masks

% - Should have run TF_cricle.m before this:
%        TFellipse.mat should be in current folder)
% Inputs:
%        angle_increment: for angle with horizontal of the line to
%                         divide ellipse into two, ~ 5 to 45 (default value 5)
% Outputs:
%         Fccellipse.mat has:
%         Fcc has angle of dividing line, first_half_tension (x and y components) and
%         second_half_tension (x and y components) listed (in nN)

function Fcc_ellipse(angle_increment)
if nargin < 1
    angle_increment = 5;
end
load Trac.mat
load TFellipse.mat

ObjMag = TracCalc_settings.ObjMag;
TracGridSize = TracCalc_settings.GridSize;

cell_files = dir('./binary/binary*.*');
num_cell_files = numel(cell_files);

% the center of the mask:
center_x = TF_mask.center_x;
center_y = TF_mask.center_y;
%rmdir('half_binary','s');
mkdir('half_binary');

for num_cell_file = 1:1:(num_cell_files)
    disp(['Processing Frame' num2str(num_cell_files) '...'])
for ang = 0:angle_increment:179
    disp(['Processing angle' num2str(ang) '...'])
binary_mat = imread(fullfile('./binary/',cell_files(num_cell_file).name));
sdb = size(binary_mat);
half1_binary_mat(:,:)=binary_mat(:,:);
```

```matlab
half2_binary_mat(:,:)=binary_mat(:,:);
if ang <= 90
    for ix = 1:1:sdb(2)
        for iy = 1:1:sdb(1)
            if iy < (-tan(ang*pi/180)*ix)+center_y+...
                    (tan(ang*pi/180)*center_x) | ix < ...
                    ((center_y-iy)/tan(ang*pi/180))+center_x
                half1_binary_mat(iy,ix)=0;
            end
        end
    end
else
    for ix = 1:1:sdb(2)
        for iy = 1:1:sdb(1)
            if iy > (-tan(ang*pi/180)*ix)+center_y+...
                    (tan(ang*pi/180)*center_x) | ix < ...
                    ((center_y-iy)/tan(ang*pi/180))+center_x
                half1_binary_mat(iy,ix)=0;
            end
        end
    end
end
str1 = strcat('./half_binary/half1_binary_',int2str(ang),'.tif');
imwrite(half1_binary_mat,str1,'compression','none');

if ang <= 90
    for ix = 1:1:sdb(2)
        for iy = 1:1:sdb(1)
            if iy > (-tan(ang*pi/180)*ix)+center_y+...
                    (tan(ang*pi/180)*center_x) | ix > ...
                    ((center_y-iy)/tan(ang*pi/180))+center_x
                half2_binary_mat(iy,ix)=0;
            end
        end
    end
else
    for ix = 1:1:sdb(2)
        for iy = 1:1:sdb(1)
            if iy < (-tan(ang*pi/180)*ix)+center_y+...
                    (tan(ang*pi/180)*center_x) | ix > ...
                    ((center_y-iy)/tan(ang*pi/180))+center_x
                half2_binary_mat(iy,ix)=0;
            end
        end
    end
end
str2 = strcat('./half_binary/half2_binary_',int2str(ang),'.tif');
imwrite(half2_binary_mat,str2,'compression','none');

t1 = TracCalc_results(num_cell_file).trac;
t2 = TracCalc_results(num_cell_file).trac;
p = TracCalc_results(num_cell_file).pos;
for i=1:1:length(p)
```

```matlab
        if half1_binary_mat(uint16(p(i,2)),uint16(p(i,1)))==0
        t1(i,1)=0;
        t1(i,2)=0;
        end
        if half2_binary_mat(uint16(p(i,2)),uint16(p(i,1)))==0
        t2(i,1)=0;
        t2(i,2)=0;
        end
    end
    % vector sum of traction stresses:
    cell_t1_sum=[sum(t1(:,1)) sum(t1(:,2))];
    cell_t2_sum=[sum(t2(:,1)) sum(t2(:,2))];
    % traction to force conversion factor
    conv_fac = 0.001 * (6.45*TracGridSize/ObjMag)^2; % pN->nN; grid area in um2

    cell_f1_sum=conv_fac.*cell_t1_sum;
    cell_f2_sum=conv_fac.*cell_t2_sum;

    Fccc((ang/angle_increment)+1,num_cell_file).f1_sum_x = cell_f1_sum(1,1);
    Fccc((ang/angle_increment)+1,num_cell_file).f1_sum_y = cell_f1_sum(1,2);
    Fccc((ang/angle_increment)+1,num_cell_file).f2_sum_x = cell_f2_sum(1,1);
    Fccc((ang/angle_increment)+1,num_cell_file).f2_sum_y = cell_f2_sum(1,2);
    Fccc_settings.angle_incr = angle_increment;
    end
    for i=1:1:(ang/angle_increment)+1
        for j=1:1:4
            F_mat(i,1)=Fccc(i,num_cell_file).f1_sum_x;
            F_mat(i,2)=Fccc(i,num_cell_file).f1_sum_y;
            F_mat(i,3)=Fccc(i,num_cell_file).f2_sum_x;
            F_mat(i,4)=Fccc(i,num_cell_file).f2_sum_y;
        end
    end
    str3 = strcat('./Fccc_data_',int2str(num_cell_file),'.xlsx');
    xlswrite(str3,F_mat);
    clear cell_f1_sum cell_f2_sum cell_t1_sum cell_t2_sum half1_* half2_*
    clear str1 str2 str3 t1 t2 p ix iy F_mat i j
    end
    save('Fccellipse.mat', 'Fccc','Fccc_settings');
    clear Fccellipse.mat ObjMag TracGridSize binary_mat
    clear cell_files num_cell_files conv_fac
```

APPENDIX F

MEASURING AND PLOTTING STRAIN ENERGY AND SHEET TENSION

```
% Yashar Bashirzadeh 2017

% The code obtains, plots, and saves strain energy (density) and sheet tensions (over
% island length) along x-x and y-y midlines for eliptical masks.
% It calls the functions 'TF_ellipse.m' and 'Fcc_ellipse.m'.
% It uses the traction data obtained using "assembly analysis.m" or "pivlab to lab code.m".

% size.xlsx (a column of time lapse island area)should have been saved in the associated
% cell folder.Of course the length of the column vector should be equal to the number of time
% points (Number of BeadImages-1);

% length_island.xlsx [2 column vectors including the lengths of all islands along y-y
% (first column)and xx (second column)] should have been saved in the folder which contains
% all the cell folders. For example, an experiment which has captured time-lapse images of
% 5 islands at 10 time points sould have a length.xlsx containing a 50 by 2
% matrix (a 10 by 2 column vector for each islnd).

% The eliptical mask of each islnd should have been saved as 0001.tiff in the
% associated cell folder.

% if user drawn masks are used instead of eliptical masks, the 'loops' section of this script
% should be replaced with the commented codes located at the end of this script. The mask for
% each islnd should  have been saved as 0001.tiff in the associated cell folder. In this case
% the halves of the drawn masks (for measuring sheet tension along x-x and y-y midliness)
% should be manually created by the user and saved as 00001.tiff (left half), 00002.tiff
% right half), 00003.tiff (bottom half), and 00004.tiff (top half) in the associated cell folder.


% The folder which contains all cell folders should be located in a folder in the general
% folder 'Lab code'.'lab code' itslef can be  located anywhere in PC.
% an example for correct location of cell foders:
% Z:\Yashar\LabCode\MDCK\analysis
% Here the folder 'MDCK' must be in the general foder 'LabCode' and the
% 'MDCK' folder itself contains the folder 'analysis' which is the folder that includes
% all the cell folders (1,2,...) for a particular experiment or a set of experiments.

% Before running set the current directory to LabCode/analysis

% The user should set the inputs before running:

% User defined inputs ...................................................

C_dir = 'MDCK\analysis\'; %File containing cell folders. Look at the example above.
folder = [1 14];           %First and last folders to be processed.
N_BeadImages =8;           %number of bead images of each cell foder.
```

```matlab
time=5:10:65;                %Time points (for time lapse plots).
time_ticks={'5-10','15-20','25-30','35-40','45-50','55-60','65-70'}; %Time ticks for time plots.

% End of User defined inputs ..........................................



%....................................................................
%....................................................................
%....................................................................
%....................................................................
% Import cell size xlsx files.........................................
prefix_dir =['../',C_dir];
LENGTH=xlsread([prefix_dir,'length_island.xlsx']);
for t = folder(1):folder(2)
size{t}=xlsread([prefix_dir,num2str(t),'/size.xlsx']);
end

addpath('../forces');



% Loops section*********************************************Loops section
%....................................................................
%....................................................................

for t = folder(1):folder(2)
for k =1:N_BeadImages-1
mkdir ([prefix_dir,num2str(t),'/results',num2str(k),'/binary']);

copyfile([prefix_dir,num2str(t),'/0001.tif'],...
[prefix_dir,num2str(t),'/results',num2str(k),'/binary/binary_01.tif']);

cd ([prefix_dir,num2str(t),'/results',num2str(k)]);
F_cell;
TF_ellipse;
Fcc_ellipse (90);
load('Fccellipse.mat')
save('Fccc');
cd '../../../../analysis'
end
end

markers = {'+','o','*','x','v','d','^','s','>','<','+','o','*','x','v'};
for t = folder(1):folder(2)
for k =1:N_BeadImages-1
load([prefix_dir,num2str(t),'/results',num2str(k),'/Fcell.mat'])
load([prefix_dir,num2str(t),'/results',num2str(k),'/Fccc.mat'])

x(t,k)=Fcell.tf_sca_sum;
y(t,k)=Fcell.strain_energy;
```

```matlab
z_imb(t,k)=Fcell.perc_imbalance;

zx1(t,k)=Fccc(2).f1_sum_x;
zx2(t,k)=Fccc(2).f2_sum_x;
zy1(t,k)=Fccc(2).f1_sum_y;
zy2(t,k)=Fccc(2).f2_sum_y;
zx(t,k)=(zx1(t,k)-zx2(t,k))/2;
zy(t,k)=(zy1(t,k)-zy2(t,k))/2;
z(t,k)=sqrt(zx(t,k)^2+zy(t,k)^2);
error(t,k)=sqrt((zx1(t,k)+zx2(t,k))^2+(zy1(t,k)+zy2(t,k))^2)/2;

imb(t,k)=Fcell.perc_imbalance;

load([prefix_dir,num2str(t),'/results',num2str(k),'/Fccc.mat'])

X_zx1(t,k)=Fccc(1).f1_sum_x;
X_zx2(t,k)=Fccc(1).f2_sum_x;
X_zy1(t,k)=Fccc(1).f1_sum_y;
X_zy2(t,k)=Fccc(1).f2_sum_y;
X_zx(t,k)=(X_zx1(t,k)-X_zx2(t,k))/2;
X_zy(t,k)=(X_zy1(t,k)-X_zy2(t,k))/2;
X_z(t,k)=sqrt(X_zx(t,k)^2+X_zy(t,k)^2);
X_error(t,k)=sqrt((X_zx1(t,k)+X_zx2(t,k))^2+(X_zy1(t,k)+X_zy2(t,k))^2)/2;
end


%...............................................................
%...............................................................
% End of Loops section ******************************End of Loops section




figure(1);
plot(time,x(t,:),'markerfacecolor','k','markeredgecolor','k')
xlabel( 'time (min)');
xticks(time)
xticklabels(time_ticks);
ylabel('TF scalar sum (nN)');
box off
set(gca,'fontsize',12,'fontweight','bold')
hold on
S=size{t};

figure(2);
plot(time,S(1:N_BeadImages-1,2)','markerfacecolor','k','markeredgecolor','k')
xlabel( 'time (min)');
xticks(time)
xticklabels(time_ticks);
ylabel('area (\mum^2)');
box off
set(gca,'fontsize',12,'fontweight','bold')
hold on
```

```matlab
SsumArea(t,:)=x(t,:)./S(1:N_BeadImages-1,2)';

figure(3);
plot(time,SsumArea(t,:),'markerfacecolor','k','markeredgecolor','k')
xlabel( 'time (min)');
xticks(time)
xticklabels(time_ticks);
ylabel('TF scalar sum/area (nN/\mum^2)');
%ylim([0.02 0.12])
box off
set(gca,'fontsize',12,'fontweight','bold')
hold on

figure(4);
plot(time,y(t,:),'markerfacecolor','k','markeredgecolor','k')
xlabel( 'time (min)');
xticks(time)
xticklabels(time_ticks);
ylabel('strain energy (fJ)');
box off
set(gca,'fontsize',12,'fontweight','bold')
%ylim([0 7000])
hold on
SenergyArea(t,:)=y(t,:)./S(1:N_BeadImages-1,2)';

figure(5);
xticks(time)
plot(time,y(t,:)./S(1:N_BeadImages-1,2)','markerfacecolor','k','markeredgecolor','k')
xlabel( 'time (min)');
xticklabels(time_ticks);
ylabel('strain energy/area (fJ/\mum^2)');
%ylim([0 0.05])
box off
set(gca,'fontsize',12,'fontweight','bold')
hold on
end

for t=folder(1):folder(2)
load([prefix_dir,num2str(t),'/results',num2str(k),'/TFellipse.mat'])
a(t)=TF_mask.a;
b(t)=TF_mask.b;
end
a=a';
b=b';
n=N_BeadImages-1;
for k =1:n
zz(folder(1):folder(2),k)=z(folder(1):folder(2),k)./LENGTH(n*folder(1)-(n-1):n:n*folder(2)-(n-1),1);
X_zz(folder(1):folder(2),k)=X_z(folder(1):folder(2),k)./LENGTH(n*folder(1)-(n-1):n:n*folder(2)-(n-1),2);
zavg(k)=mean(zz(folder(1):folder(2),k));
X_zavg(k)=mean(X_zz(folder(1):folder(2),k));
%z_area_avg=mean(z(:,k)./S(1:N_BeadImages-1,2)');
```

```matlab
error_avg(k)=mean(error(folder(1):folder(2),k)./LENGTH(n*folder(1)-(n-1):n:n*folder(2)-(n-1),1));
%X_z_area_avg=mean(X_z(:,k)./S(1:N_BeadImages-1,2)');
X_error_avg(k)=mean(X_error(folder(1):folder(2),k)./LENGTH(n*folder(1)-(n-1):n:n*folder(2)-(n-1),2));
%error_avg(k)=(error(1,k)+error(2,k)+error(4,k)+error(5,k))/4;
%error_area_avg=mean(error(:,k)./S(1:N_BeadImages-1,2)');
end

figure(6);
%bar(time,zavg);
hold on
e=errorbar(time,zavg,error_avg)
e.Color = 'k'; e.Marker='.'; e.MarkerSize=20; e.MarkerFaceColor='k';
xlabel( 'time (min)');
xticks(time)
xticklabels(time_ticks);
ylabel('Intra sheet force per unit length  (nN/\mum^2)')
hold on

figure(7);
%bar(time,X_zavg);
hold on
e=errorbar(time,X_zavg,X_error_avg);
e.Color = 'k'; e.Marker='.'; e.MarkerSize=20; e.MarkerFaceColor='k';
xlabel( 'time (min)')
xticks(time)
xticklabels(time_ticks);
ylabel('Intra sheet force per unit length  (nN/\mum^2)')
hold on

figure(8);
AvgSsumArea=mean(SsumArea);
StdSsumArea=std(SsumArea);
e=errorbar(time,AvgSsumArea,StdSsumArea);
e.Color = 'k'; e.Marker='.'; e.MarkerSize=20; e.MarkerFaceColor='k';
xlabel( 'time (min)');
xticks(time)
xticklabels(time_ticks);
ylabel('TF scalar sum/area (nN/\mum^2)');
hold on

figure(9);
AvgSenergyArea=mean(SenergyArea);
StdSenergyArea=std(SenergyArea);
e=errorbar(time,AvgSenergyArea,StdSenergyArea);
e.Color = 'k'; e.Marker='.'; e.MarkerSize=20; e.MarkerFaceColor='k';
xlabel( 'time (min)');
xticks(time)
xticklabels(time_ticks);
ylabel('strain energy/area (fJ/\mum^2)');
hold on

figure(10);
```

```matlab
SEM_SsumArea=std(SsumArea)/sqrt(length(SsumArea));
e=errorbar(time,AvgSsumArea,SEM_SsumArea);
e.Color = 'k'; e.Marker='.'; e.MarkerSize=20; e.MarkerFaceColor='k';
xlabel( 'time (min)');
xticks(time)
xticklabels(time_ticks);
ylabel('TF scalar sum/area (nN/\mum^2)');
hold on

figure(11);
SEM_SenergyArea=std(SenergyArea)/sqrt(length(SenergyArea));
e=errorbar(time,AvgSenergyArea,SEM_SenergyArea)
e.Color = 'k'; e.Marker='.'; e.MarkerSize=20; e.MarkerFaceColor='k';
xlabel( 'time (min)');
xticks(time)
xticklabels(time_ticks);
ylabel('Strain energy/area (fJ/\mum^2)');
hold on

figure(12)
z1mag=sqrt(zx1.^2+zy1.^2);
z2mag=sqrt(zx2.^2+zy2.^2);
timeavg_z1mag=mean(z1mag');
timeavg_z2mag=mean(z2mag');
plot(timeavg_z1mag,timeavg_z2mag,'ok','markerfacecolor','k');
xlabel('F1(nN)');
ylabel('F2(nN)');
box off
hold on
plot(linspace(0,max(timeavg_z1mag(:)),max(timeavg_z1mag(:))/100),linspace(0,max(timeavg_z1mag(:))
,max(timeavg_z1mag(:))/100),'--k')

figure(13)
Xz1mag=sqrt(X_zx1.^2+X_zy1.^2);
Xz2mag=sqrt(X_zx2.^2+X_zy2.^2);
timeavg_Xz1mag=mean(Xz1mag');
timeavg_Xz2mag=mean(Xz2mag');
plot(timeavg_Xz1mag,timeavg_Xz2mag,'ok','markerfacecolor','k');
xlabel('F1(nN)');
ylabel('F2(nN)');
box off
hold on
plot(linspace(0,max(timeavg_Xz1mag(:)),max(timeavg_Xz1mag(:))/100),linspace(0,max(timeavg_Xz1mag(
:)),max(timeavg_Xz1mag(:))/100),'--k')

figure(14)
teta1=atand(zx1./abs(zy1));
teta2=atand(-zx2./abs(zy2));
plot(teta1,teta2,'ok','markerfacecolor','k');
xlabel('\theta1 (degrees)');
ylabel('\theta2 (degrees)');
 ylim([0 90])
 xlim([0 90])
```

```matlab
box off

figure(15)
%Xz1_mag=sqrt(X_zx1.^2+X_zy1.^2)
tetaX1=atand(X_zy1./abs(X_zx1));
tetaX2=atand(-X_zy2./abs(X_zx2));
plot(tetaX1(:),tetaX2(:),'ok','markerfacecolor','k');
xlabel('\theta1 (degrees)');
ylabel('\theta2 (degrees)');
 ylim([0 90])
 xlim([0 90])
box off


figure(16)
z1mag=sqrt(zx1.^2+zy1.^2);
z2mag=sqrt(zx2.^2+zy2.^2);
plot(z1mag(:),z2mag(:),'ok','markerfacecolor','k');
xlabel('F1 (nN)');
ylabel('F2 (nN)');
box off
hold on
plot(linspace(0,max(z1mag(:)),max(z1mag(:))/100),linspace(0,max(z1mag(:)),max(z1mag(:))/100),'--
k')

figure(17)
Xz1mag=sqrt(X_zx1.^2+X_zy1.^2);
Xz2mag=sqrt(X_zx2.^2+X_zy2.^2);
plot(Xz1mag(:),Xz2mag(:),'ok','markerfacecolor','k');
xlabel('F1 (nN)');
ylabel('F2 (nN)');
box off
hold on
plot(linspace(0,max(z1mag(:)),max(z1mag(:))/100),linspace(0,max(z1mag(:)),max(z1mag(:))/100),'--
k')

figure(18)
alpha_init=acosd((zx1(:,1).*zx2(:,1)+zy1(:,1).*zy2(:,1))./(z1mag(:,1).*z2mag(:,1)));
plot(1:1:length(size),alpha_init,'ok','markerfacecolor','k');
xlabel('measurement number');
ylabel('\alpha (degrees)');
box off
hold on
plot(1:1:length(size),180*ones(length(size),1),'--k');
ylim([0 180])

figure(19)
alpha_end=acosd((zx1(:,end).*zx2(:,end)+zy1(:,end).*zy2(:,end))./(z1mag(:,end).*z2mag(:,end)));
plot(1:1:length(size),alpha_end,'ok','markerfacecolor','k');
xlabel('measurement number');
ylabel('\alpha (degrees)');
box off
hold on
```

```matlab
plot(1:1:length(size),180*ones(length(size),1),'--k');
ylim([0 180])

figure(20)
alphaX_init=acosd((X_zx1(:,1).*X_zx2(:,1)+X_zy1(:,1).*X_zy2(:,1))./(Xz1mag(:,1).*Xz2mag(:,1)));
plot(1:1:length(size),alphaX_init,'ok','markerfacecolor','k');
xlabel('measurement number');
ylabel('\alpha (degrees)');
box off
hold on
plot(1:1:length(size),180*ones(length(size),1),'--k');
ylim([0 180])

figure(21)
alphaX_end=acosd((X_zx1(:,end).*X_zx2(:,end)+X_zy1(:,end).*X_zy2(:,end))./(Xz1mag(:,end).*Xz2mag(:,end)));
plot(1:1:length(size),alphaX_end,'ok','markerfacecolor','k');
xlabel('measurement number');
ylabel('\alpha (degrees)');
box off
hold on
plot(1:1:length(size),180*ones(length(size),1),'--k');
ylim([0 180])

figure(22)
TimeAvgImb=mean(imb');
TimeStdImb=std(imb');
errorbar(1:1:length(size),TimeAvgImb,TimeStdImb,'ok','markerfacecolor','k')
xlabel('measurement number')
ylabel('% imbalance')
box off

figure(23)
area=y./SenergyArea;
for i = folder(1):folder(2)
e=plot(area(i,:),y(i,:));
e.Color = 'k'; e.Marker='.'; e.MarkerSize=20; e.MarkerFaceColor='k';
xlabel('Area (\mum^2)');
ylabel('Strain energy(fJ)');
hold on
end

figure(25)
AvgSenergy=mean(y);
StdSenergy=std(y);
SEM_Senergy=std(y)/sqrt(length(y));
e=errorbar(time,AvgSenergy,SEM_Senergy)
e.Color = 'k'; e.Marker='.'; e.MarkerSize=20; e.MarkerFaceColor='k';
xlabel( 'time (min)');
xticks(time)
xticklabels(time_ticks);
ylabel('Strain energy (fJ)');
hold on
```

```
saveas(figure(1),'ScalarSum.fig');
saveas(figure(2),'Area.fig');
saveas(figure(3),'ScalarSum_Area.fig');
saveas(figure(4),'StrainEnergy.fig');
saveas(figure(5),'StrainEnergy_Area.fig');
saveas(figure(6),'inter_celly_length.fig');
saveas(figure(7),'inter_cellx_length.fig');
saveas(figure(8),'AvgSsumArea.fig');
saveas(figure(9),'AvgSenergyArea.fig');
saveas(figure(10),'AvgSsumArea_SEM.fig');
saveas(figure(11),'AvgSenergyArea_SEM.fig');
saveas(figure(12),'TimeAvg F1vsF2_alongY.fig');
saveas(figure(13),'TimeAvg F1vsF2_alongX.fig');
saveas(figure(14),'theta1vstheta2_alongY.fig');
saveas(figure(15),'theta1vstheta2_alongX.fig');
saveas(figure(16),'F1vsF2_alongY.fig');
saveas(figure(17),'F1vsF2_alongX.fig');
saveas(figure(18),'Initial Alpha Vs Measurement number_alongY.fig');
saveas(figure(19),'End Alpha Vs Measurement number_alongY.fig');
saveas(figure(20),'Initial Alpha Vs Measurement number_alongX.fig');
saveas(figure(21),'End Alpha Vs Measurement number_alongX.fig');
saveas(figure(22),'imbalance.fig');
saveas(figure(23),'StrainEnergy vs Area.fig');
saveas(figure(1),'ScalarSum.tif');
saveas(figure(2),'Area.tif');
saveas(figure(3),'ScalarSum_Area.tif');
saveas(figure(4),'StrainEnergy.tif');
saveas(figure(5),'StrainEnergy_Area.tif');
saveas(figure(6),'inter_celly_length.tif');
saveas(figure(7),'inter_cellx_length.tif');
saveas(figure(8),'AvgSsumArea.tif');
saveas(figure(9),'AvgSenergyArea.tif');
saveas(figure(10),'AvgSsumArea_SEM.tif');
saveas(figure(11),'AvgSenergyArea_SEM.tif');
saveas(figure(12),'TimeAvg F1vsF2_alongY.tif');
saveas(figure(13),'TimeAvg F1vsF2_alongX.tif');
saveas(figure(14),'theta1vstheta2_alongY.tif');
saveas(figure(15),'theta1vstheta2_alongX.tif');
saveas(figure(16),'F1vsF2_alongY.tif');
saveas(figure(17),'F1vsF2_alongX.tif');
saveas(figure(18),'Initial Alpha Vs Measurement number_alongY.tif');
saveas(figure(19),'End Alpha Vs Measurement number_alongY.tif');
saveas(figure(20),'Initial Alpha Vs Measurement number_alongX.tif');
saveas(figure(21),'End Alpha Vs Measurement number_alongX.tif');
saveas(figure(22),'imbalance.tif');
saveas(figure(23),'StrainEnergy vs Area.tif');
```

```
% ..............................................................
% ..............................................................
% ..............................................................
% if drawn masks are used, the 'Loops' section of the script above should be replaced with the
code below.


% for t = folder(1):folder(2)
% for k =1:N_BeadImages-1
% mkdir ([prefix_dir,num2str(t),'/results',num2str(k),'/binary']);
% mkdir ([prefix_dir,num2str(t),'/results',num2str(k),'/dilated_binary']);
% copyfile([prefix_dir,num2str(t),'/0001.tif'],...
% [prefix_dir,num2str(t),'/results',num2str(k),'/binary/binary_01.tif']);
% copyfile([prefix_dir,num2str(t),'/00001.tif'],...
% [prefix_dir,num2str(t),'/results',num2str(k),'/dilated_binary/binary1_01.tif']);
% copyfile([prefix_dir,num2str(t),'/00002.tif'],...
% [prefix_dir,num2str(t),'/results',num2str(k),'/dilated_binary/binary2_01.tif']);
%
% cd ([prefix_dir,num2str(t),'/results',num2str(k)]);
% F_cell;
% Fcc_cellpair;
% load('Fcccp.mat')
% Fccp_along_y=Fcccp;
% save('Fccp_along_y');
% cd '../../../../analysis'
% copyfile([prefix_dir,num2str(t),'/00003.tif'],...
% [prefix_dir,num2str(t),'/results',num2str(k),'/dilated_binary/binary1_01.tif']);
% copyfile([prefix_dir,num2str(t),'/00004.tif'],...
% [prefix_dir,num2str(t),'/results',num2str(k),'/dilated_binary/binary2_01.tif']);
%
% cd ([prefix_dir,num2str(t),'/results',num2str(k)]);
% Fcc_cellpair;
% load('Fcccp.mat')
% Fccp_along_x=Fcccp;
% save('Fccp_along_x');
% %F_cell_cell(10,8)
% cd '../../../../analysis'
% end
% end
%
% % Plots.............................................................
% markers = {'+','o','*','x','v','d','^','s','>','<','+','o','*','x','v'};
% for t = folder(1):folder(2)
% for k =1:N_BeadImages-1
% load([prefix_dir,num2str(t),'/results',num2str(k),'/Fcell.mat'])
% load([prefix_dir,num2str(t),'/results',num2str(k),'/Fccp_along_y.mat'])
%
% x(t,k)=Fcell.tf_sca_sum;
% y(t,k)=Fcell.strain_energy;
%
% z1(t,k)=Fccp_along_y.cell1_fm_sum;
% z2(t,k)=Fccp_along_y.cell2_fm_sum;
```

```matlab
% zx1(t,k)=Fccp_along_y.cell1_f_sum_x;
% zx2(t,k)=Fccp_along_y.cell2_f_sum_x;
% zy1(t,k)=Fccp_along_y.cell1_f_sum_y;
% zy2(t,k)=Fccp_along_y.cell2_f_sum_y;
% z_imb(t,k)=Fccp_along_y.imb_perc;
% zx(t,k)=(zx1(t,k)-zx2(t,k))/2;
% zy(t,k)=(zy1(t,k)-zy2(t,k))/2;
% z(t,k)=sqrt(zx(t,k)^2+zy(t,k)^2);
% error(t,k)=sqrt((zx1(t,k)+zx2(t,k))^2+(zy1(t,k)+zy2(t,k))^2)/2;
%
% imb(t,k)=Fcell.perc_imbalance;
%
% load([prefix_dir,num2str(t),'/results',num2str(k),'/Fccp_along_x.mat'])
%
% X_z1(t,k)=Fccp_along_x.cell1_fm_sum;
% X_z2(t,k)=Fccp_along_x.cell2_fm_sum;
% X_zx1(t,k)=Fccp_along_x.cell1_f_sum_x;
% X_zx2(t,k)=Fccp_along_x.cell2_f_sum_x;
% X_zy1(t,k)=Fccp_along_x.cell1_f_sum_y;
% X_zy2(t,k)=Fccp_along_x.cell2_f_sum_y;
% X_z_imb(t,k)=Fccp_along_x.imb_perc;
% X_zx(t,k)=(X_zx1(t,k)-X_zx2(t,k))/2;
% X_zy(t,k)=(X_zy1(t,k)-X_zy2(t,k))/2;
% X_z(t,k)=sqrt(X_zx(t,k)^2+X_zy(t,k)^2);
% X_error(t,k)=sqrt((X_zx1(t,k)+X_zx2(t,k))^2+(X_zy1(t,k)+X_zy2(t,k))^2)/2;
% end
%*************************************************************************
```

VITA

Yashar Bashirzadeh

Department of Mechanical Engineering, Old Dominion University, Norfolk, VA 23529
Office: 2120 Engineering Systems Building, ybash001@odu.edu, (757) 663-3031

Educational Background

- PhD in Mechanical Engineering, Old Dominion University, Norfolk, VA. (2014-2018)
- M. Sc. in Mechanical Engineering, Azad University, Science and Research Branch, Tehran, Iran. (2010-2012)
- B. Sc. in Mechanical Engineering, University of Zanjan, Zanjan, Iran. (2004-2009)

Academic Experience

Research
- Bioengineering: Mechanobiology, Electrotaxis   2015-Present
- Heat & Fluids: Microfluidics, Particle image velocimetry, Convective heat transfer   2012-Present

Teaching
- Thermo-fluids lab instructor, Old Dominion University, up to 3 courses per semester   2015-Present
- Graduate teaching assistant in computational methods for engineers, thermodynamics I and thermodynamics II, Old Dominion University.   2015-present
- Math and physics tutor at Khajeh Nasir institute, Theran, Iran.   2013-2014

Journal Articles

- **Bashirzadeh, Y**., Dumbali, S., Qian, S., Maruthamuthu, V. (2018). Mechanical response of an epithelial island subject to uniaxial stretch on a hybrid silicone substrate. Cellular and Molecular Bioengineering. **(Submitted)**

- **Bashirzadeh, Y**., Chatterji, S., Palmer, D., Dumbali, S., Qian, S., Maruthamuthu, V. (2018). Stiffness Measurement of Soft Silicone Substrates for Mechanobiology Studies Using a Widefield Fluorescence Microscope. Journal of visualized experiments: JoVE. **(Published)**

- **Bashirzadeh, Y**., Qian, S., Maruthamuthu, V. (2018). Effect of Actin Organization and Contractility on Collective Cell Electrotaxis. Bioelectromagnetics. **(Published)**

- **Bashirzadeh, Y**., Qian, S., Maruthamuthu, V. (2017). Non-intrusive Measurement of Wall Shear Stress in Flow Channels. Sensors and actuators A. **(Published)**
  Note: This paper uses Fourier Transform Traction Cytometry (FTTC) to extract wall shear stress.

- **Bashirzadeh, Y**., Maruthamuthu, V., & Qian, S. (2016). Electrokinetic Phenomena in Pencil Lead-Based Microfluidics. Micromachines, 7(12), 235. **(Published)**

- **Bashirzadeh, Y**., & Ashrafi, N. (2014). Heat transfer of Nano-fluids as working fluids of swimming pool heat exchangers. Int. J. Advanced Design and Manufacturing Technology, 7(1), 75-81. **(Published)**

- Zhou, C., **Bashirzadeh, Y**., Bernadowski, T. A., & Zhang, X. (2016). UV Light–Induced Aggregation of

Titania Submicron Particles. Micromachines, 7(11), 203. **(Published)**

- Akurati S., **Bashirzadeh, Y.**, Qian, S., Ghosh D. (2018). Dielectrophoretic effects on freeze casting of Cermaics. **(Manuscript in preparation)**

Proceedings

- Hughes, C., Dutta, D., Bashirzadeh, Y., Ahmed, K. A., & Qian, S. (2015). Measuring shear stress with A Micro Fluidic sensor to improve aerodynamic efficiency. In 53rd AIAA Aerospace Sciences Meeting, AIAA (Vol. 1919). (Published)
- Ashrafi, N., & Bashirzadeh, Y. (2012, November). Enhancement of Heat Transfer by Nanoparticles Added to the Working Fluid of Swimming Pool Heat Exchangers. In ASME 2012 International Mechanical Engineering Congress and Exposition (pp. 2393-2397). American Society of Mechanical Engineers. (Published)
- Hughes, C., Dutta, D., Bashirzadeh, Y., Ahmed, K., & Qian, S. (2014, November). A Multi-Phase Based Fluid-Structure-Microfluidic interaction sensor for Aerodynamic Shear Stress. In APS Meeting Abstracts. (Abstract)
- N. Ashrafi and Y. Bashirzadeh, Nano particled working fluid for heat exchangers, IMECE 2012. (Poster)

Peer Reviewer for

- Scientific Reports – Nature   2018-Present
- ASME journals: Journal of Fluids Engineering   2018-Present

Grant Writing

- Author of the white paper entitled 'Continuous size-separation, trap and detection of bio-aerosols" for grant proposal to Defense University Research Instrumentation Program (DURIP). Principle investigators: Shizhi Qian and Venkat Maruthamuthu   2018

Honors and Awards

- The 2017-2018 Tiwari Endowed Graduate Scholarship in Mechanical Engineering for one graduate student interested in scholarly activities and research (Old Dominion University).
- 1st rank between about 15000 participants in Iranian private universities' nationwide entrance examination for graduate studies of mechanical engineering held in 2010 awarded with graduate scholarship for Master's program.

Engineering Software

- MATLAB (Professional user)
- ImageJ
- COMSOL Multiphysics (Basics)
- Autocad (Basics)
- Autodesk Inventor (Basics)